Title
High-Conductance Electrokinetic Device Characterization and Design

Permalink
https://escholarship.org/uc/item/8sv429q4

Author
Heineck, Daniel Philip

Publication Date
2017

Peer reviewed|Thesis/dissertation

UNIVERSITY OF CALIFORNIA, SAN DIEGO

High-Conductance Electrokinetic Device Characterization and Design

A dissertation submitted in partial satisfaction of the
requirements for the degree
Doctor of Philosophy

in

Electrical Engineering (Photonics)

by

Daniel Philip Heineck

Committee in charge:

- Professor Michael J. Heller, Chair
- Professor Sadik C. Esener, Co-Chair
- Professor Pau Cho
- Professor Zhaowei Liu
- Professor Yuwha Lo
- Professor Andrea Tao

2017

The dissertation of Daniel Philip Heineck is approved, and it is acceptable in quality and form for publication on microfilm and electronically:

Co-Chair

Chair

University of California, San Diego

2017

DEDICATION

To all my friends, family, and compatriots that have pushed and supported me along this journey.

EPIGRAPH

Concern for man and his fate must always form the chief interest of all technical endeavors. Never forget this in the midst of your diagrams and equations.

— *Albert Einstein*

TABLE OF CONTENTS

LIST OF FIGURES

ACKNOWLEDGEMENTS

Chapter 3, in full, is being prepared for publication submission. Heineck, Daniel P.; Kim, Sejung; Heller, Michael J. The dissertation author is the primary investigator and author of the material herein.

Chapter 4, in part, has been submitted for publication of the material as it may appear in ELECTROPHORESIS, 2017, Heineck, Daniel P.; Lewis, Jean M.; Heller, Michael J., Wiley-Blackwell. The dissertation author was the primary investigator and author of this paper.

Chapter 5, in part, is being prepared for publication submission. Heineck, Daniel P.; Heller, Michael J. The dissertation author is the primary investigator and author of the material herein.

VITA

2006	B. S. in Electrical Engineering *summa cum laude*, Oregon State University
2006	B. S. in Computer Engineering *summa cum laude*, Oregon State University
2009	M. S. in Electrical Engineering, Oregon State University
2017	Ph. D. in Electrical Engineering (Photonics), University of California, San Diego

PUBLICATIONS

D. Heineck, B. McFarlane and J. Wager, ”Zinc Tin Oxide Thin-Film-Transistor Enhancement/Depletion Inverter”, *IEEE Electron Device Lett.*, vol. 30, no. 5, pp. 514-516, 2009.

B. McFarlane, P. Kurahashi, D. Heineck, R. Presley, E. Sundholm and J. Wager, ”AC/DC Rectification With Indium Gallium Oxide Thin-Film Transistors”, *IEEE Electron Device Lett.*, vol. 31, no. 4, pp. 314-316, 2010.

I. Yoon, K. Kim, S. Baker, D. Heineck, S. Esener and D. Sirbuly, ”Stimulus-Responsive Light Coupling and Modulation with Nanofiber Waveguide Junctions”, *Nano Letters*, vol. 12, no. 4, pp. 1905-1911, 2012.

I. Yoon, S. Baker, K. Kim, N. Fischer, D. Heineck, Y. Wang, S. Esener and D. Sirbuly, ”Nanofiber Near-Field LightMatter Interactions for Enhanced Detection of Molecular Level Displacements and Dynamics”, *Nano Letters*, p. 130328095017000, 2013.

J. Lewis, D. Heineck and M. Heller, ”Detecting cancer biomarkers in blood: challenges for new molecular diagnostic and point-of-care tests using cell-free nucleic acids”, *Expert Review of Molecular Diagnostics*, vol. 15, no. 9, pp. 1187-1200, 2015.

Lawrence Livermore National Security, LLC, ”Three-dimensional boron particle loaded thermal neutron detector”, 8829460, 2014.

Lawrence Livermore National Security, LLC, ”Method for manufacturing solid-state thermal neutron detectors with simultaneous high thermal neutron detection efficiency ($> 50\%$) and neutron to gamma discrimination ($> 1.0E4$)”, US8558188, 2013.

ABSTRACT OF THE DISSERTATION

High-Conductance Electrokinetic Device Characterization and Design

by

Daniel Philip Heineck

Doctor of Philosophy in Electrical Engineering (Photonics)

University of California, San Diego, 2017

Professor Michael J. Heller, Chair
Professor Sadik C. Esener, Co-Chair

The primary direction of this thesis is to expand and more clearly define the constraints and operating conditions surrounding high-conductance electrokinetic phenomena. Dielectrophoresis (DEP), the movement of polarizable particles in an electric field gradient, is an effective mechanism to separate biological particles, in the range of nanoparticles through cell clusters, from biological solutions, e.g. whole blood, plasma, serum, cerebrospinal fluid, urine, etc. Most research in this realm has been focused in low-conductance solutions, either from dilution or through substantial sample preparation. One major constraint defined is electrochemical corrosion of platinum electrodes in chlorine-bearing solutions. While chlorine concentration is important, corrosion is exacerbated with low frequency electrical stimulus and high current densities. The latter manifests itself as a high faradaic reaction rate and results in local heating. A temperature dependence and frequency sensitivity indicate that platinum-chlorine complexes involved in passivation and de-passivation are kinetically rate-limited. Many confounding electrokinetic forces contribute to particle movement in high-conductance solutions. Joule heating and the resulting density-based fluid flow, i.e. electrothermal flow, is shown to be a major drag force able to overcome DEP forces. Certain device geometries are more sensitive to electrothermal flow; when high electric field gradients are allowed to exist in regions of locally low fluid flow, DEP forces easily dominate electrothermal. Likewise, effective DEP separation is more dependent on micron- or nanometer-sized geometric features to create large electric field gradients than on overall potential differences between electrodes. With corrosion concerns, the V^2 relation for Joule heating, and marginal DEP force benefit from increased voltage, devices for high-conductance electrokinetics need to be optimized for low voltage and low current. This refined understanding may be applied to future device designs as to realize novel or improved device structures.

Chapter 1

Introduction

The increasing interest in molecular diagnostics for research or clinical applications, i.e. forms of personalized or precision medicine, is concomitant the rapid improvements in sequencing technologies and amplification techniques. This progress puts greater burden on sample preparation: throughput, yield, and maintaining sample integrity are all key, and yet present best practices are fundamentally little changed in a several decades. Dielectrophoretic separations offer tremendous benefits over more traditional techniques, and hold promise to positively affect these three critical metrics. One of the greatest advantages is the ability to directly isolate biomarkers such as cell-free DNA, cell-free RNA, and exosomes from whole blood or other biological fluids such as plasma, serum, urine, or cerebrospinal fluid.

Dielectrophoresis, the movement of a polarizable particle in an electric field gradient, has been applied to a number of different biological particles, with sizes ranging from nanoparticles to cells, but the majority of research efforts have focused in cell separations in low-conductance buffers. Few efforts into dielectrophoretic device applications for high-conductance solutions have been realized, greatly limiting potential biological applications for this technique. The work herein looks into futher elucidating the challenges and limitations, both from an electrochemical and electrokinetic perspective, of dielectrophoretic devices for high-conductance solutions.

This thesis is organized as follows. Chapter 2 provides core background and derivations for electrokinetic phenomena. Chapter 3 looks at electrochemical corrosion of platinum electrodes in high-conductance buffers containing chlorine. Chapter 4 examines three different overarching device structures with regards to dominant electrokinetic phenomena, experimentally and in simulations. Chapter 5 provides conclusions and offers future research directions.

Chapter 2

Background

2.1 Dielectrophoresis

Dielectrophoresis (DEP) is movement of a polarizable particle as result of an asymmetric electrostatic force on the particle in a suspending medium where an electric field gradient is present [1]. To understand this phenomenon, it is best to derive the physics of dielectrophoresis from the base principles. Let us start with a homogeneous, lossless spherical particle suspended in a medium with an electric field gradient along the vertical axis, as seen in Fig. 2.1. Likewise, let us assume normal boundary conditions: the potential across the surface is continuous, flux is conserved at the interface, and Laplace's equation is satisfied throughout ($\nabla^2\phi = 0$) [2]. Thus,

$$\begin{aligned}
&\text{at } r = R_{particle} : \\
&\phi_i = \phi_o \text{ and} \\
&\epsilon_p \frac{\partial \phi_i}{\partial r} = \epsilon_m \frac{\partial \phi_o}{\partial r}.
\end{aligned}$$

By applying a field, $E = E_x$, across the particle, it will polarize homogeneously, resulting in a dipole aligned with the external field along the X-axis, e.g. $p = k \cdot E$. Lastly the potential at large distances from the particle must be $\phi = -Ex$. The internal and outside fields are, respectively:

$$\begin{aligned}
&\phi_i = -E_i \cdot x, \text{ where } x = rcos(\theta),\\
&\phi_o = -E \cdot x - \phi_{dipole}, \text{ where, } \phi_{dipole} = \frac{p\hat{r}}{4\pi\epsilon_m r^2},\\
&\phi_o = -E \cdot x + \frac{k \cdot E}{4\pi\epsilon_m r^2} \cdot \frac{x}{r}, \text{ or alternatively,}\\
&\phi_o = -E \cdot cos(\theta)\left(r - \frac{k}{4\pi\epsilon_m r^2}\right)
\end{aligned}$$

To satisfy boundary conditions, we know that for $\phi_i = \phi_o$,

$$E_i = E\left(1 - \frac{k}{4\pi\epsilon_m R^3}\right),$$

and for $\epsilon_p \frac{\partial\phi_i}{\partial r} = \epsilon_m \frac{\partial\phi_o}{\partial r}$

$$\epsilon_p E_i = \epsilon_m E\left(1 + \frac{2k}{4\pi\epsilon_m R^3}\right).$$

Solving for k yields

$$k = 4\pi\epsilon_m R^3\left(\frac{\epsilon_p - \epsilon_m}{\epsilon_p + 2\epsilon_m}\right).$$

The difference in polarizability between the particle and medium, the particle's relative polarizability, is defined by the Clausius-Mossotti relation in Eqn. 2.1, which has a range from $(-0.5, 1)$.

$$CM = \frac{\epsilon_p - \epsilon_m}{\epsilon_p + 2\epsilon_m} \tag{2.1}$$

In a uniform field, a dipole will experience forces that algebraically sum to

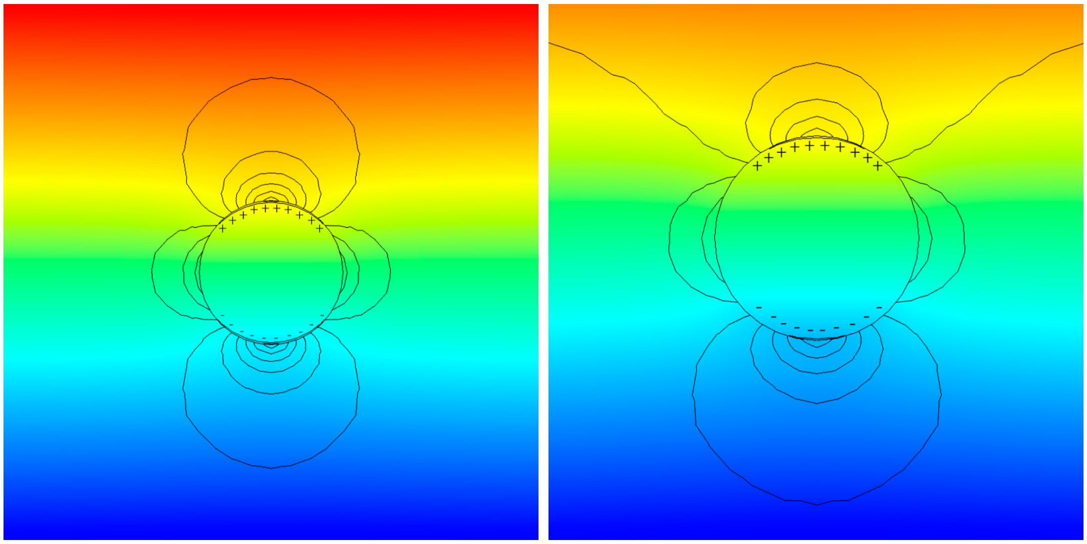

Figure 2.1: Dielectrophoresis is the result of asymmetric fields on a polarizable particle. On the left, the electric field is symmetric, and therefore the coulombic forces are balanced. The particle experiences zero net force as the polarized charges are equal and opposite in direction. In an asymmetric field in on the right, the polarized charges experience different respective fields and, therefore, there is a net force in one direction. The color gradient follows potential, whereas the lines make up the contour plot of the normalized electric field.

zero, but in a nonuniform field, there will be a difference in force acting on the positive and negative charges. The force on a dipole in an nonuniform field can be written:

$$F(x) = q[E(x + d) - E(x)] \tag{2.2}$$

Taking the Taylor series expansion of Eqn. 2.2 about $F(x + d)$, where $d = 2R$ is the effective charge separation in the particle,

$$F_{DEP} = q\left[E(x) + \frac{2R}{1!} \cdot \frac{\partial E}{\partial x} + \ldots + \frac{(2R)^n}{n!} \cdot \frac{\partial E}{\partial x}\right] - qE(x).$$

It is commonly assumed that the particle's diameter is smaller than the field gradient, and thus only the first term of the expansion is needed. Thus,

$$F_{DEP} = q2R\frac{\partial E}{\partial x} = p\frac{\partial E}{\partial x} = kE \cdot \nabla,$$

which is written in its commonly-read form:

$$F_{DEP} = 2\pi\epsilon_m R^3 \left(\frac{\epsilon_p - \epsilon_m}{\epsilon_p + 2\epsilon_m}\right)(\nabla E^2). \tag{2.3}$$

There are a number of important aspects of this equation that one should note. First is the R^3 term, which indicates that this is effectively a volume force, and, specifically, small particles will ultimately not be affected by DEP to the same magnitude as larger particles. Using a spherical model of a particle, the drag is:

$$D = \frac{1}{2}\rho C_d A V^2,$$

where A is the projected area of the sphere along the drag axis. Area follows $A = \pi R^2$, so one sees, to a first order, that particles sensitivity to a DEP field falls off $1/R$. Second, the Claussius-Mossoti factor tells us that DEP force is frequency dependent: at certain frequencies the respective dispersion relations of the medium and the particle will result in identical polarization. This null is called the cross-over frequency, where DEP goes from positive (where the particle moves towards a higher field gradient) and negative (where the particle moves away from a higher field gradient), or vice-versa. Particles with dielectric properties closely matching their supporting medium will also experience a very small DEP force. Thirdly, the ∇E^2 term underscores the importance of engineering the electric field geometrically in order to controllably move particles into desired locations. In many cases, one does not have control over the particle's dielectric properties, nor the medium, so one must use a combination of electric field control and frequency selection to maximize the desired DEP force.

2.1.1 Multipolar effects

For large particles in highly gradient fields, the dipole approximation described in Eqn. 2.3 breaks down and further refinements to the model are needed, namely representing the uncharged particle as a multipole. Essentially, the potential on the outside of an uncharged sphere may be described by a sequence of multipoles located at the center of the sphere, e.g. the external potential of a general multipole follows the form,

$$\begin{aligned} \phi_o &= -E \cdot x - \sum \phi_n \\ \phi_n &= \frac{1}{4\pi\epsilon_m} p_n \frac{Y_n}{r^{n+1}}, \quad p_n = n! q d^n. \end{aligned}$$

Y_n is determined by a Legendre polynomials of the multipole expansion [1]. A linear multipole of order n may be described by:

$$F_{DEP_n} = qd^n \cdot \frac{\partial^n E}{\partial x^n}.$$

In general, one needs to account for multipole moments when field gradients are large or when, due to electrode design, the ∇E^2 term goes to zero [3]. It should be noted that these conditions are only found when the particle is in close proximity to the electrodes and the radius of the particle is proportional to the electrode spacing. Cell-sized particles may be affected the multipolar effects, but in submicron particles, such as cellular fragments, a dipole model is more than sufficient.

2.1.2 Deviations away from ideal model

While our model assumed a lossless dielectric sphere, many biological particles are conductive due to either captured (e.g. a cell) or associated (e.g. cell-free DNA) mobile ions, and thus their permittivity or conductivity must be represented by complex terms:

$$\begin{aligned}\epsilon_p^* &= \epsilon_0\epsilon_p - \frac{j\sigma_p}{\omega}\\ \sigma_p^* &= \sigma_p + j\omega\epsilon_0\epsilon_p.\end{aligned}$$

Of important note is the frequency-dependent nature of these terms, namely at low frequencies, the conductivity is dominated by the movement of mobile charges, whereas at high frequencies, the permittivity depends on the polarization of bound charges. Current and will be in phase with voltage at low frequencies, but lead voltage up to $\pi/2$ radians as frequency increases towards infinity. Likewise, the Clausius-Mossotti factor can be written in terms of the complex terms, either as a permittivity or as a conductivity:

$$CM^* = \left(\frac{\epsilon_p^* - \epsilon_m^*}{\epsilon_p^* - 2\epsilon_m^*}\right) \quad \text{or} \quad CM^* = \left(\frac{\sigma_p^* - \sigma_m^*}{\sigma_p^* + \sigma_m^*}\right). \tag{2.4}$$

Unlike the homogeneous particle model described in Eqn. 2.3, most biological particles of relevance are neither spherical nor homogeneous. A cell, for example, can be better described by a model where the heterogeneity is ensembled into a single complex permittivity. Such permittivity models rely on particle effective radius, membrane thickness, membrane permittivity, and, finally, cytoplasm effective permittivity. Similarly, many particles carry a fixed charge that shows electrophoretic mobility at very low frequency stimulus, but this effect averages out as frequency increases. Double layer effects associated with the charged particle, however, may contribute dramatically to the effective particle diameter and dielectric properties.

2.2 Dielectric modeling of biological products

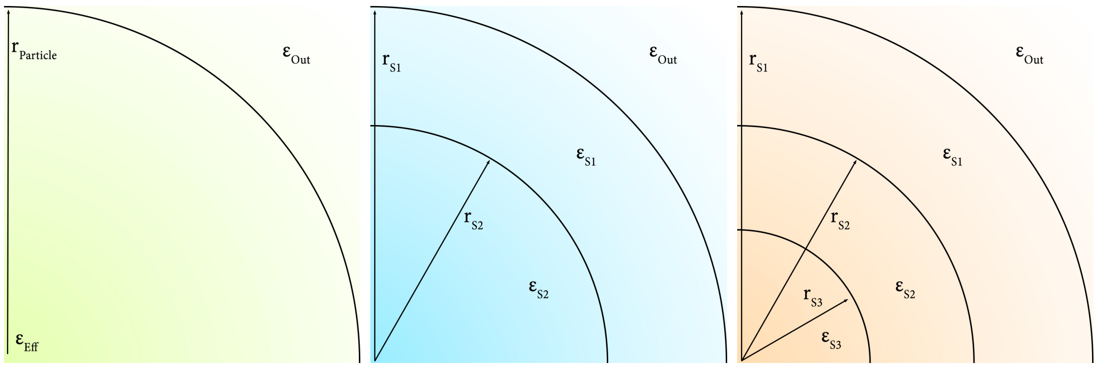

(a) Lumped Model (b) Single shell (c) Multi-shell

Figure 2.2: Equivalent dielectric model (a) for Eqn. 2.2, where an outer shell and inner shell of respective dielectric constants and radii (labeled in b) can be lumped into a single, complex term. Likewise, this model may be recursively applied on multi-shell models (c), an $\epsilon_{Eff_{S}2}$ derived from R$_{S2}$, R$_{S3}$, ϵ_{S2}, and ϵ_{S3}. Then, having simplified (c) into an equivalent (b), Eqn. 2.2 will simplify to a nested ϵ_{Eff}.

Given the complexity of larger biological particles, e.g. cells, viruses, and nuclei, a core-shell model of the ensemble characteristics of the particles internal structure is typically used [3]–[6]. The base case is a model where the cell's constituents are lumped into a homogeneous term, as seen in Fig. 2.2a: a non-conductive lipid shell surrounding a conductive cytosol core. As more complex models are needed to fit frequency dependent terms, additional layers may be incorporated [4]. In either case, these shell structures can be incorporated into already established equations for dielectric effects on particles. To start with a single-shell model shown in Fig. 2.2b, we have a system with two relaxation frequency, respective to each component which yields the effective permittivity [3]

$$\epsilon_{eff} = \epsilon_{s1} \left(\left[\left(\frac{R_{s1}}{R_{s2}} \right)^3 + 2\frac{\epsilon_{s2} - \epsilon_{s1}}{\epsilon_{s2} + 2\epsilon_{s1}} \right] \Big/ \left[\left(\frac{R_{s1}}{R_{s2}} \right)^3 - \frac{\epsilon_{s2} - \epsilon_{s1}}{\epsilon_{s2} + 2\epsilon_{s1}} \right] \right). \tag{2.5}$$

If one needs more than one shell, such as Fig. 2.2c, then Eqn. 2.2 may be applied from the innermost shell outwards in an iterative fashion. This isotropic model of the effective dielectric model works under most circumstances, but falls apart under specific conditions, such as incorporating charged, lipid-soluble molecules into the cell membrane, whereupon a strong anisotropy occurs between tangential and radial field components. Under such circumstances, more detailed profiling of the cell's electrodynamics is needed [5].

2.3 Double Layer Effects

In the presence of a charged surface, charges within an electrolyte will distribute near the interface in a complex profile. Originally identified by Helmholtz, a number of models have been developed to describe the distribution of ions that have generally converged on a concept of essentially fixed surface charges near the surface (Stern layer) with increasingly diffuse and mobile charges further away from the interface (diffuse/Guoy layer) [7]. The Stern layer is then separated into an inner Helmholtz layer (IHL) and an outer Helmholtz layer (OHL), Three planes are used to respectively bound these two regions: the physical surface, the inner Helmholtz plane (IHP) and outer Helmholtz plane (OHP). The IHL is typically used to describe adsorbed and Coulombically bound ions whereas the OHL is used to describe electrostatically interacting ions. The OHP signifies where ions further from the surface are mobile and purely driven by electrostatic forces. While models

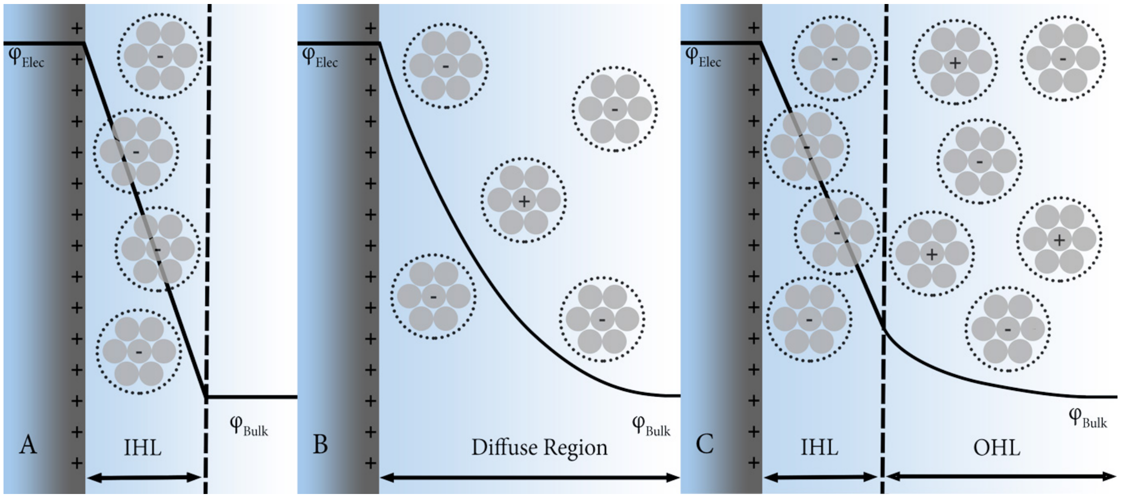

Figure 2.3: Diagrams showing the potential profile of the Helmholtz (A), Gouy-Chapman (B), and Stern-Gouy-Chapman (C) models of the double layer effect at an conductor-electrolyte interface. The Helmholtz model assumes a tightly bound layer of counter-ions (shown as clusters of ions surrounded by water molecules) that resides between the conductor surface and the inner Helmholtz layer (IHL). Guoy and Chapman developed a model based on electrostatics and diffusion, where there is an exponential decay away from the interface. Further profiling the interface led to a model, and derivatives thereof, that combine the two models: namely, a highly dense, tightly bound layer of counter ions immediately local to the interface and an exponential grading of concentration and potential to the bulk.

define these layers as distinct, the transition is between them, in reality, more blurred and progressive. As charge must be conserved, the surface charge densities must sum to zero:

$$\sigma^{surf} + \sigma^{IHL} + \sigma^{OHL} = 0.$$

Surrounding a particle or near a surface, a thin film of fluid is essentially bound, beyond which hydrodynamic slip is permitted. Thus, for drag purposes, a particle's effective size must take this extra width into account. Like the Helmholtz layers, this distinction between bound and slip mathematically defined as a specific distance from the particle, but the transition is progressive over distance. The shear plane is located near, but slightly outside that of the OHP. Zeta potential, defined at the shear plane where charges are unbound, is most commonly used parameter to describe the electrokinetic phenomena of particles. Zeta potential is dependent on the solution's conductivity and fluid properties, which will modulate the size of the Helmholtz layers and shear plane. Important terms, such as the isoelectric point across varying solution chemistries, and whether particles will tend to flocculate or remain dispersed are tied to the zeta potential of the particle-solution system. The double layer has a dramatic effect on the effective dielectric properties of small particles and, as such, most biological particulate of interest must be treated in respect to its supporting medium.

To understand the diffuse region, Boltzmann statistics are needed; the concentration of ion i follows the form:

$$c_i = c_{i,\infty} e^{\frac{-z_i F \Phi}{RT}},$$

where $c_{i,\infty}$ is the concentration the bulk, z_i is the ion's charge number, F is Faraday's constant, R is the universal gas constant, and T is temperature. Therefore, we may write the local charge density ρ_E as the sum of different ion concentrations,

$$\rho_E = \sum_i c_{i,\infty} z_i F e^{\frac{-z_i F \Phi}{RT}}$$

To determine the ion distribution due to potential, we must combine the charge density equation above with the Poisson equation,

$$\nabla^2 \phi = -\frac{\rho_E}{\epsilon}.$$

Assuming that ions are point charges and a mean field approximation, we have the general form of the Poisson-Boltzmann equation:

$$\nabla^2 \Phi = -\frac{F}{\epsilon} \sum_i c_{i,\infty} z_i e^{\frac{-z_i F \Phi}{RT}}. \tag{2.6}$$

To simplify this equation into a more understandable form, we may assume the interface's wall radius is much larger than the Debye length, $\lambda_D = \sqrt{\frac{\epsilon RT}{2F^2 C_0}}$, and thus Eqn. 2.6 simplifies to a nondimensionalized 1D approximation:

$$\frac{\partial^2 \Phi^*}{\partial y^{*2}} = -\frac{1}{2} \sum_i c^*_{i,\infty} z_i e^{-z\Phi^*}$$

where $\Phi^* = \frac{F\Phi}{RT}$. Simplifying further by stating $c_1 = c_2 = c_\infty$ and $|z_1| = |z_2|$, i.e. a single symmetric electrolyte, and taking the first-order Taylor series expansion, we have the Debye-Hückel approximation:

$$\frac{\partial^2 \Phi^*}{\partial y^{*2}} = \Phi^*.$$

Eqn. 2.6 has no analytical solution, but there are some important take away concepts to examine. The diffuse region is very thin, on the order of the Debye length, and tends to fall off exponentially from the edge of the Stern layer before the concentration approaches that of the bulk solution. As result, extremely high electric field gradients may exist in this layer. Higher electrolyte concentrations yield thinner Stern layers and diffuse layers [8], and thus, higher local electric field gradients. Potentials of a discrete, isolated particle must be described relative to the bulk solution, as the surface potential Φ^0, can not be determined unambiguously. Thus, surface charge is the driving parameter, and potentials exist solely within the context of a model.

Unlike free floating particulate, electrode walls can be deliberately biased to a specific potential, and, therefore, can affect the double layer's thickness and the dynamics of mass transfer and local reaction kinetics [9].

2.4 Electro-osmotic Flow

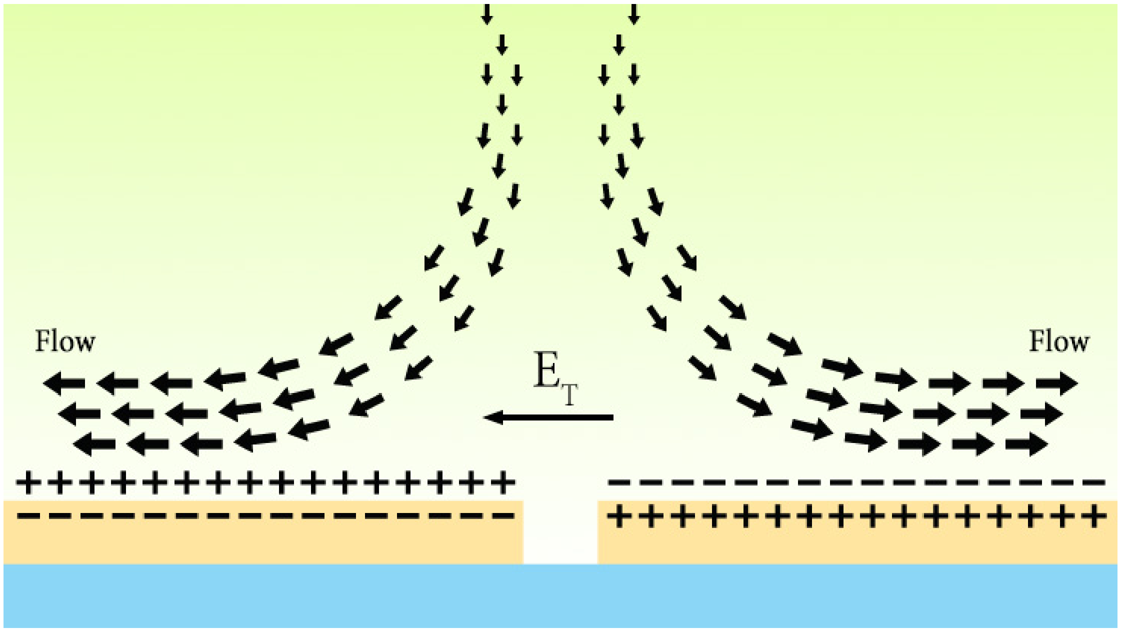

Figure 2.4: The double layer established above the electrode surface interacts with any tangential electric field to result in a net displacement. In this figure the tangential field is configured in such a manner that the fluid flow due to AC electroosmosis moves fluid away from the gap.

An additional effect that must be accounted for is called electro-osmotic flow. Due to the surface charge on the walls of a vessel, there is a double layer established at the boundary, as established in 2.3. Subsequently, the bulk fluid maintains a small net charge, and, thus is subject to Coulombic forces, usually applied via electrodes to inlet and outlet. This tangential/radial flow is described by a 1-D Navier-Stokes equation:

$$\eta \frac{d^2 v_r(z)}{dr^2} = E_z \rho(z),$$

where η, E_z, and ρ are the fluid viscosity, normal electric field component, and charge density, respectively [10]. This may be simplified when far away from the double layer as,

$$\nu = \frac{E_z \sigma}{\kappa \eta};$$

κ^{-1} is the Debye length. Assuming that all excess charge in a double layer exists at the first Debye length and ignoring the diffuse nature of the double layer , as Ramos et al. [11] do, the excess charge follows the relation,

$$\sigma = \frac{\epsilon_m V_{z=\kappa^{-1}}}{\kappa^{-1}}.$$

The tangential electric field, E_r at the first Debye length is thus:

$$E_z = \frac{\partial V_{z=\kappa^{-1}}}{\partial z}$$

It must be noted, however that this effect is only significant when the dimensions of the vessel are very small. Likewise, the flow approximates a plug flow, essentially a flat velocity profile except very near the boundary, whereas a pressure-derived flow will maintain a parabolic velocity profile. An AC stimulus across the length of a microfluidic channel will yield a net-zero flow, but in the case of a planar interdigitated electrode, there can be net forces on electrolytes in the electrode gap as result of interactions with the induced double layers over the electrodes. This results in a tangential flow velocity sweeping across the electrode, moving fluid away from gap. Therefore a circulating flow is established in an electrode array, as shown in Fig 2.4 [11]. The tangential velocity asymptotes to zero at very low frequencies where the electrode is completely polarizable, and thus there is no electric field in the solution, and to zero at high frequencies due to the electric field being dropped entirely across the solution, and thus no double layer is established. It must also be noted that the mobile excess charge of the double layer is inversely proportional to solution conductivity (i.e. the OHL is proportional to the Debye length), so the significance of electroosmosis decreases significantly at higher conductivities [10].

2.5 Electrothermal Effects

Significant thermal gradients can also be established in microelectrode arrays, which, depending on the system, may be the largest driving force affecting particles in solution. The low permeability, especially relative to the permittivity, of materials used and tested in such devices means that magnetic field terms can be ignored and, thus, simpler electrostatic equations adequately describe the system. The energy storage ratios and the characteristic times for electrical and magnetic phenomena, respectively, are as follows [12], [13]:

$$\text{Energy ratio: } \frac{W_M}{W_E} = \frac{(1/2)\mu\mu_0 H^2}{(1/2)\epsilon\epsilon_0 E^2}$$

$$\text{Electrical characteristic time: } \tau_c = \epsilon\epsilon_0\sigma$$

$$\text{Magnetic characteristic time: } \tau_M = \mu\mu_0\sigma l^2$$

For solutions between 1 mS/m ($\tau_C \sim 10^{-6}\ s^{-1}$ and $\tau_M \sim 10^{-17}\ s^{-1}$) to 1 S/m ($\tau_C \sim 10^{-10}\ s^{-1}$ and $\tau_M \sim 10^{-14}\ s^{-1}$) magnetic charateristic time is much smaller than electrical characteristic time, and respective energy storage ratios are very small. Starting from the derivative form of the quasi-electrostatic limit, our governing

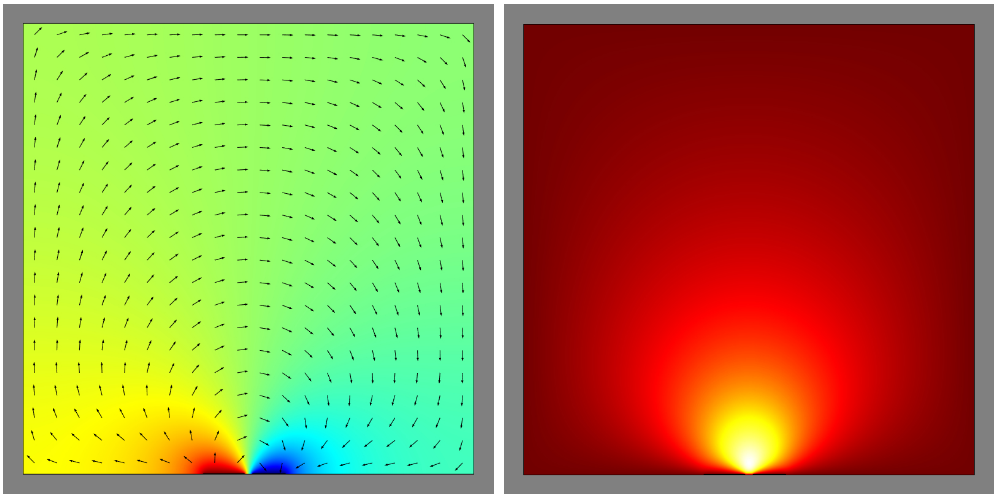

(a) Potential with current direction (b) Temperature

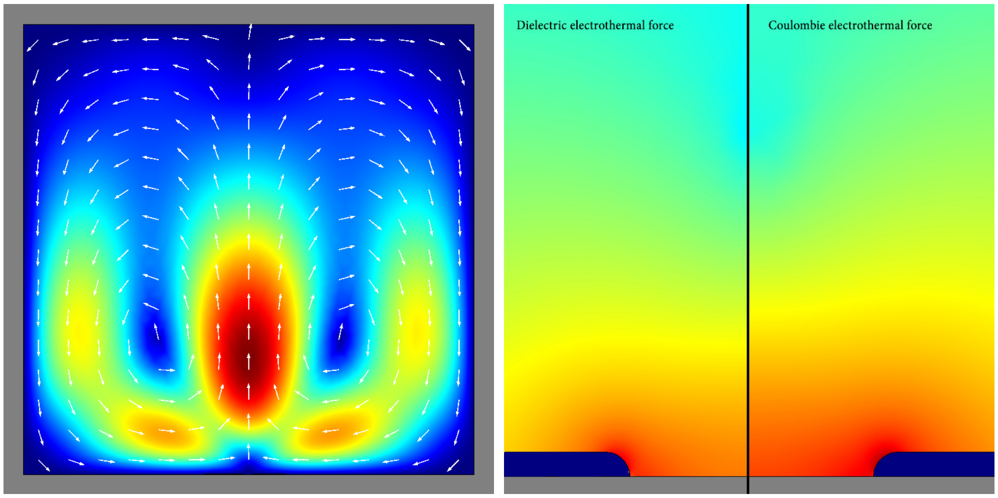

(c) Fluid velocity and direction (d) Electrothermal force magnitudes

Figure 2.5: Simulation of 2 electrodes (50 μm wide, 10 μm gap) in 1.4 S/m aqueous electrolyte driven at 10 kHz and 10 V_{rms}. (a) shows that the potential quickly drops into bulk potential as one moves away from the electrodes, and current flow is circulating around the test window. The temperature plot (b) follows that of the current density, which highest in between the electrodes, causing a plume that radiates outwards and upwards nearly equally due to conduction. Temperature-based density changes in the water create buoyancy forces that displace the warm water upwards, which is balanced by cooler water flowing down the edges and across the electrode surface (c). Zooming in on the electrode gap, (d) is a split plot of the log-scaled magnitude of the force equation 2.12, where the first term is on the right (Coulombic) and the second term is on the left (dielectric). The peak magnitude of the Coulombic force, under these circumstances, is roughly five times greater than the dielectric force. This peak occurs right along the electrodes corners and falls away rapidly from the gap.

equations are [14]:

$$\nabla \cdot \epsilon E = \rho_V$$
$$\nabla \times E = 0$$
$$\nabla \cdot j + \frac{\partial \rho_V}{\partial t} = 0$$

where ρ_V and j are the volume charge density and the bulk electrolyte current density, e.g. $j = \sigma E$. Simplifying to a binary electrolyte [15],

$$j = e(n_+\mu_+ + n_-\mu_-)E - e(D_+\nabla n_+ + D_-\nabla n_-) + e(D_+^T n_+ + D_-^T n_-)\nabla T.$$

The ion mobilities are $\mu_{+/-}$, $D_{+/-}$ are the ion diffusivities, and n_+ and n_- are the positive and negative ion densities, respectively. $D_{+/-}^T$ are the thermal diffusion constants, ∇T is the temperature gradient and e is the elementary charge constant. The above equation assumes monovalent ions, and in the circumstances of an electrolyte such as saline, the equation may be further simplified, as many of the constants may be reduced to a common term for both the positive and negative ion.

The Peclet number, i.e. the ratio between advective and diffusive transport,

$$P_{eL} = \frac{L\nu}{\alpha}, \text{ where thermal diffusivity is } \alpha = \frac{k}{\rho c_p}$$

is dominated by diffusion, so convection may be ignored for most microfluidics. The characteristic length of the system, L, is on the order of the system's dimension; for microfluidic applications, L is in the range of tens to hundreds of micrometers. ν is typical velocities experienced, which max out in the mm/s range, κ is the thermal conductivity, ρ the density and c_p the heat capacity. Likewise, drift current dominates both electrical and thermal diffusion terms.

To simplify the system, one may assume that electrolyte concentration gradients in the bulk solution are small, especially under low potential and $\omega \gg \frac{\sigma \lambda_D}{\epsilon l}$. For very low concentration solutions, this frequency may be in the kHz range, but for biological fluids the conductivity dominates, this approximation only reliably holds in when $\omega \gg 1$ MHz (let us assume $\sigma \sim 1$ S/m, $\lambda_D \sim 10^{-9}$ m, $\epsilon \sim 10^{-10}$ F/m, and $l \sim 10^{-6}$ m, therefore $\omega \gg 1$ MHz). Likewise, for high conductivity solutions, the bulk is electrically neutral on micron scales, as it may be estimated by $\Lambda = \epsilon E/eln_+ \sim 0$ as a proxy for $(n_+ - n_-)/n_+ = \nabla \cdot (\epsilon E)/en_+$ [13].

At small temperature gradients, the gradients in conductivity and permittivity are small, so the nominally complex solution to the quasi-electrostatic equations may be expanded and simplified as [12]:

$$\nabla \cdot ((\sigma + j\omega\epsilon)E) = 0; \tag{2.7}$$

$$\text{let} \quad E = E_0 + E_1 \quad \text{where} \quad E_1 \ll E_0;$$

$$\nabla \cdot E_0 = 0 \text{ and} \tag{2.8}$$

$$\nabla \cdot E_1 + \left(\frac{\nabla\sigma + j\omega\nabla\epsilon}{\sigma + j\omega\epsilon} \right) \cdot E_0 = 0. \tag{2.9}$$

Charge densities for the respective electric field superpositions may be written as,

$$\rho_0 = \epsilon \nabla \cdot E_0 = 0 \tag{2.10}$$

$$\rho_1 = \epsilon \nabla \cdot E_1 + \nabla\epsilon \cdot E_0 = \left(\frac{\sigma\nabla\epsilon - \epsilon\nabla\sigma}{\sigma + j\omega\epsilon} \right) \cdot E_0. \tag{2.11}$$

If the conductivity and permittivity gradient terms are very small, the overall solution may be simplified to E_0, in which case one may start from Laplace's equation: $\nabla^2 \phi_0 = 0$.

Starting from the Navier-Stokes relation for incompressible fluids, which may be separated into inertial, pressure, viscous, electrical, and gravitational forces, respectively [12],

$$\begin{aligned}
&\nabla \cdot u = 0 \\
&\rho_m \left(\frac{\partial u}{\partial t} + u \cdot \nabla u \right) = -\nabla p + \nabla \cdot \mu \left(\nabla u + (\nabla u)^T \right) + f_{elec} + \rho_m g.
\end{aligned}$$

Again, since the convective term is small, we may ignore the inertial contribution, and simplify to

$$0 = -\nabla p + \nabla \cdot \mu \left(\nabla u + (\nabla u)^T \right) + f_{elec} + \rho_m g.$$

While there are oscillatory effects due to AC electrical heating, the time averaged velocity field is

$$0 = -\nabla p + \eta \nabla^2 u + \langle f_{elec} \rangle + \Delta \rho_m g;$$

a Boussinesq buoyancy approximation has been applied due to the nearly-homogeneous mass density [12]. Lastly, the average electrical force due to an applied AC field is due to the contributions of Coulombic and dielectric forces:

$$\langle f_{elec} \rangle = \frac{1}{2} Re(\rho_q E^*) - \frac{1}{4} E \cdot E^* \nabla \epsilon, \tag{2.12}$$

and substituting the respective charge densitites from 2.10 and 2.11,

$$\langle f_{elec} \rangle = \frac{1}{2} Re \left(\left(\left(\frac{\sigma \nabla \epsilon - \epsilon \nabla \sigma}{\sigma + j\omega\epsilon} \right) \cdot E_0 \right) E_0^* \right) - \frac{1}{4} E_0 \cdot E_0^* \nabla \epsilon. \tag{2.13}$$

Notable is the importance of frequency on the electrical force, as the conductivity and permittivity terms themselves are frequency-dependent, but also the proportional contributions of either the Coulombic force ($\sigma/\epsilon \ll \omega$) or dielectric force ($\sigma/\epsilon \gg \omega$), since the variation in conductivity due to temperature is roughly 20 times the variation in permittivity due to temperature for electrolyte systems. The proportion of σ to ϵ also determines the driving force in the equation, as in the case of pure water, the system will be almost purely driven by ϵ and $\nabla\sigma$ and by σ and $\nabla\epsilon$ in a high conductance solution.

To define the thermal energy equation, let us start with the general convection-diffusion equation:

$$\frac{\partial T}{\partial t} = \nabla \cdot (k\nabla T) - \nabla \cdot (\vec{v}T) + P_{elec}(t),$$

where T is temperature, t is time, k is the thermal diffusion coefficient $\vec{v}$ is convective velocity, and $P_{elec}(t)$ is the electrically-derived heat loss. If we assume that convection is very small and Joule heating ($P_{elec}(t) = \sigma E^2$), then we can simplify to the time-averaged Poisson's equation [16]:

$$k\nabla^2 T + \sigma\langle E^2\rangle = 0.$$

Ultimately, this allows us to derive some rules and relationships that are more useful to the design of electrokinetic devices [6], [12]. First,

$$\Delta T \sim \frac{\sigma V_{rms}^2}{\kappa} \quad \text{or} \quad \frac{\kappa \Delta T}{l^2} \sim \frac{\sigma V^2}{2l^2}$$

indicates that we may achieve large thermal gradients at small voltage differences, which confers great benefit, by reducing the dimensions of the device. Second, any system must be designed with the expected fluid conductivity in mind, as Joule heating is directly proportional to conductivity. The proportion the system is influenced by electrothermal effects is strongly dependent on the fluid conductivity:

at low conductivity solutions, electroosmotic and dielectrophoretic forces will be proportionally stronger in comparison with high conductivity solutions. Third, flow direction is critically important, as it may augment or impede the desired direction of fluid and particle movement within a system. All of these contributing forces must be accounted for during device design.

Chapter 3

Platinum corrosion in biologically-relevant solutions

3.1 Introduction

Diagnostic timeliness, whether due to marker integrity [17], [18] or clinical immediacy, challenges the present clinical laboratory milieu. Greater performance and reliability is expected of materials to keep up with the development and expansion of lab-on-a-chip devices, constant miniaturization and automation of laboratory tests; and increasing number of implanted electronic devices. Even in vitro there is a growing desire to direct sample body fluids, albeit difficult [19], as sample preparation is brought on-chip or made unnecessary by device design [20]–[23]. Since body fluids are corrosive and safety is paramount, the breadth of research into biomaterial corrosion resistance is extremely wide but with a clear focus in structural implants, stents, and dental applications. Materials used for active electrodes, typically platinum, platinum-iridium alloys, and gold; have seen less attention although corrosion of neural implants has been investigated on several occasions [24]–[33]. This said, none of this work has looked at electrode corrosion effects at higher current densities, especially those resulting from potentials greater than the oxidation potential of water, as might be found in an in vitro electrophoretic, dielectrophoretic, or electrochemical lab-on-a-chip device, e.g. [26], [34], [35]. Likewise, micron-scale devices are more likely to suffer from corrosion due to small geometries, microelectronic fabrication methods, and proportionally lower potential loss across the fluid than large-scale devices. This study examines the effects of platinum corrosion in biologically-relevant solutions, as applicable to lab-on-chip-sized devices.

3.2 Methods

To simulate geometries that might be found in lab-on-a-chip devices, small circular wells were made in polytetrafluoroethylene (PTFE) blocks and spanned by three 100 μm diameter 99.99% platinum wires (Sigma Aldrich). Device is shown in Figure 3.1. The diameter of the well is $\frac{3}{8}$ inch ($\sim$ 9.5 mm) and $\frac{3}{16}$ deep ($\sim$ 4.75 mm); the wires are spaced on 0.015 inch center-to-center ($\sim$ 381 μm) through the middle of the well, both width- and depth-wise. Wires are held under tension and glued in place with cyanoacrylate glue (Scotch single use) and cured overnight in a 60 °C oven before use. While the ends of the well are firmly affixed, small variations in inter-wire spacing are noted, as result of fabrication imperfections. Devices are cleaned by filling the well with reagent-grade H_2SO_4 for 10 minutes rinsed thoroughly in 1 $M\Omega$ deionized water and dried in an $\sim 60 - 70$ °C oven for at least 30 minutes before use. Due to the small contact area between the fluid and the glue, minimal chemical attack of the glue is observed. Uncoated planar electrode arrays consisting of a checkerboard pattern of 60 μm diameter circular pads on a 150 μm center-to-center spacing were purchased from Biological Dynamics (La

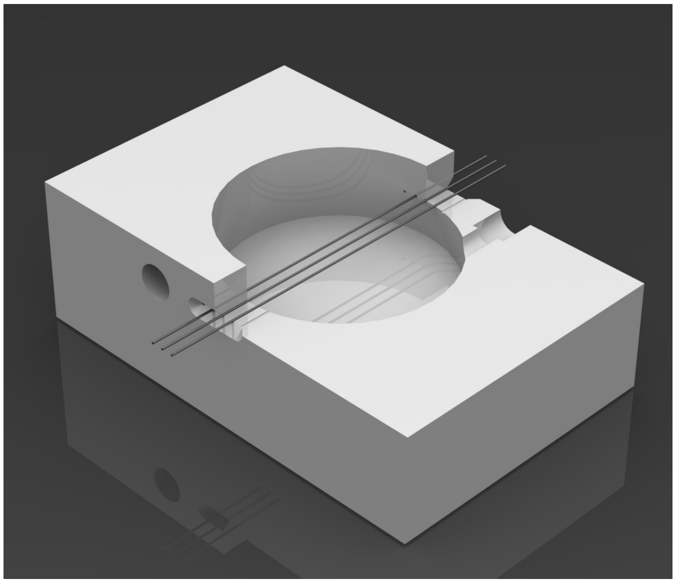

Figure 3.1: Rendered cross-section of the wire well device. 3 wires are suspended through the center of the $\frac{3}{8}$ inch diameter by $\frac{3}{16}$ inch deep well on 0.015 inch wire-to-wire spacing. The wires themselves are 100 μm in diameter.

Jolla, CA), and used with no further preparation.

A solution of pH 7.4 10x phosphate buffered saline (VWR International) is diluted to a 0.5x PBS final concentration with 1 $M\Omega$ deionized water to roughly simulate the conductivity and salinity of common biological fluids, e.g. blood, plasma, cerebrospinal fluid, and urine. 180 μl of solution is to fill the wire-well devices and 35 μl is needed for the planar electrode devices. To power the system, an HP/Agilent 33120 signal generator is connected to an amplifier (Newtons4th LPA01) and, subsequently, to the device under test. The wire-based device is configured with the inner wire connected to the opposite polarity of the outer wires, and the planar electrodes are powered in a checkerboard polarity pattern. Temperature was not measured nor controlled; in use the planar device is mounted on $\sim 10\frac{°C}{W}$ heatsink without any thermal interface material. Wire-based devices are mounted on a glass substrate, but, given the thickness of the PTFE walls, the majority of the generated heat is assumed to be lost through evaporative cooling and passive convection.

The devices were observed under an Olympus BX51WI microscope and Olympus DP71 camera controlled with Olympus's DP Manager software. For planar devices, sinusoidal drive voltage (1 kHz) was stepped from 10 $V_{peak-peak}$ (V_{pp}) through 20 V_{pp} in 2 V per $\sim$ 5 minute steps, and 1.5 V_{pp}, 4.5 V_{pp}, and 10 V_{pp} steps were used at 100 Hz. Wire-based electrodes were stepped up to 28 V_{pp} (maximum output of amplifier) in less than 30 seconds and allowed to remain for 5 minutes or until platinum black was observed. If no degradation of the wires was observed, frequency was lowered to 100 Hz and same steps were repeated. After voltage stepping, the parts were flushed with deionized water to remove any precipitated salt and then disassembled. A razor blade was used to carefully separate the glued-on cover of the planar device, and then soaked in deionized before drying in a $\sim 60 - 70$ °C oven. The wire-based devices were first immersed in acetone to dissolve the Cyanoacrylate glue, whereupon the wires were carefully removed with tweezers. The wires were subsequently rinsed with acetone to remove any residue, then soaked in ethanol and deionized water before drying in a $\sim 60-70$ °C oven. Scanning electron microscope (SEM) images were taken on a FEI/Philips XL30 ESEM.

3.3 Results

3.3.1 Wire Electrode Devices

An etched wire in solution after a run at 10 V_{pp}, 100 Hz is seen in Fig. 3.2, where aggregates are still loosely attached to the center wire (rightmost wire not shown). Figures 3.3 through 3.5 shows SEM images of a Pt wire tested for corrosion. Figure 3.3 is the same wire in a region outside the submerged well;

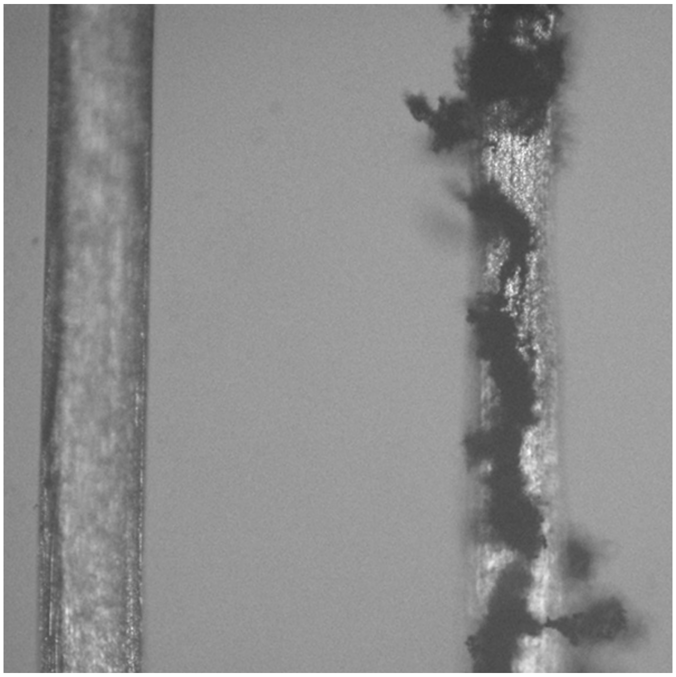

Figure 3.2: Left and center wires of a 3-wire device in 1x PBS after application of 100 Hz, 10 V_{pp} for less than 30s. The black tendril-like aggregates loosely attached to the surface of the central wire are formed from platinum nanoparticles that etched off the surface of the wire.

there are a number of dents and scratches on the surface of the wire from device assembly due to platinum's softness, but the wire is smooth in unaffected regions. Figure 3.4 shows the effects of rapid-onset corrosion due to use at 100 Hz and 10 V_{pp}. Voltage required to induce rapid corrosion was highly variable based on the electrode surface and length of tests during voltage stepping (not shown): rougher wires corrode at lower voltage, as would be expected from greater surface area and regions where coordination reactions are favorable. Longer, slower sweeps to maximum voltage increase the solution temperature, thus enhancing reaction kinetics. Therefore corrosion begins at lower voltage, albeit at greatly reduced rate.

A voltage slightly above that used for dielectrophoretic separations was chosen to accelerate corrosion. Substantial hydrolysis and gas formation between

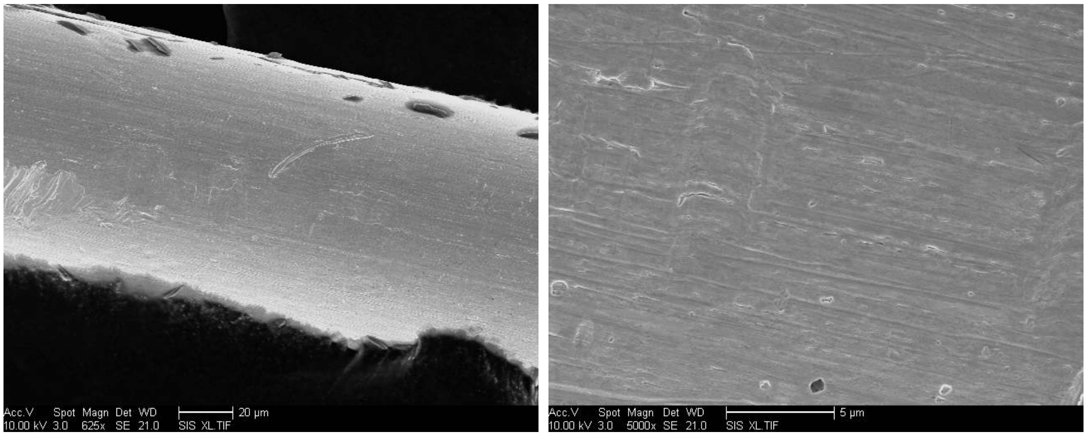

Figure 3.3: SEM of a 100 μm Pt wire in an unused region of a wire-based device. Given the softness of pure Pt, there are scratches from assembly, but the overall surface is largely smooth. Dark spots are from graphite mounting tape.

the electrodes is observed at these potentials, obviating its use in diagnostics. Similarly, the solution quickly turns dark brown from dissolved $PtCl_x$ and possibly PtO_x complexes. Surface morphology is similar to that derived from Pt-black or platinization depositions where aggregated metallic platinum nanoparticles form on the surface due to the favorable energetics of Pt-Cl coordination complexes. Optically, these regions appear black, owing to internal reflections, which scatter and attenuate incident light. These Pt-nanoparticle aggregates suffer poor surface adhesion and are largely displaced from the wire surface due to sheer forces resulting from electrothermally-derived flow around the wires and from gas bubbles forming and collapsing. Pt-nanoparticles experience positive dielectrophoretic forces that, in lower flow regions near the edges of the well form into large, extremely delicate, and tendril-like aggregates that nearly bridge the gaps between the wires. As expected due to the rapid growth of surface area, the evolution of gas and corrosion increase over time [36]. Similar results were found using blood plasma samples as with 0.5x PBS samples.

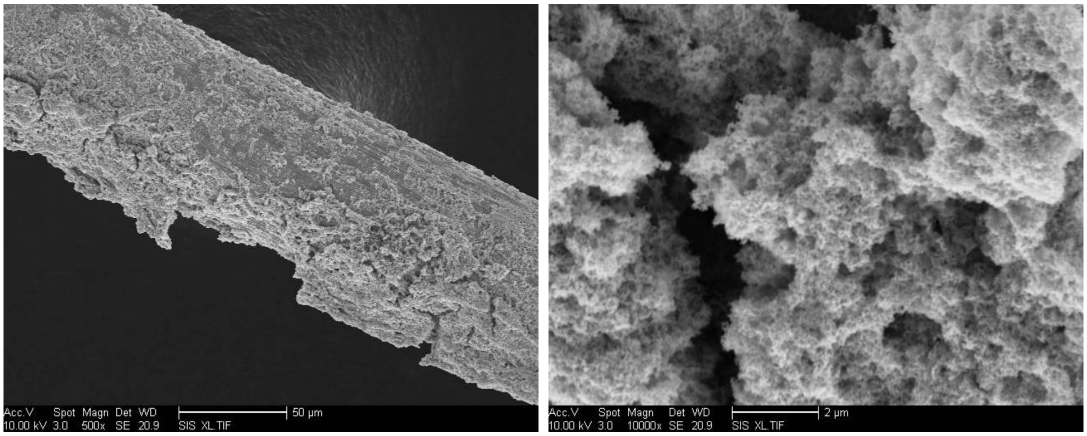

Figure 3.4: SEM of a 100 μm Pt wire after rapid corrosion from an AC signal (10 V_{pp} 100 Hz, alternating wire polarity), in a region where aggregated Pt nanoparticles remained adhered to the wire surface. While the particles in these images are very small, the size varies significantly over the surface of the wires.

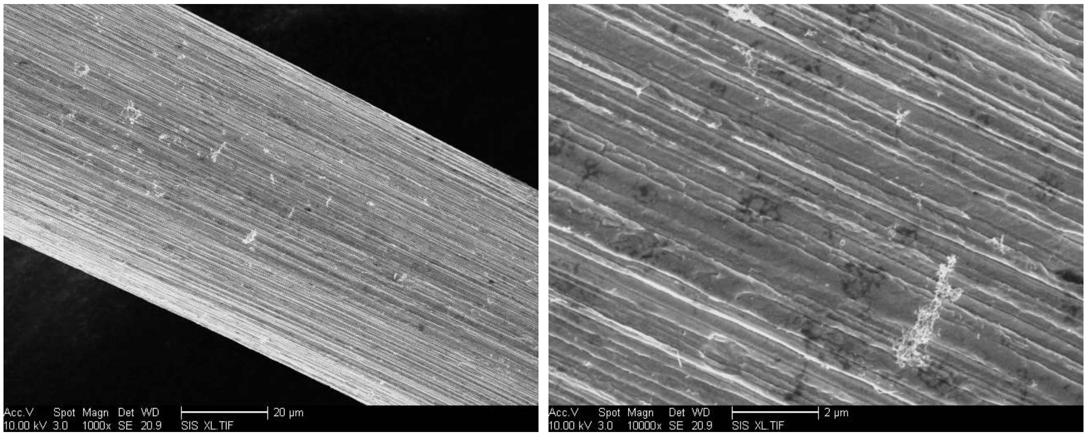

Figure 3.5: SEM of a wire-based device immersed in 0.5x PBS driven at 10 V_{pp} 100 Hz, whereupon rapid corrosion was observed. Due to local flow conditions around the wire, subsequent cleaning steps, and the overarching fragility of the aggregated Pt nanoparticle debris, there are several regions where the underlying Pt wire surface is largely clean. As seen in more clearly here than in regions still coated with aggregates, the wires appear striated along the primary wire axis. It is undetermined whether that is due to small surface defects in the as-formed wire, or due to preferential coordination reactions, although the latter is suspected.

Figure 3.5 shows a region with few Pt-nanoparticles and, thus, significant striations along the wire axis in the wire beneath are evident. The electric field in the wire electrode geometry is axially uniform over its length; wire resistance ($\sim 0.4\ \Omega$ for a 3 cm 100 μm diameter wire) and self-inductance ($\sim$ 38 nH) are very small compared to the inter-wire impedance, so effectively potential across the wire's length can be assumed to be uniform. Uniform axial striations are consistently observed over the length of the wire. Current density in this configuration is

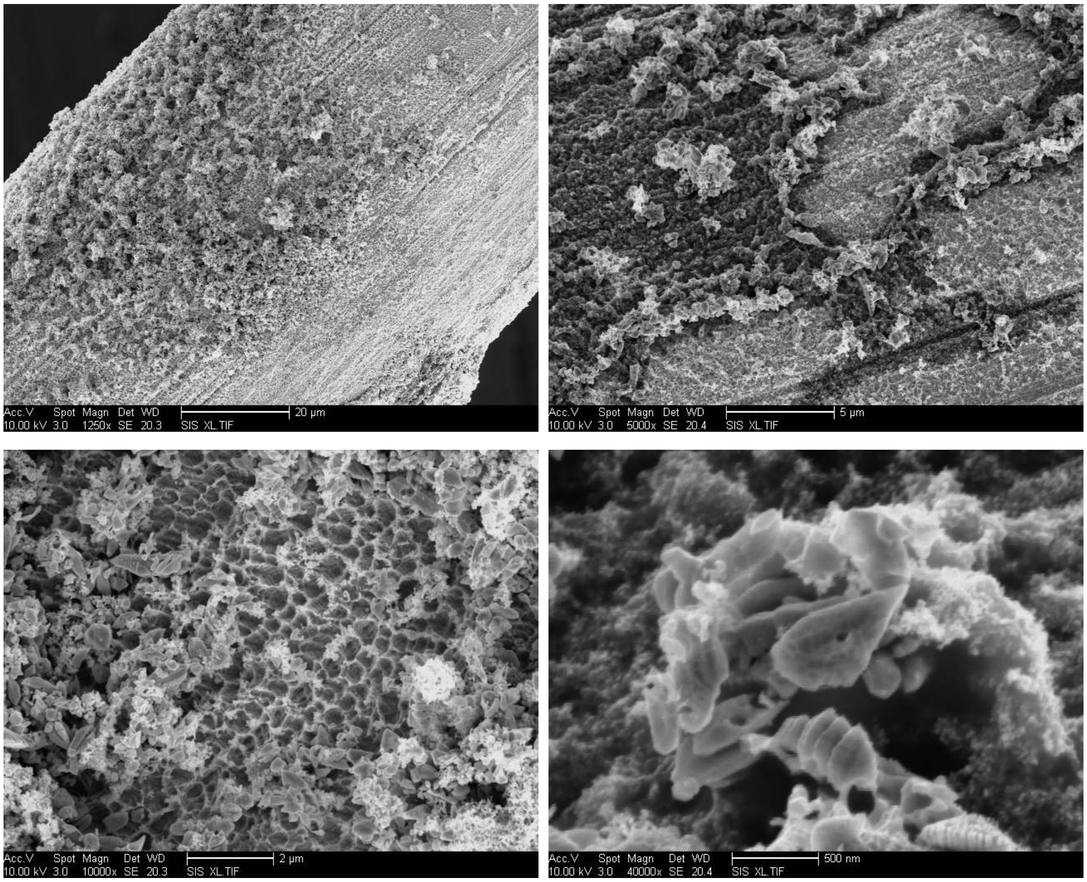

Figure 3.6: The center wire of a wire-based device connected as the anode to a 14 V_{DC} power supply, far in excess of that needed to corrode the Pt in 0.5x PBS. Outer wires, connected as cathodes, experienced no surface etching, strongly suggesting the corrosion reactions are chlorine-driven, correlating with data presented by Llopis [37]. Platinum nanoparticle aggregates observed on the corroded surface are similar in morphology and size range to those found on corroded wires held under AC stimulation.

distributed over the length, but skin depth at low frequency (≤ 1 MHz) is much larger than the wire radius. Thus, surface current is almost exclusively radial in nature. It is therefore assumed this is due primarily to the grain alignment of the platinum wire and preferential adsorption and reaction kinetics along grain boundaries rather than due to localized current effects.

DC-biased corrosion was also tested on wire electrodes: minimal effects were found at potentials equivalent to the AC RMS voltages due to static passivation of the respective surfaces and nonlinear I-V curves, but when $V_{DC} = V_{AC,PP}$, DC biased anodes were driven into rapid corrosion, faster than that found at the same peak-to-peak AC potential. As seen in Fig. 3.3.1, similar morphology and striations are found on the wire surface for both AC and DC stimulus. No observable etching was noted in identical tests using 1 MΩ deionized water nor 30 % commercial H_2O_2 (Sigma Aldrich).

Since the Faradaic impedance of a Pt-PBS cell decreases with increasing frequency [38], [39] and corrosion is observed to dramatically decrease [40], tests

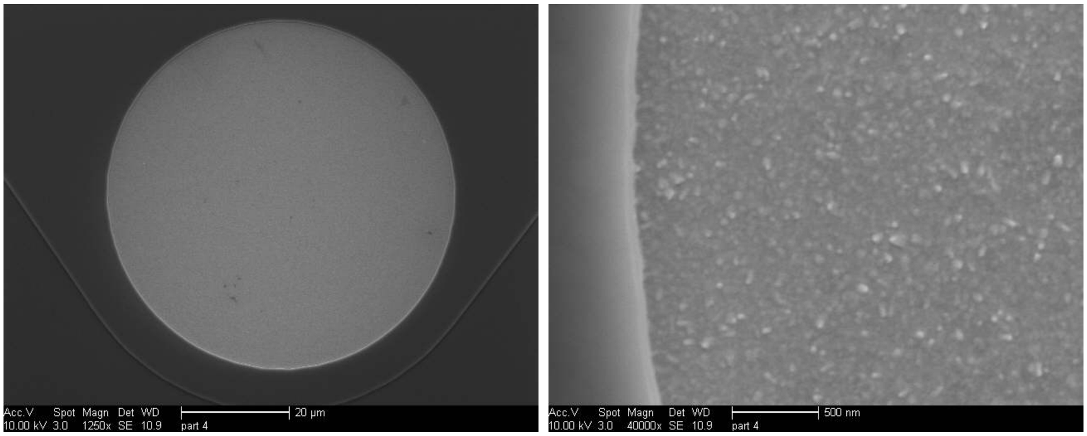

Figure 3.7: SEM images of an unused Pt planar electrode: a window in the SiO_2-coated surface to underlying Pt-Ti trace forms the electrode. The electrode surface appears continuous and largely smooth with some small grain formation effects due to sputter deposition.

were run at 10 kHz, 100 kHz and 1 MHz. Voltage was stepped from 4 V$_{pp}$ to 24 V$_{pp}$ in 4 V steps: 3 minute on, 2 minutes off to allow for cool down. As expected from the low Faradaic impedance, mass transport to/from the electrode-electrolyte interface is reduced, greater power is lost to the solution, and, thus, substantial evaporation and gas evolution are observed. The well was flushed with DI water and fresh 0.5x PBS was used after both the 16 V$_{pp}$ steps and the 20 V$_{pp}$ steps as result of evaporative loss during these sub-tests. While no visible pitting on the surface of the wires was observed, bubbling becomes so severe at 24 V$_{pp}$ that the experiment are terminated before the full 3 minutes expired. 1 MHz tests behaved the same as 100 kHz, but notable etching of the wire surface is observed at 10 kHz half way into the 20 V$_{pp}$ step, so tests were terminated. This is consistent with prior literature and demonstrates the importance of frequency selection on device performance and longevity.

3.3.2 Planar Electrode Array Devices

To test other geometries relevant to lab-on-a-chip devices, Figure 3.7 shows an overhead SEM of a planar electrokinetic device. The electrodes are formed by etching a window through a SiO_2 coating to the sputtered Ti-Pt metal layer beneath the oxide. The square grid of these circular electrodes are connected to alternating polarities in a checkerboard pattern, but, in essence, the electrode array is a series interdigitated platinum strips with periodically placed circular windows in the insulation to form the active electrode area. The electrode surface is smooth and bright, with some small grain formation evident at higher magnifications. Figure 3.8 is a series of brightfield images of a planar electrode, immersed in 0.5x PBS, stepped from 14 V$_{pp}$ to 20 V$_{pp}$ in roughly 5 minute intervals. The left side of Fig. 3.8b is an unpowered region of the device, Fig. 3.8a, Fig. 3.8c, and Fig. 3.8d

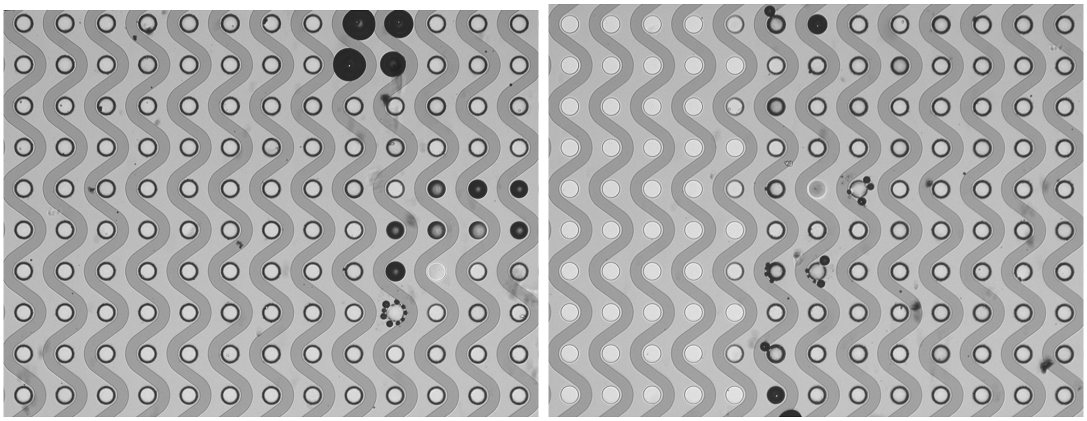

(a) 14 V$_{pp}$, 1 kHz (b) 16 V$_{pp}$, 1 kHz

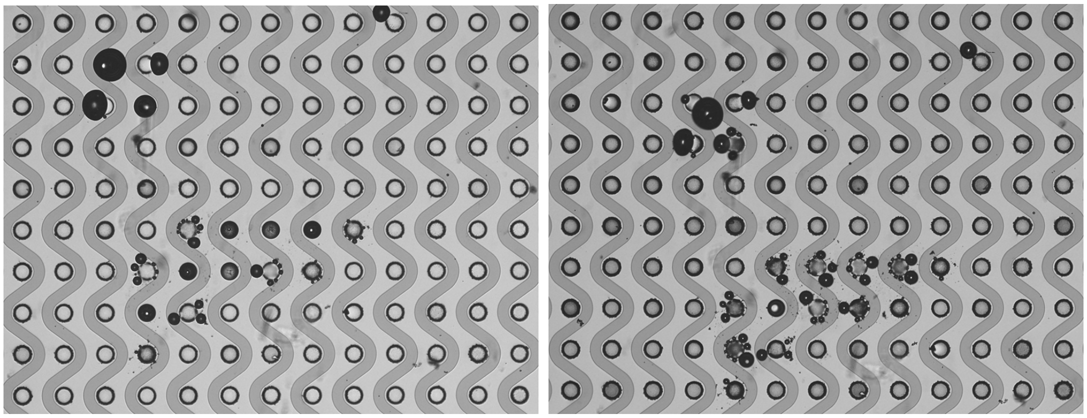

(c) 18 V$_{pp}$, 1 kHz (d) 20 V$_{pp}$, 1 kHz

Figure 3.8: Brightfield microscope images of a planar electrode immersed in 0.5x PBS during operation at 14 V$_{pp}$, 16 V$_{pp}$, 18 V$_{pp}$, 20 V$_{pp}$ at 1 kHz, stepped in $\sim$ 5 minute intervals. The small circles are the active electrode surfaces, and are powered in a checkerboard pattern. For reference, an unpowered region of the planar electrode is shown on the left third of Figure 3.8b, where there is no dark outline around the circumference of each respective electrode. A small amount of bubbling is noted at 14 V$_{pp}$, and increases with voltage, as expected from the electrolysis of hydrogen, chlorine, and possibly a small amount of oxygen. At 18 V$_{pp}$, electrodes are observed to corrode in localized regions of the chip. This is noted by the roughened electrodes, which appear darker due to scattering light away from the microscope objective, and the appearance of small particles in inactive regions of the chip. By 20 V$_{pp}$, the extent of the electrode degradation has increased significantly. Drive voltage between wire and planar devices are not directly comparable.

are images wholly of the active region. Bubbles seen in Fig. 3.8a emerged at the initial 10 V_{pp} stimulus and remained stable until new bubbles began to form at ≥ 18 V_{pp}, and therefore the images from 10 V_{pp} and 12 V_{pp} are omitted, as they are functionally identical to Fig. 3.8a. At 18 V_{pp}, a few electrodes appear dark in isolated regions, due to roughening of the surface, and dramatically increases at 20 V_{pp}, becoming largely uniform over the active surface.

Voltage levels between the wire electrodes above and planar electrodes are not directly comparable, as the voltage losses from amplifier to planar electrode surface are substantially higher than along the wire, both from trace resistance and contact resistance within the electrical harness to the chip. Similarly, the different geometries will dramatically change the current pathways and have different abilities to manage heat; consequently, corrosive effects will manifest differently on different devices, even though the same basic electrochemistry is the driving mechanism.

Figure 3.9 shows the effects on planar electrodes at 100 Hz, stepping from 1.5 V_{pp} to 10 V_{pp}. Low frequency modulation, e.g. 50 Hz or lower, and with DC bias [39] or without [41], is shown to drastically increase corrosion. Similar effects are not found at higher frequencies, due to heavy mediation by the nature of the electrode-electrolyte interface, slow reaction kinetics for both passivation and de-passivation, and the lack of mass transport towards and away from the electrode surface [42]. As expected, while minimal effects were seen at lower voltages, albeit by optical observation, 10 V_{pp} at 100 Hz causes significant bubbling and corrosion on the electrode surface. Figure 3.9c shows the effect on the electrodes, after the voltage was removed, whereupon the entire active region is completely corroded.

Figure 3.10 shows the effect of burning out the electrodes. The surface first fails at the SiO_2 interface, where the field and current density are highest. Along the edge of the electrode, larger particles are observed; as seen in Figure

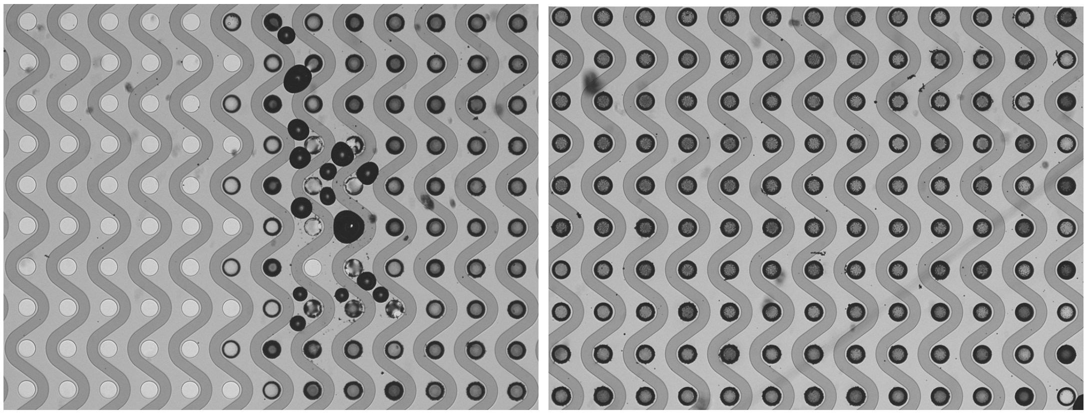

(a) 1.5 V_{pp}, 100 Hz

(b) 4.5 V_{pp}, 100 Hz

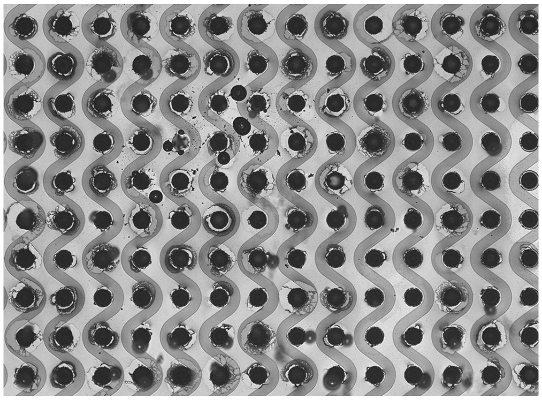

(c) 10 V_{pp}, 100 Hz

Figure 3.9: Brightfield microscope images of a planar electrode stepped across 1.5 V_{pp}, 4.5 V_{pp}, and 10 V_{pp} at 100 Hz. The 0.5x PBS was exchanged and the chip was allowed to cool between the 1 kHz and the 100 Hz tests. An un-powered region of the planar electrode is seen Figure 3.9a on the left half. Comparing intact regions of Figure 3.9a and Figure 3.9b to Figure 3.8d, only a slight darkening/roughening in the electrode surface is seen.

3.10b, these particles appear to remain clumped near the receding metallized edge. Due to the higher fields and current density at the outer circumference of the electrode, breakdown occurs there first and then migrates inward. Eventually, the entire electrode experiences corrosion; the reformed surface, albeit cracked and fragmented, remains sufficiently conductive as to not fail to an open circuit. Platinum nanoparticles are found to experience positive dielectrophoresis in 0.5x PBS in the range of 100 Hz to 10 kHz, so this is the most probable reason for the

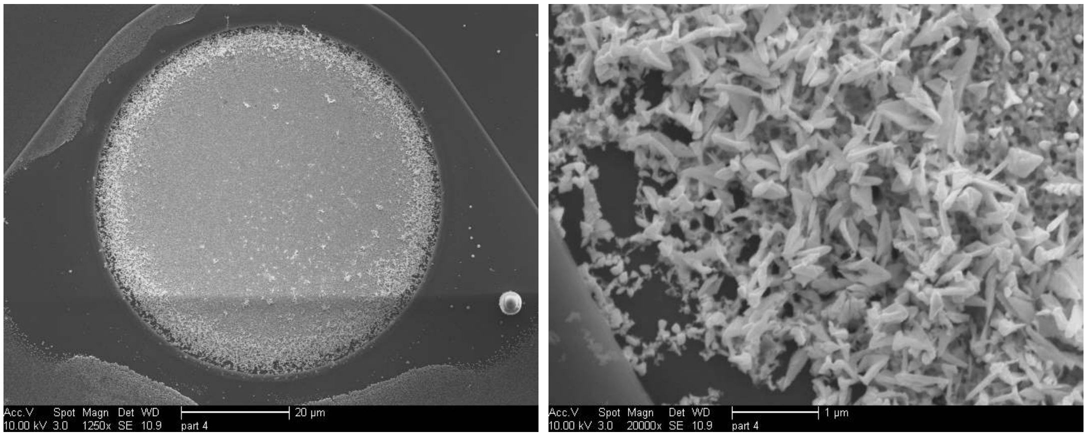

(a) Corroded electrode; the lighter parts around the periphery are dried residue.

(b) Electrode window edge, lower left corner shows undercutting of insulator.

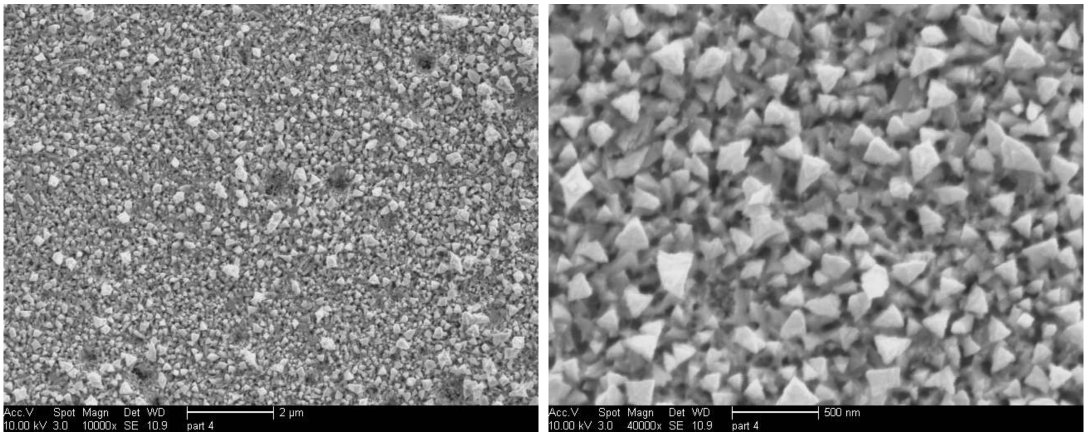

(c) Electrode center showing significant roughening and particle formation.

(d) Electrode center detail, showing particle size and morphology.

Figure 3.10: SEM images of a corroded Pt planar electrode; there is a notable differenced in the morphology in the center versus at the edges. Electric field, and therefore current, is greatest at the pad-insulator interface and relatively uniform over the remainder of the electrode, yielding different local environments. Both the Pt and Ti under-layer are almost completely removed from the Si substrate around the edge, with material piled up along the inward-propagating edge.

aggregation of Pt at the edge. Electromigration and/or local electrophoresis may possibly contribute, but unlikely, given the AC stimulus and particles solely moving towards the center of the electrode [43]. Electromigration may accelerate reformation of the smooth surface into the granular surface observed. Throughout the center of the electrode, morphology has fragmented into still-adhered nanoparticles, primarily triangular in shape, and the Si substrate below is visible in the gaps between particles. Figure 3.10c clearly shows the surface roughening, and Figure 3.10d shows the nanoparticle formation in detail.

Similarly interesting is the undercutting of the platinum at the edge of its patterning. As can be seen in Fig. 3.10a along the upper left edge, there is a significant roughening of the platinum underneath the SiO_2 coating. This suggests that the oxide layer is not completely conformal as it steps from the Si to the Pt layer, allowing for electrolyte ingress and, thus, corrosion at these weak spots. Like wire-based tests, no corrosion in duplicated tests using 1 MΩ deionized water or 30 % commercial H_2O_2 was observed.

3.4 Discussion

Platinum electrodes, when immersed in a chlorine-containing solutions will form a stable platinum-chloride passivation layer. High overpotential voltages, under either DC stimulus or low-frequency AC stimulus, will cause the platinum surface to corrode. While platinum electrodes are commonly and reliably used for a number of bio-electrical applications, it must be emphasized that it requires substantial heat and available specific reactive species to corrode their surfaces, both factors available in a biological solution biased microfluidic systems using large voltages to achieve their desired effect. Mass transport under higher frequency stimulus is limited and reaction kinetics of passivation and de-passivation, on their respective cycles, become too slow as frequency increases above audio frequencies. Thus, the amount of overpotential tolerated by the electrodes without corrosion increases with frequency, even though there is substantially greater Joule heating of the solution due to lower effective impedance between the electrodes, [44] which accelerates reaction kinetics.

Prior research into platinum electrode corrosion has typically focused on potentials at or below the reduction potential of water (~ -1.23 V) in various aqueous acids and at relatively low current densities [32], [33], [37], [39]–[42], [45]–[49]. Llopis and Sancho examined Pt corrosion in hydrochloric acid solutions under low frequency AC current stimulus (50 Hz sinusoid, and 10 Hz square wave) and observe that corrosion is critically dependent on the removal of surface passivation [41]. Sufficiently high DC bias relative to AC modulation limits mass transport away from the interface, as does increasing the modulation frequency. Juchniewicz's results using 3% and 10% NaCl aqueous solutions corroborated with tests using HCl solutions [39], [47].

Sodium hypochlorite and other reactive oxygen and chlorine species evolving off the electrodes is of concern as well, given their efficacy in degrading biological samples [50]. Evolution rates are drastically lower at current densities typically found in microfluidic systems, but long tests may accumulate to a significant concentration [39]. To date, no studies into oxidative damage to RNA or DNA in a microfluidic electrokinetic cell have been reported, but this does remain a concern.

Benke and Gnot further examine dissolution of platinum in HCl, H_2SO_4, and KOH under various conditions and stimulus [51]. Their findings corroborate with those found here: namely, chlorine concentration, temperature, frequency, and current density are the key determinants behind platinum dissolution. Unfortunately, chlorine concentration is uncontrolled in biological solutions, albeit within typical ranges, but an emphasis on cooling and electrode design that minimizes voltage requirements can mitigate corrosive effects dramatically. Likewise, frequency choice is one that should be made carefully: depending on the process, e.g. dielectrophoretic separations of small biological particulate and cellular fragments, the maximum separation peak is fairly broad, so choosing and designing one's device for higher frequency will likely yield greater system reliability and possibly allow for a wider drive voltage margin, depending on ones design compromises.

3.5 Conclusion

A series of tests to examine the effects of corrosion on platinum electrodes were conducted. Two electrode geometries were tested in 0.5x PBS: first was a three parallel wires in close proximity, the second was a planar structure of checkerboard-arranged electrodes. With sufficient overpotential, albeit not much greater than the working voltages of these devices for dielectrophoretic separations, the platinum will experience rapid corrosion and surface reformation due to abundantly available chlorine and high temperatures due to Joule heating. This causes both surface conformation changes as Pt nanoparticles are formed and dissolution of the Pt electrode. Platinum-chlorine reaction kinetics, along with transport of reactants and products to/from the platinum-electrolyte interface, become rate-limiting steps in this corrosion as frequency increases. Knowledge of these limitations to platinum electrodes and their mechanism of failure in biologically-relevant solutions will allow future device designers insight into design constraints and methods to mitigate the issue.

Chapter 3, in full, is being prepared for publication submission. Heineck, Daniel P.; Kim, Sejung; Heller, Michael J. The dissertation author is the primary investigator and author of the material herein.

Chapter 4

High-conductance electrokinetic phenomena

An era of increasingly individualized care based on biomarker analysis is upon us. As result, there is a strong push to make blood/biological fluid testing more widespread, but direct testing generally proves difficult due to most tests requiring substantial sample preparation. Not only does this increase cost and need for laboratory space and specialized labor; but low yields and long pipelines are non-ideal due to marker degradation and increases the needed sensitivity of downstream processing [18]. In general, a substantial percentage of the overall process is tied up in preparation, especially in terms of human labor and equipment, whereas amplification and analysis steps tend to already be automated.

Instead, isolation and preservation of valuable biomarkers must be automated and conducted soon after samples are taken, ideally in the form of a point-of-care device or stand-alone benchtop system. Direct sampling of biological products, especially from a small, disposable, part that can be readily adopted into a diagnostic pipeline is a must if the field of molecular diagnostics is to enjoy substantial growth and progress beyond its present extremely specialized tools and expensive clinical laboratory infrastructure. Electrokinetic separation devices offer tremendous promise in terms of miniaturization and direct separation of targeted biomarkers without the need to go through centrifugation, chemical isolation, and precipitation steps. Considerable effort has been spent on direct capture of circulating-tumor DNA for cancer diagnostics [35], [52], [53]. Ibsen, et. al, recover drug delivery nanoparticles from blood for subsequent analysis [54]. There is also research into using DEP to concentrate relevant biomarkers for chemical assay [55]–[58]. Much of the published efforts into electrokinetic separations for diagnostics has been focused in cell sorting, e.g., [59]–[64].

A major stumbling block for electrokinetic devices is their general need to operate on low-conductance solutions, which, in turn requires either enrichment via mechanical or chemical isolation, e.g. precipitation or centrifugation, and re-suspension in a low-conductance buffer, or a simple dilution until a satisfactory conductivity is achieved. Neither of these solutions are ideal, as either compromise ultimately reduces the benefits of electrokinetic devices. This chapter examines different device structures and effects of higher conductivity solutions on device performance.

4.1 Electrokinetic device experiments

4.1.1 Parallel Wire DEP devices

A series of parallel 3-wire devices were devised and constructed to understand viability of dielectrophoretic separation in high-conductance solutions, e.g. biological solutions such as blood and blood products; urine, and cerebrospinal fluid. Solid 100 μm diameter platinum wires were chosen and spaced $\sim 300 - 500$ μm on center-to-

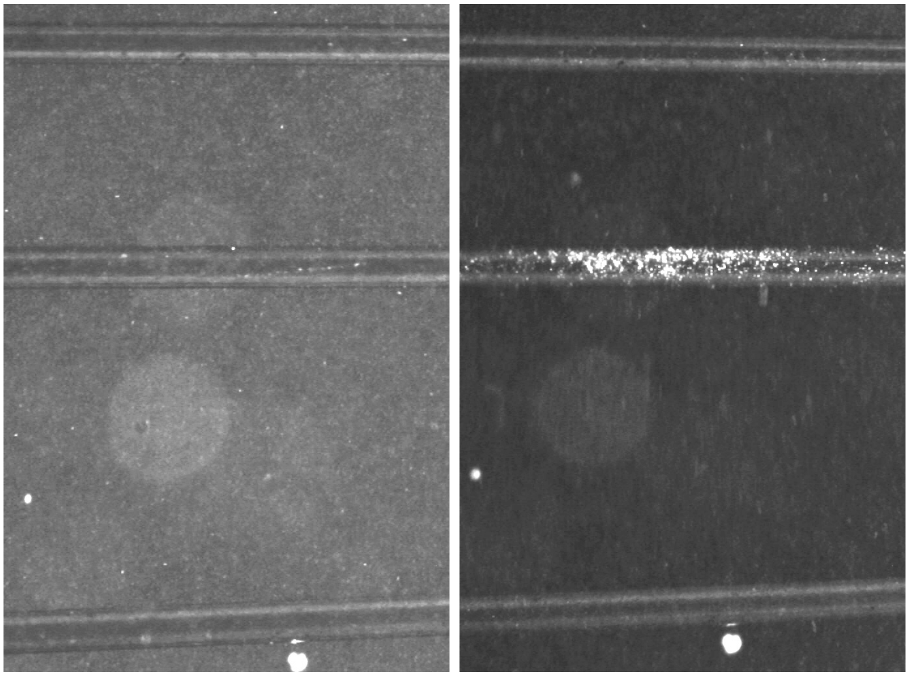

Figure 4.1: 3-wires electrode system suspended along the surface of glass substrate. Images are before (left) and after (right) 20 minutes at 28 V_{pp}, 1 kHz AC stimulus. Outer electrodes and inner electrodes are connected to opposite polarities. Solutions is 1×10^{-7} by volume of 200 nm red fluorescent polystyrene beads in 0.1x tris borate EDTA. There is an accumulation of beads on the central wire where the field gradient is highest, indicating these beads are experiencing positive-DEP.

center spacing. Solid platinum wires were chosen to minimize electrochemical attack or undercutting of more commonly chosen patterned electrodes using microelectronic fabrication methods, thus explore the limits of rapid, high-power separations.

Two configurations were chosen: first, wires were placed directly, under tension, on the surface of a glass plate. Center-to-center distance is ~ 500 μm but spacing varies due to fabrication errors. A pre-cured PDMS well was made from a 8 mm thick, 15 mm square block, through which a circular opening 5 mm in diameter was made using a biopsy punch. This well was adhered to the glass plate using a thin film of PDMS and cured overnight in a 70 °C oven. The opening was aligned over the wires, thus locking the wires in place on the edges while allowing access

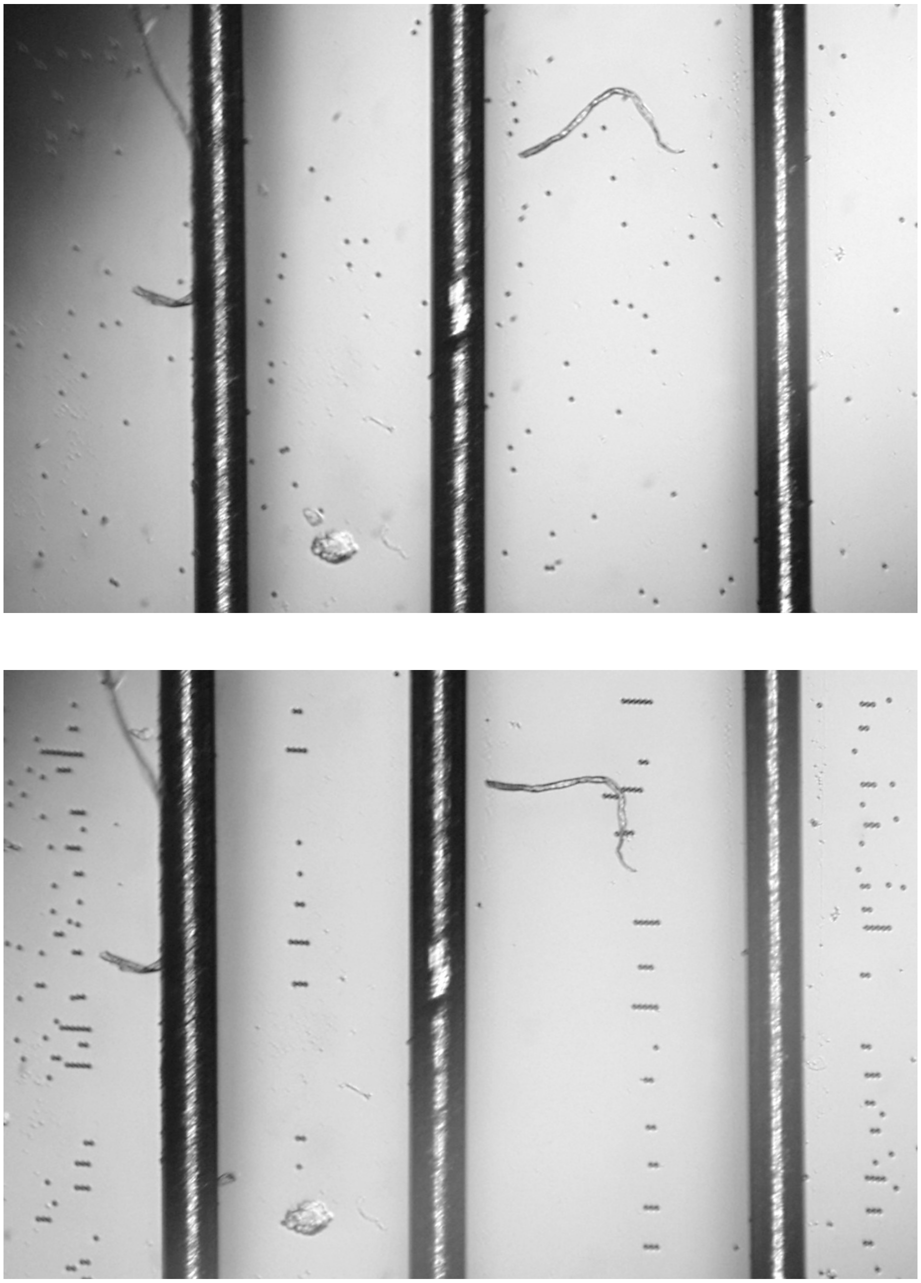

Figure 4.2: Before (left) and after (right) 18 minutes of 28 V_{pp} 10 kHz AC stimulus, where the outer electrodes are connected to the opposite polarity of the inner wire. The solution is 1×10^{-4} by volume 10 μm beads in 0.1x tris-borate EDTA with 0.2 % volume Tween20 to reduce bead aggregation. As can be seen, the beads experience negative-DEP, which pushes the particles to the local low-field regions. The string-of-pearls effect is a result of the particles aligning along the electric field.

to the wires. Due to wicking of uncured PDMS along the wires during assembly, an etch step is invoked after curing to release the wires from encapsulation. 100 μl of concentrated hydrosulfuric acid (H_2SO_4) was pipetted into the well to etch for 10 minutes before thorough rinse in deionized water and dried in a 70 °C oven. Due to the isotropic attack of H_2SO_4 on PDMS, there is slight undercutting of the opening, but the effect is small.

The second configuration suspends the 3 wires in the middle of a PTFE apparatus with a circular well $\frac{3}{8}$ inch ($\sim$ 9.5 mm) in diameter, with a depth of $\frac{3}{16}$ inches ($\sim$ 4.75 mm). Wire-to-wire spacing is affixed with cyanoacrylate (CA) glue at the ends to 0.015 inches ($\sim$ 381 μm) by drilled holes in the apparatus, but fabrication imperfections result in some wire spacing variance over the length of the well's span. Glue is cured overnight in a 70 °C oven and then these devices are cleaned by filling the well with H_2SO_4 for 10 minutes followed by a 1 $M\Omega$ deionized water rinse. Every tests is preceded by a 30 minute drying step in a 70 °C oven. Like the bottom-mounting, little attack is observed on the CA glue and none on the PTFE. Due to the wire configuration, ultrasonic agitation for cleaning causes wires to break at the adhesion junction along the edge of the well, so while all the components are thoroughly cleaned in an ultrasonic bath before assembly, only rinsing and soaking steps were used on already-assembled devices.

To begin, lower conductance solutions were first attempted. Figure 4.1 shows red fluorescence images of a parallel 3-wire device where the wires are resting on the glass surface. Solution used is 0.1x tris-borate EDTA (Fisher Scientific 1x, diluted with 1 $M\Omega$ deionized water) with 0.2 % by volume of Tween20. To this 1×10^{-4} by volume 10 μm unlabeled polystyrene beads and 1×10^{-5} by volume 200 nm red-fluorescent polystyrene beads were mixed. Before every trial, the bead-loaded solution was agitated in a vortex mixer for 30 seconds followed by an ultrasonic

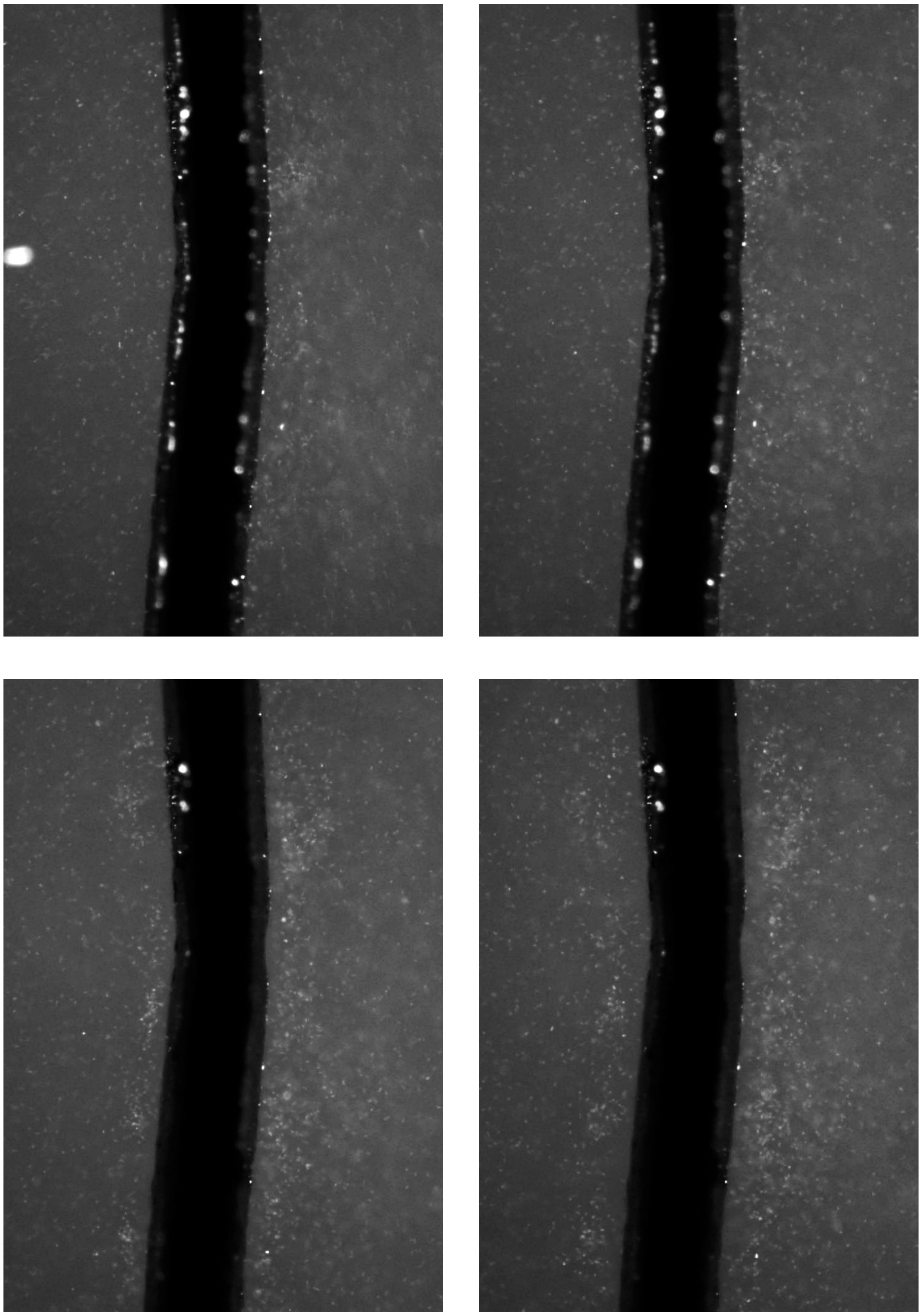

Figure 4.3: Fluorescent sequence of images at the end of 5 minute, 10 kHz, 28 V_{pp} AC stimulus (top frames). Between the top frames and the bottom frames, a 1 V DC bias was applied between the center and outer wires. Images are on 4s intervals. Solution used is 0.1x TBE with 0.2 % volume Tween20 and 1×10^{-6} by volume 200 nm red fluorescent beads. Beads, aggregated on/near the wire surface are electrophoretically driven off the surface with a large plume of fluorescence in the $\sim 10 - 50$ μm from the wire.

bath for at least 30 minutes to break up any particle aggregation and resuspend any particles that may have settled. The electrical stimulus was a 10 kHz sinusoid at 28 V_{pp}.

Figure 4.2 shows 10 μm uncoated beads in brightfield illumination before and after 18 minutes of 28 V_{pp}, 10 kHz AC stimulus. Here one can see the randomly scattered beads that have settled onto the glass surface move into strings-of-pearls centered over local low-field regions between the wires, and pushed away from the wires entirely outside the outer wires. The string-of-pearls effect is due to mutual polarization of particles causing them to align along electrical field lines. Due to the effects of dye incorporation, fluorescent beads are statically charged and conductive, thus experience positive DEP in biologically-relevant conductivities ($\sim 1S/m$). Large undecorated polystyrene beads undergo negative-DEP. as their polarizability and conductivity are below that of the aqueous solutions of interest, thus their Clausius-Mossoti factor is negative. Due to surface charge effects inverse relationship with size, small undecorated polystyrene particles may also experience positive DEP [65], [66]

Negative DEP tests were not attempted with suspended wires, since non-static particle tracking was not possible with equipment available. Thus to identify the effects of various electrical and hydrodynamic forces on particles, a particle capable of being captured local to the suspended wires is needed. Fluorescent-dyed beads, subject to positive-DEP over the range of conductivities and dielectric properties of biological solutions and appropriate respective buffers, were used. Figure 4.3 is a sequence of 4 images on a 4 second interval of the central wire in a suspended 3-wire apparatus. Preceding these frames, the 1×10^{-6} % volume 200 nm red fluorescent beads (in 0.1x TBE with 0.2 % volume Tween20 surfactant solution) were dielectrophoretically accumulated on the surface of the wire electrodes with a 28 V_{pp}, 10 kHz sinusoidal signal for 5 minutes. The first two frames show the result of this accumulation, whereupon a 1 V_{DC} potential is applied between the center and outer wires; this occurs between frame 2 and 3. Due to the static charge of the fluorescent beads, the beads experience an electrophoretic force and are driven off the surface of the central wire. This results in a plume of released fluorescent beads within $\sim 10-50$ μm of the center wire's surface for the length of the sequence of images. Due to the short depth of field and the cylindrical geometry of the wire, much of the accumulated beads on the surface of the wire are out of focus. This noted, the transition from AC dielectrophoretic accumulation and DC electrophoresis as the primary force on the fluorescent beads is clearly shown by the marked decrease in fluorescence on the wire itself, leaving only scattered light from wire as a signal.

Higher conductivity solutions were also attempted with suspended wires, where the buffer was changed from 0.1x tris-borate EDTA to 0.1x phosphate buffered saline (PBS), increasing the conductivity of the solution from $\sim 1.25 \times 10^{-3}$ S/m to ~ 0.15 S/m, or roughly an 100x increase in conductivity and approaching biological fluid conductivities. Figure 4.4 shows a large accumulation of fluorescent beads on the center wire surface after 15 minutes of stimulus at 20 V_{pp} 1 kHz. Consistent results under these conditions proved difficult, as electrothermal flow, and wire damage tend to dominate this device structure under these conditions, only becoming worse with increasing conductivity.

4.1.2 Pipette Tip-based DEP apparatus

Given the utility of dielectrophoretic separations for molecular diagnostic preparations [67], an apparatus to designed to leverage DEP into high-throughput pipetting systems was conceived. First, a microwell with a large electrode on the

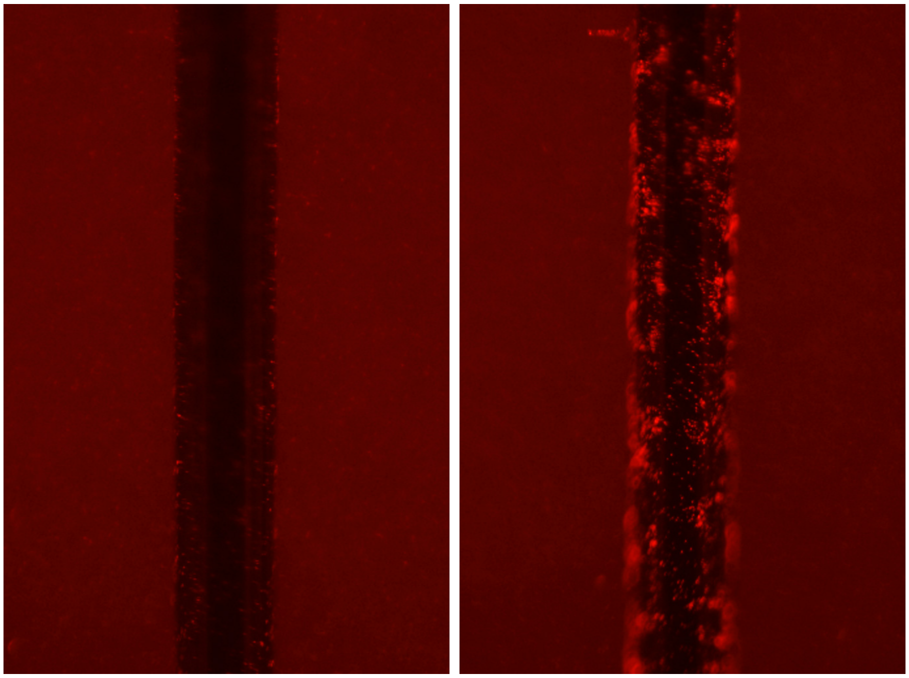

Figure 4.4: Center wire images before (left) and after (right) an applied signal (20 V_{pp}, 1 kHz for 15 minutes). Three wires are suspended through the middle of a PTFE well and the outer electrodes and inner electrode are connected to opposite polarities. Solution is 1×10^{-6} by volume of 200 nm red fluorescent polystyrene beads in 0.1x phosphate buffered saline (PBS) with 0.2 % by volume Tween20.

bottom of the well would be filled with a biological fluid containing the desired biomarkers, e.g. blood, plasma, serum, cerebrospinal fluid, urine, et cetera. Second, a pipette tip containing the necessary electrodes, buffers, and packaging would be lowered into the well. An AC signal may then be applied between the pipette's electrode and the large counter-electrode on the microwell's base, which in turn drives positive-DEP particles towards the pipette tip, and negative-DEP particles away from the tip, thus minimizing non-specific diffusion of particles into the pipette's buffer and ensuring a high-purity isolation. Lastly, after the set time, the pipette is removed from the well, whereupon further refinement and cleaning steps may me needed to prepare the sample for PCR, sequencing, or other diagnostic techniques. Critically, the pipette tip must be engineered in a manner that is effectively particle-specific: targeted particles need to be transported deep enough inside the tip that little is lost on tip-well extraction, but also no contaminant must be allowed to mix with the tip buffer as well.

To minimize fluid mixing as the tip is lowered and raised into the well; and to impart a physical barrier to large particle diffusion into the tip, a number of gel materials loaded into the tip cavity just inside the pore opening. First, gel powder was melted in a buffer (0.1x PBS, typically) and then drawn into the bottom of a pipette tip, where it was allowed to cool and set. The gel-loaded tips were then back-filled with additional buffer and immersed in a beaker also containing buffer to ensure that the gel would not dry out and buffer concentration was stable. Tips were refrigerated until use, at most a week between preparation and use. To test the tips, a series of 8 mm diameter circular wells were fabricated out of PDMS and mounted onto a glass slide upon which gold annular electrodes (3 mm inner diameter, 7 mm outer diameter) were deposited. Immediately before use, a platinum wire was inserted into the tip, to roughly 2 mm away from the pore opening, the tip was affixed to a jig that centered the tip's opening roughly 1 mm above the center of the annular electrode. The two electrodes were powered from an HP/Agilent 33120 signal generator and a Trek 2210 amplifier and observed under a Nikon Eclipse inverted microscope. Unlike Song, et al. [52], several gels commonly used for electrophoretic separations at a range of gel concentrations were tried with minimal success, as either little collection was observed or the gel melted and failed in the high conductance solution. Thus, more robust systems were attempted.

Porous PDMS-loaded Pipette Tips

Porous PDMS was fabricated by first milling granular sugar with a mortar and pestle until the nominal particle size approached 50 μm in diameter. The

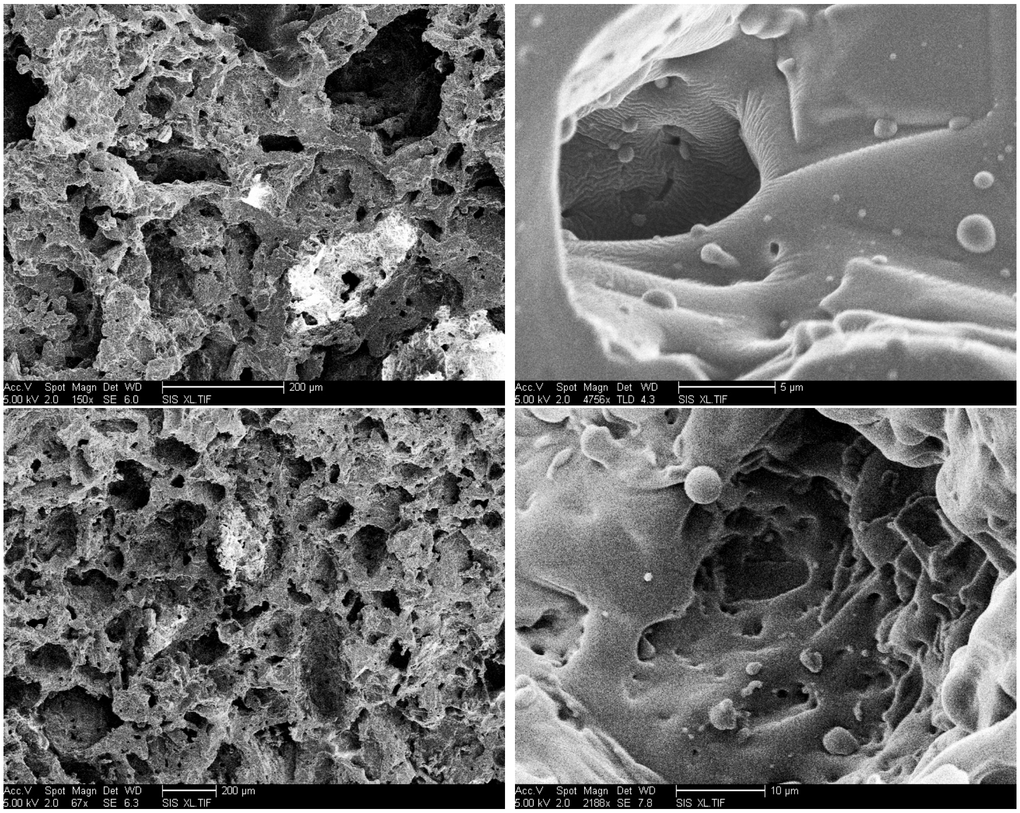

Figure 4.5: SEM cross-sectional images of porous PDMS prepared by mixing finely granulated sugar with Sylgard 184 resin and allowed to cure. The sugar was subsequently dissolved out, leaving the pores and essentially an open cell foam. As expected, a wide range of pore sizes are observed, but constrictions are as small as 10 μm across.

sugar was then subsequently mixed with Sylgard 184 resin (Dow-Corning) until the resin-sugar mixture achieved saturation at 4 g sugar to 3.1 g resin, whereupon the curing agent was incorporated at 10:1 (resin:curing agent) by mass and thoroughly mixed. A series of degassing steps, cycling from vacuum to atmospheric pressure, were then performed to remove the incorporated air. The bottom $\sim$ 2 mm of a 200 μl pipette tip (Thermo-Fisher FinnTip $^{\text{TM}}$) were then loaded with the PDMS-sugar mixture and allowed to cure overnight in a 60 °C oven. To dissolve out the sugar, the tips were submerged into a solution of 20 % by volume ethanol in 1 MΩ deionized (DI) water and agitated in a ultrasonic bath. After 30 minutes, the solution was

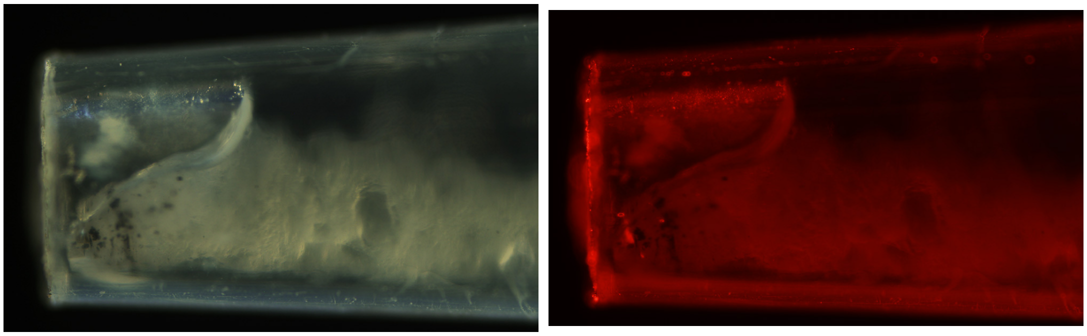

Figure 4.6: Brightfield (left) and red fluorescent (right) microscope images of a porous-PDMS tip after electrokinetic separation (100 V_{pp}, 10 kHz, 20 minutes), where 200 nm fluorescent beads were successfully pulled through the porous-PDMS matrix

exchanged and the tips were replaced in the bath for another 30 minutes. The tips were rinsed and then submerged in pure 1 MΩ DI water and sonicated for an additional 30 minutes. A final DI rinse was applied then the tips were allowed to dry out overnight in a 60 °C oven before use. Figure 4.5 shows a cross-sectional SEM of the resulting PDMS; the pore size ranges from 10 μm to 200 μm randomly. It is not known if particle size variation or clumping is the root cause of the pore size range, but the pores through the PDMS are continuous, as fluid can be pumped through the tip, albeit with significant flow resistance. Further characterization of the pore structure has not been pursued, so it is unknown whether or not any large continuous channels exist across the entire length of the porous PDMS plug or whether it is a series of large pockets interconnected with small openings.

To determine whether particles could be drawn through the porous PDMS tips electrokinetically, these tips were tried in the same a series of 8 mm diameter circular wells with gold annular electrodes on the bottom. A buffer consisting of 0.1x PBS with 0.5 % by volume of Tween20 is mixed and used to serially dilute 1 μm green/yellow and 200 nm Texas-red fluorescent polystyrene bead stocks (Thermo-Fisher) down to working concentrations; ultimately, solutions of the two

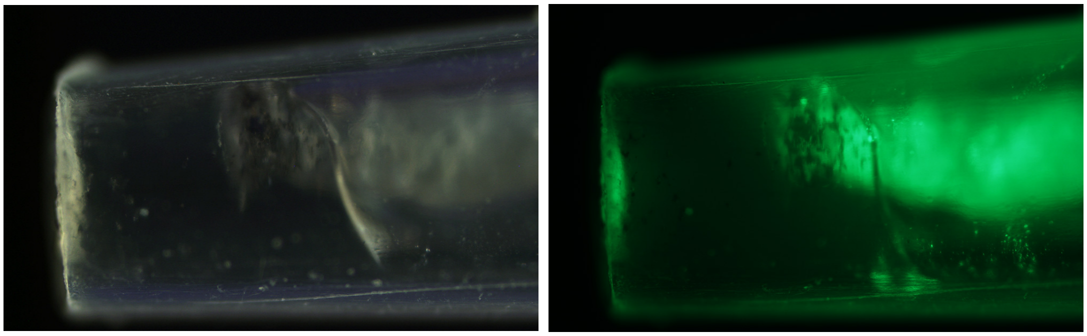

Figure 4.7: Brightfield (left) and green fluorescent (right) images of a 200 μl pipette tip loaded with porous-PDMS. Bead size is 1 μm and electrokinetic separation is the same as Fig. 4.6: 100 V_{pp} 10 kHz for 10 minutes. Like the 200 nm beads, 1 μm beads are successfully concentrated inside the porous-PDMS plug.

bead types at 1×10^{-7} by volume were tested. PDMS wells were filled with 100 μl of either the 200 nm or 1 μm bead solution and the tips were filled with 50 μl of the buffer. A 200 μm platinum wire, cleaned between tests by soaking in concentrated H_2SO_4 and rinsed in DI water, is placed in the pipette tip with the end of the wire as close to the PDMS plug without touching. The pipette was held in a 3-axis chuck and centerer over the annular electrode with a 1 mm vertical gap. The wire and the base electrode are connected to a Trek Inc. 2210 amplifier and HP/Agilent 33120 signal generator. Tests were run at 10 kHz, 100 V_{pp} for 20 minutes. After the test, the tips were removed from the well, rinsed on the outside with DI water and the platinum electrode was removed. The tips were then placed in a 60 °C oven overnight to dry before examining under a fluorescent microscope (Olympus BX51WI microscope using an Olympus DP71 camera controlled by Olympus's DP Manager software). The microscope filters used were 505/515 nm excitation/emission and 580/615 nm excitation/emission for the green/yellow and red dyes, respectively.

Runs at 100 V_{pp} using purely 200 nm red fluorescent beads (Fig. 4.6) and 1 μm green fluorescent beads (Fig. 4.7) show effective capture in porous-PDMS tips.

There is no fluorescence observed in the rest of the tip, solely in the porous-PDMS region; additional illumination comes from internally scattered light in the tip itself. A solution having both the 200 nm and 1 μm beads, at 1×10^{-7} by volume, respectively, in 0.1x PBS with 0.2 % Tween20 was tested to see if there were major changes in the distribution of beads based on size. The electrodes were driven with 150 V_{pp} at 10 kHz for 20 minutes while a second, parallel test was run without any electrical stimulus for 50 minutes to determine if diffusion effects or electrokinetic effects were dominant and the effect of bead size on transport. Figure 4.8 shows the electrokinetically-driven chip after drying. The beads have both been transported throughout the porous PDMS; while the 200 nm Texas red beads appear brighter it is unknown what the relative ratio is between the two bead sizes due to differences in the dye sensitivity and lamp intensity at the respective wavelengths. The differences between the actively driven tips and the those dependent solely on diffuse are striking. First, while the images of the driven tip system of Fig. 4.8 are at 5x magnification and show the entirety of the plug, the lower images are at 10x magnification and are zoomed in at the outermost extents of the PDMS plug. The smaller red-fluorescent beads, as expected, diffuse slightly inside porous PDMS, the larger green fluorescent beats are essentially confined to the outer surface of the tip. It must also be noted that the beads were allowed to passively diffuses for 2.5 times as long as the actively-driven tip was immersed in the bead-loaded solution as to amplify any diffusion effect.

The implications of this test indicates that applying a dielectrophoretic force through a porous media serves as an effective filter to selecting positive-DEP particulate, even when the identically-sized particle are unable to diffuse through the media passively. This adds an additional layer of size selection and obviates concerns about capturing desired particulate within a tip. Release becomes more

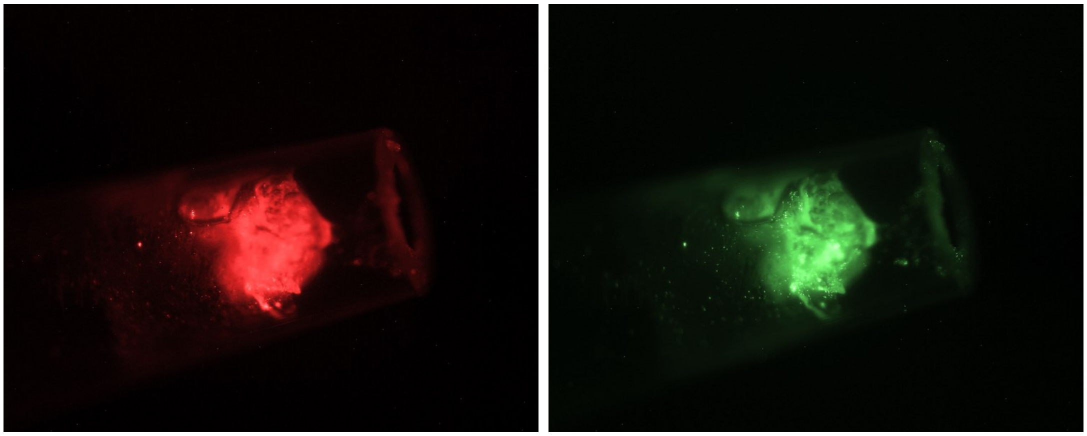

Driven electrode tip (150 V_{pp}, 10 kHz, 20 minutes), 5x magnification.

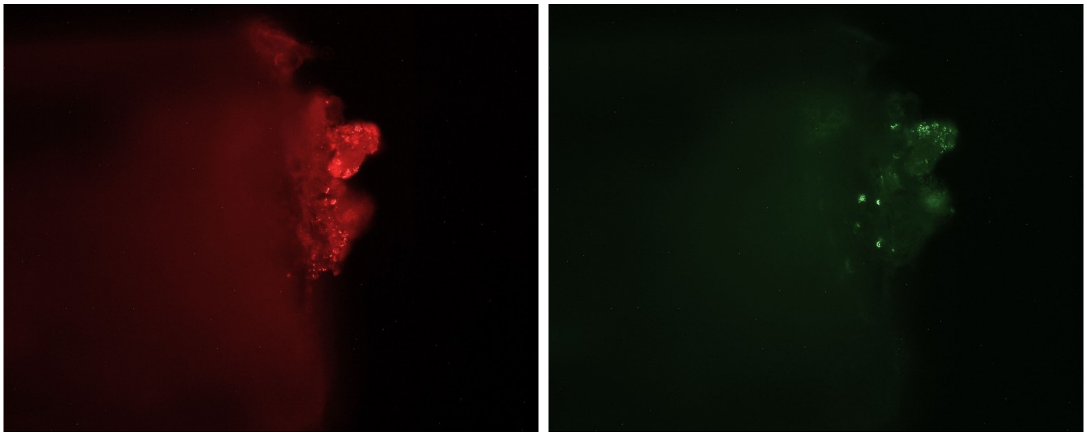

Passive diffusion tip (50 minutes), 10x magnification.

Figure 4.8: Fluorescent images of a porous PDMS plug in 200 μl pipette tips. The tip was immersed into a solution of 0.1x PBS with 0.5 % by volume of Tween20 detergent and 1×10^{-7} by volume of both 200 nm red fluorescent beads and 1 μm green/yellow beads. A 150 V_{pp} 10 kHz signal is driven between a 200 μm platinum wire and a gold annular electrode for 20 minutes to electrokinetically drive the beads through the PDMS (top). A second, simultaneous test was conducted for 50 minutes, where the tips were allowed to passively diffuse into the plug. The DEP-driven plugs contain fluorescent beads throughout, whereas the passive plugs have the slightest of diffusion at the very end.

complex, as the desired particulate is captured within an open cell foam. It is important to remember, however, that this electrokinetic separation step is an intermediate step along the pathway to downstream diagnostics. By transferring the tip to a different well, containing an intermediate buffer, or one appropriate for down-stream processing, such as PCR reaction buffer, DC electrophoresis and attendant DC electroosmosis through the porous media allow for particle release. Furthermore, while the system demonstrated uses porous PDMS-loaded pipette tips, it serves more importantly as a proof of the concept than an ultimate realized solution. Different open-cell foam materials to realize the tip should be explored for manufacturability, biocompatibility, and optimal pore sizing.

It is also infinitely more robust system than any gel-based application, needing essentially no treatment immediately before use, nor a limited shelf life once prepared, like any kind of gel-based system. There is also zero concern about failure of the porous matrix during use. While PDMS has been proven well-compatible with biological solutions and regularly been used to create microfluidic lab-on-a-chip systems, a hydrophilic surface would mitigate nonspecific adhesion of many biological fragments and cells. PDMS is not the only material that could be used for this specific application, although other structural polymers would also be hydrophobic, and thus require some form of hydrophilic coating. There is still a large amount of work on this design to bring it to maturation.

4.2 Electrokinetic device simulations

A series of simulations were designed in COMSOL Multiphysics (v5.2, Los Angeles, CA) to correlate with tests conducted. Three geometries, in specific, were tested, and subsequently compared with constructed devices: a parallel set of three wires, a wire and annular electrode, and a planar grid array.

The parallel wire simulation has 3 wires of 100 μm diameter spaced on 400 μm centers, which are suspended in the center of a 900 μm by 900 μm fluid volume. The fluid is modeled as a solution of sodium chloride in water at 147 mmol/l concentration, similar to that of 1x phosphate buffered saline (PBS), which is a commonly used biologically-compatible buffer. Diffusivity of both sodium and chlorine were assumed to be $1.48 \times 10^{-5} cm^2/s$ [68]; bulk solution conductivity is assumed to be 1.4 S/m, and relative permittivity of the solution is assumed at 80, corresponding to the simulated temperature of 20 °C [69]. Considering the salinity of solution, it is expected that the real dielectric constant should be slightly less than 80. Dynamic viscosity, heat capacity, density, and thermal conductivity are used as-is from the COMSOL material library for pure water.

The diameter of the planar electrodes is 60 μm and they are placed on a 150 μm spacing. Alternating polarities are configured on a checkerboard arrangement. The surface is covered with a 200 nm layer of SiO_2, with 60 μm diameter windows centered over the electrodes to establish the active area.

The fluid is modeled as 0.1x PBS. Conductivity of the solution is affixed to 0.14 S/m, since sodium and chlorine, the primary constituents are strongly dissociated at these concentrations no scaling was applied. The dielectric constant versus temperature follows the low frequency formula provided by Kaatze [70]:

$$\epsilon(0) = 10^{1.94404 - 1.991 \times 10^{-3} K^{-1} (T - 273.15K)} \text{ for } 0\ ^\circ C < T < 100\ ^\circ C$$

The incorporation of 13.7 mmol/L sodium chloride, and, to a lesser degree, 1 mmol/L Na_2HPO_4, 0.27 mmol/L, and 0.18 mmol/L KH_2PO_4 will slightly lower the static dielectric constant of the solution from that of water, but the effect is small at this 1000 ppm salinity and was thus ignored [71]. Conductivity was modeled to vary 2 %/K, centered at 25 °C.

The electrochemical interface between the solution and the wire is not modeled, which will result in a number of potential effects. While bulk concentration will remain relatively constant, especially under high conductivity conditions, the electrical properties of the electrolyte within the first 10 to 100 nm of the electrolyte-electrode interface will be drastically different than in the bulk. First, voltage drop across the Stern layer is significant, even with a high conductance electrolyte. Second, the local environment of the interface will look dramatically different to the bulk: gas evolution from electrolysis, reactions between dissolved species, e.g. chlorine, and the electrode with affect the chemical landscape in the region. The dielectric properties of the solution will change dramatically throughout the double layer as result of ion concentration effects [72]. Lastly, if dielectrophoretic particle accumulation is substantial, then the interface itself will strongly affected by the presence of the particulate.

As result of the double layer being inadequately described, the simulations herein will need to be interpreted more qualitatively and relative to one another, rather than numerically. The value, however of understanding the geometrical effects different designs, when tested like-for-like, gives good insight into compromises between electrokinetic forces, thermal considerations and resultant flow dynamics.

4.2.1 Planar array DEP Simulations

Figure 4.9 shows a 2-D cross-sectional schematic of a planar electrode array. Deposited on silicon, 80 μm diameter platinum pads are placed on 150 μm center-to-center spacing. A 200 nm-thick conformal layer of SiO_2 covers the surface, and 60 μm circular windows are centered over the platinum pads. A 300 μm well, filled with 0.1x PBS, is capped with a 200 μm polypropylene cover. The model is equivalent to a unit cell of the array, where 2 half-electrodes flank a single electrode and periodic boundaries are used (i.e., modeled as infinite array of repetitions). Simulated voltage is 10 V_{pp} between the alternating electrodes. The potential plot is shown in the upper-left plot of Fig. 4.10; potential falls off to a mean value $\sim$ 100

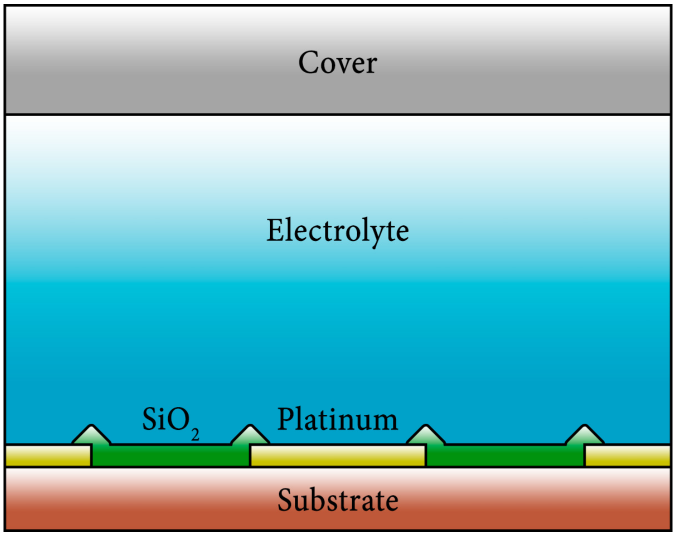

Figure 4.9: Schematic diagram of the 2-D cross-section simulation model (not to scale). Simulation design assumes infinite repetitions of this cell in both lateral directions, so only half of the two outer platinum electrodes are modeled per cell. A SiO_2 layer covers the exposed silicon substrate and the platinum electrodes. A window is then etched in the SiO_2 to define the active electrode area. The electrolyte is constrained between the electrode array on the bottom and a cover on the top.

μm above the electrode surface. The magnitude electric field gradient term of the dielectrophoretic force equation $(\nabla(E^2))$ is shown in the upper right. This plot is zoomed in on the central electrode as to show detail. Given the symmetry of the system, the outer electrodes have the same behavior. There is a large electric field gradient at the electrode-insulator edge that extends 10 μm into the solution. There is a low-field null in the center of the electrode, but only on the electrode surface, as the force vectors all point towards the SiO_2-Pt edge, canceling at their midpoint. Similarly, a low-field null occurs between electrodes. 3-D electric field simulations, seen in Fig. 4.11 show the low-field is most dominant in the center point of any 4 adjacent electrodes. Particles experiencing positive-DEP will migrate to the very edges of the electrodes. Negative-DEP particles will accumulate in the large nulls between electrodes, unless these particles have already settled onto the electrode surface before an electric field is established, whereupon they will move to the low-field null in the center of the electrode.

2-D thermal and velocity plots are showing on the bottom-left and bottom-right of Fig. 4.10. Caution should be taken in interpreting these plots, as their magnitudes are negligible: the total temperature gradient over the fluid volume is 0.2 °C, and time-averaged flow velocities are ≤ 10 nm/s. Under the parameters being used, namely the electrode conductivity and applied voltage, electrothermal effects are essentially zero; the device is dominated by dielectrophoretic forces and Brownian motion. At low frequencies, temporal heating effects on the crests may become more significant, even if time-averaged heating is low. The pad size and spacing are both much larger than needed, as the effective particle capture zone exists on the electrode circumference and much of the device's surface is underutilized.

Simulations follow behavior seen in devices, e.g. [35], [73], where thermal effects are minimal and positive-DEP particles accumulate on the electrode circumference. Figure 4.12 shows red-fluorescent beads selectively accumulating on the outer circumference of the electrodes, as expected by its geometry.

4.2.2 Wire-based DEP Simulations

Figure 4.13 shows plots the electric field and $log_{10}(\nabla|E^2|)$ of systems where the wires are suspended in the middle of the well (left) and in contact with the floor of the well (right).

Dielectrophoretic forces are highly localized around the wires, as the field gradient further away from the wires drops precipitously. This is doubly caused: first, the electric field is contained largely to the region between the wires, and, secondly, the field is relatively constant between the wires. Curiously, in the middle well case, the electric field around the center wire is nearly radially symmetric

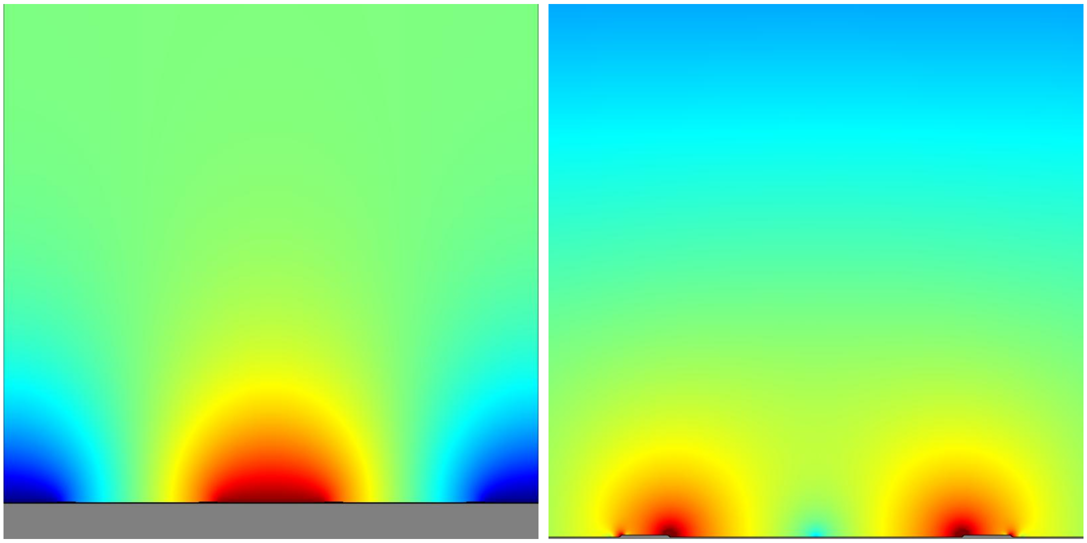

Voltage (left); $log_{10}\left(\nabla\left|E^2\right|\right)$ (central electrode zoom)

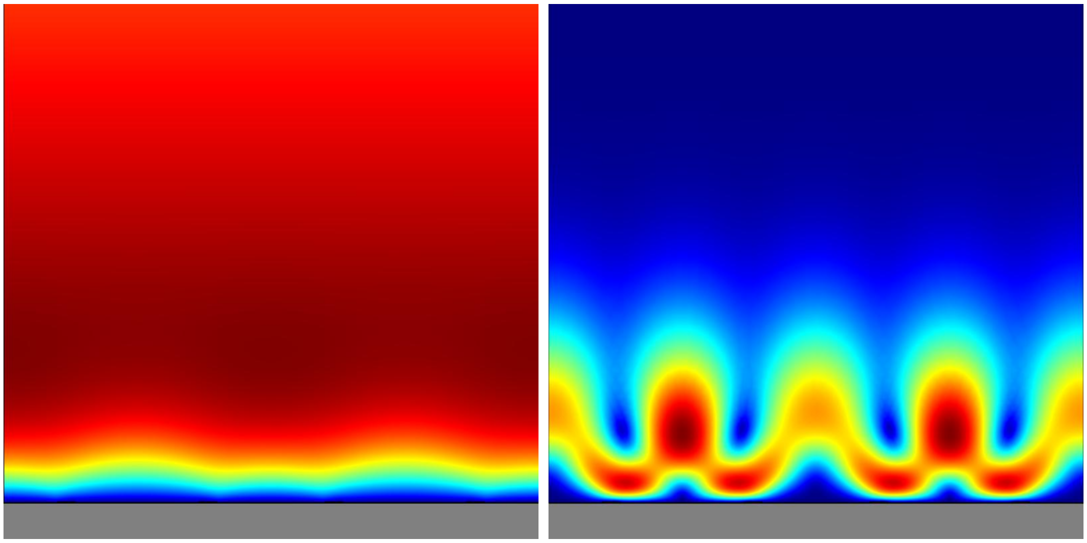

Temperature (left); flow velocity (right)

Figure 4.10: 2-D cross-sectional simulation of a planar electrode array. Potential falls off to neutral $\sim 100\ \mu$m from the electrode surface. The $log_{10}\left(\nabla\left|E^2\right|\right)$ plot in the upper right is zoomed in on the central electrode. The field gradient is greatest right at the outer circumference of the electrode, as it intersects the SiO_2 layer. There is a second high field region in the silicon, but this gradient is irrelevant. Low-field field gradients exists in the center of the electrodes and at the mid-point between the opposite polarity electrodes. Thermal (lower left) and flow velocity (lower right) plots are deceptive, however, as the temperature gradient across the fluid region is only 0.2 °C and time-averaged velocities are ≤ 10 nm/s. In essence, this geometry, while having small effective capture area, is largely dominated by dielectrophoretic forces.

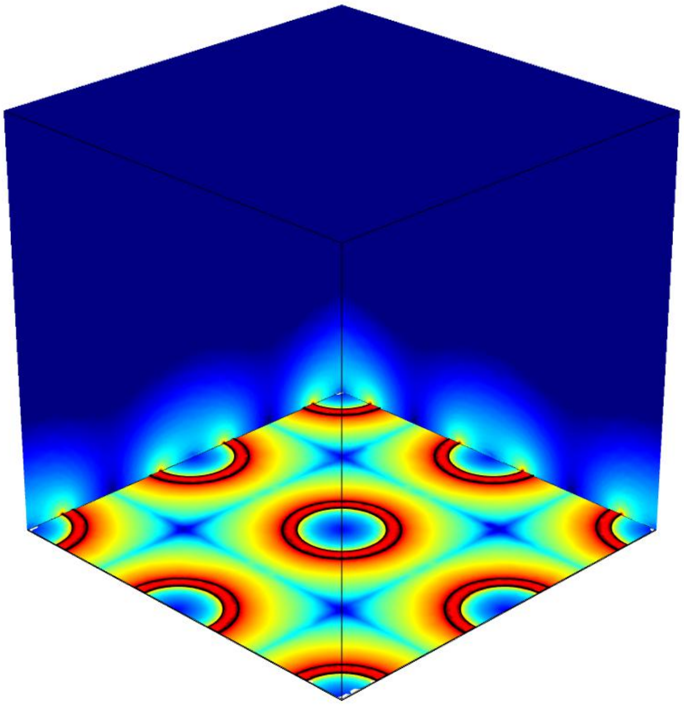

Figure 4.11: 3-D simulation of planar electrode showing the magnitude of the electric field gradient ($log_{10}\left(\nabla\left|E^2\right|\right)$) along the bottom surface and through the electrolyte solution intersecting the middle of a line of electrodes along the XZ and YZ planes. Low-field gradient regions exist between the electrode, especially at the midpoint of any 4 adjacent electrodes. Likewise, the middle of every electrode has a low-field null. High field gradients exists at the outer circumference of the electrode, as it intersects with the oxide coating. High-field gradients fall off very quickly, so the bulk solution is $\leq 10^{-6}$x the magnitude of the gradients near the electrodes.

even though the wires are in the same plane. Understandably, the distal side of the outer wires has very little electric field gradient.There is a dielectrophoretic low-field region between the wires, where the high-field regions existing on/near the wires, and thus pulling in opposite directions, respectively cancel each other out. The bottom-mounted device model shares many similarities, with obvious asymmetries due to the existence of the glass plate directly beneath the wires. Since the glass plate is an insulator, the electric field is bent away from the glass. The resulting electric field gradient minimums occur on the glass-electrolyte interface

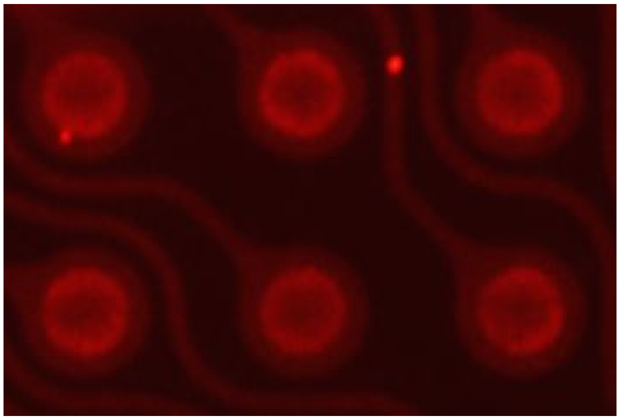

Figure 4.12: Accumulation of 200 nm red-fluorescent beads on the outer circumference of planar electrodes.

rather than on the plane connecting the three wires' respective centerlines. In context of capturing particles via positive-DEP forces, the effective cross section is small. Outside of the fluid volume within 10-100 μm of the wire, other forces, such as drag, gravitational, or diffusive, will likely dominate DEP. This situation is doubly true as particles become smaller, as explained in 2.1, drag forces are proportional to r^2 whereas DEP is proportional to r^3; all else equal, large particles are less affected by fluid flow and, thus, the effective DEP force is proportionally greater than in small particles.

Thermal and flow velocity plots for the respective middle-mounted and bottom-mounted electrode systems are showing in Fig. 4.14. Joule heating is centered around the wires, and a plume of higher temperature fluid rises from this heat source. While there is some amount of heat transfer due to conduction, the heated electrolyte is lower density to the fluid around it, and thus rises due to buoyancy forces. This establishes a circulating fluid flow where cooler electrolyte flows down the sides of the well before is fed up through the gaps between the wires and then accelerated upwards again by Joule heating. The proximity of the glass plate to the bottom-mounted wires prevents flow from circulating through the

Middle-mounted structure (left); bottom-mounted structure (right).

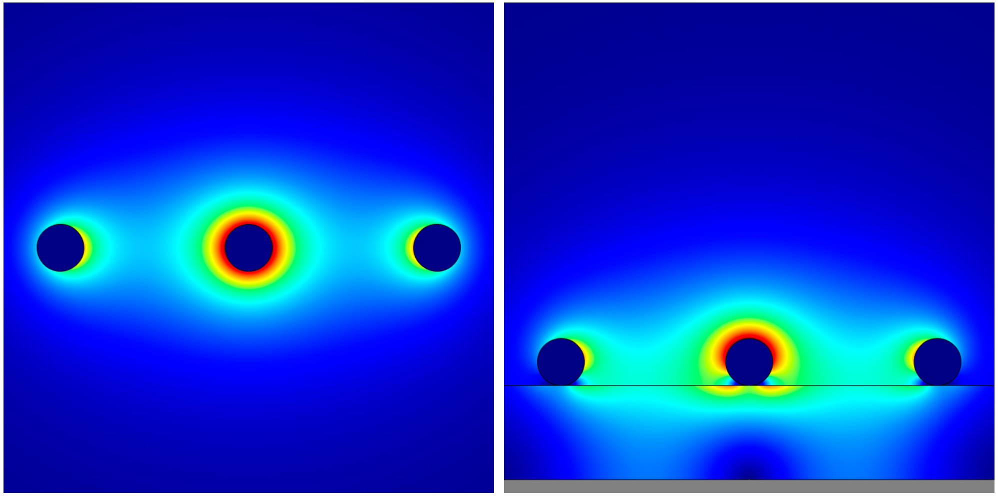

Electric field simulation.

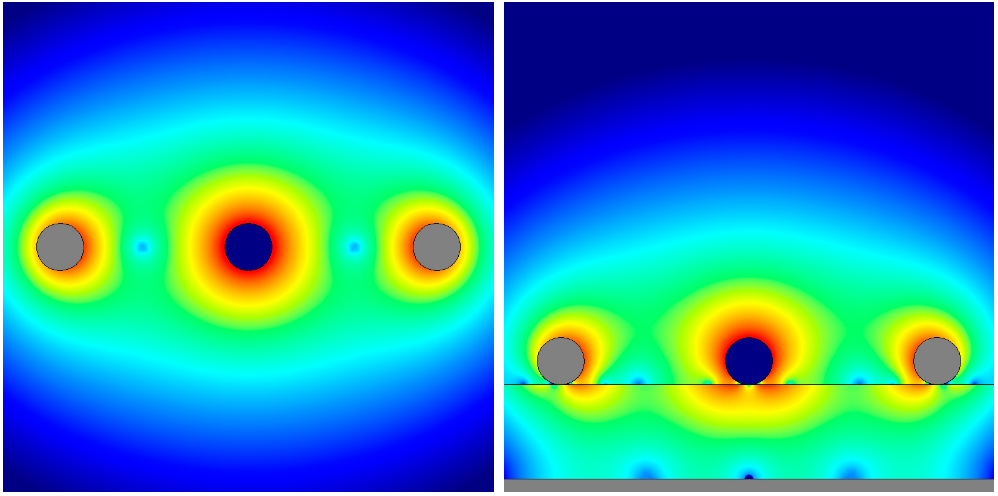

$log_{10}\left(\nabla\left|E^2\right|\right)$ term, range 10^{10} to $10^{14.5}$.

Figure 4.13: Simulations of a 3-wire electrode array (100 μm diameter Pt wires on 400 μm spacing) immersed in a 1.4 S/m aqueous electrolyte solution, and a 10 V_{pp} differential voltage applied between the inner and outer wires. As expected, the electric field, and thus the electric field contribution to the DEP force equation (i.e., $\nabla\left|E^2\right|$) are symmetric around the center electrode when the wires are suspended in the middle of the fluid. When resting on a glass surface, the electric field is bent upwards away from the glass. In both cases, there is a low-point in the field gradient directly between the wire electrodes, seen as small blue dots in the lower figures. Particles that experience negative DEP will move to these nodes, whereas positive DEP particles will move towards the wires. Note the bottom plots are logarithmic in intensity; the fall off in the DEP force as one moves away from the wires is very rapid, the $\nabla\left|E^2\right|$ term falls off to 10^{-6} times its peak 200 μm away from the wires.

wires, thus the cooler fluid flows laterally across the glass plate and then over the wires before accelerating upwards. At equal voltage, the bottom mounted system runs cooler; the reason for this is twofold. First, the close proximity of the resistive glass plate rather than the conductive electrolyte means the effective wire-to-wire impedance is greater, and, thus Joule heating is reduced. Second, the conductive heat transfer between the wire electrodes and the bottom plate means that a good amount of the heat is lost to the environment via the glass plate. The smaller density gradient means the circulating flow velocity is likewise lower.

Beyond purely velocity differences, which are greatest in the central plume and along the top surface, the flow immediately local to the wires is critically different. When the wires are suspended in the middle of the electrolyte, flow circulates from underneath and through the wires. Fluid around the bottom-mounted wires is relatively stagnant, as the circulating flow must go over the wires before accelerating upwards from heating effects. From the perspective of forces on particles local to the wires, this changes the situation entirely. Large shear forces from fluid flow through the electrokinetically active region between the wires may push particles out of the region before weak, positive-DEP forces can attract these particle into the boundary layer, where DEP forces are also orders of magnitude greater. On the other hand, the circulating flow will bring greater amounts of particulate into closer proximity of the electrokinetically-active region. In highly conductive solutions, the thermal effects and concomitant fluid flow are sufficiently high to inhibit positive-DEP forces from effectively capturing particles on the wires.

Bottom-mounted electrodes gain help from gravitational forces, but the circulating flow also brings new material in closer proximity to the wires. With no fluid flow between the wires and minimal lateral buoyancy forces affecting any particles that enter the electrokinetically-active region, positive-DEP forces will

Middle mounted device (left); bottom-mounted device (right).

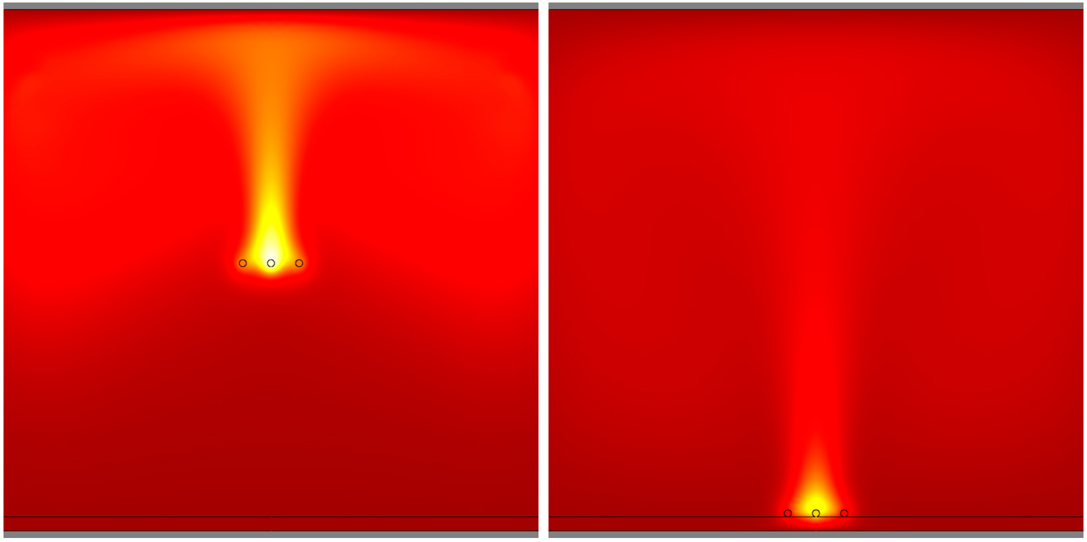

Thermal simulation; range 20 °C to 49 °C.

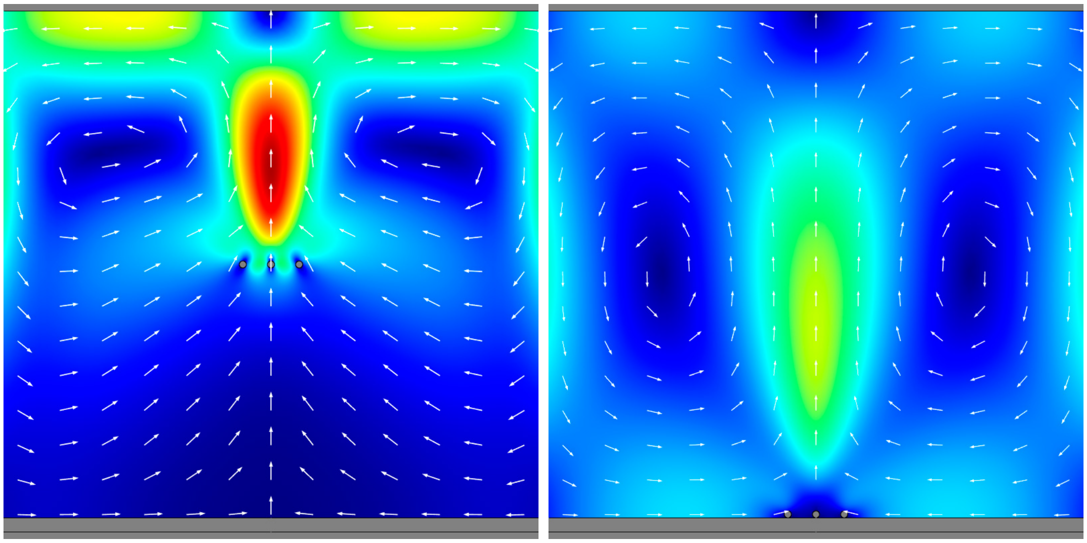

Flow velocity term, range 0 mm/s to 5.5 mm/s.

Figure 4.14: Simulations of a 3-wire electrode array from Fig. 4.13, showing the temperature and flow velocity. The greatest Joule heating occurs between the outer and inner electrodes, lowering the local density of the fluid in this region. As result of density differences, buoyancy forces cause an plume of upward fluid flow balanced by circulating flow that brings cooler, higher density solution down. The middle-mounted wires experience greater heating since electrolyte, and thus current, surrounds the wires in all directions. There is also, due to proximity to the surface where the majority of heat is lost to the environment, a greater thermal gradient in the middle-mounted design. As consequence, the flow velocity in the central plume is $\sim 2-3$ greater for the middle-mounted wires than the bottom-mounted.

dominate, and affected particles will concentrate on the wire surfaces.

4.2.3 Tips-based COMSOL simulations

To correlate with the physical observations, a series of COMSOL simulations on the tips system were conducted. To model a 200 μl pipette tip, the model uses a polypropylene tip with a 360 μm opening and an 8 °taper. Recessed 1000 μm from the tip opening, a 100 μm diameter platinum wire is suspended in the center of the pipette tip. The wire is rounded into a hemisphere, i.e. a radius of 50 μm at its end. The tip is centered 1000 μm above the floor of a 10 mm diameter circular well. An annular counter-electrode is placed on the floor of the well; its inner diameter is 3 mm an outer diameter is 7 mm. The dimensions of the well and counter electrode had minimal effect on simulation results as the primary effects are confined to the tip opening, as long as the overall well and counter electrode dimensions are much larger than the tip. Initial temperature and all outer boundaries of the well were affixed to 20 °C. Electrical stimulus between the two electrodes was simulated as 100 V_{pp} or 35.36 V_{rms}, as frequency-based effects were not modeled. The electrolyte solution throughout the well and pipette tip was approximately 0.1x PBS, as described previously. The bottom millimeter of the pipette tip was filled with a 2 % agarose gel, but this is not modeled. The effect of a 2 % agarose gel on conductivity is small [74], although it would affect convective heat transfer and flow.

An identical set of tips were simulated with the inside of the pipette tip coated with platinum; the coating covers the inside except the final 20 μm from the tip's opening. This metal layer is left at a floating potential, i.e. unconnected to any external input or ground. Figure 4.15 shows the resulting potential distribution and $log_{10}\left(\nabla|E^2|\right)$ plot for the standard-tip (left) and coated-tip (right). The region is zoomed in solely on the tip rather than the bulk since the electric field is focused primarily in this region rather than the bulk. Looking first at Fig. 4.15a, the voltage gradient starts at the tip opening and ends at the wire end. The gradient is relatively smooth throughout this region. Figure 4.15c shows the corresponding $\nabla|E^2|$, in log scale to capture the overall range, where the blue is lowest and red is highest. The electrical field gradient is, as expected, greatest right at the wire and the constriction in conduction pathway due to the pore, especially at the inner tip edge. There are two low-field nodes along the centerline between the tip opening and the wire, while a moderate high-field region is continuous throughout the tip, pointing towards the wire end.

The coated-tip is shown in Fig. 4.15b and Fig. 4.15d. Clear differences are notable: namely, the metalized layer becomes the lowest resistance pathway, rather than flowing directly to the tip of the electrode. The potential inside the entire tip remains nearly constant as current from the metal coating to the driven wire electrode is distributed throughout the extent of the tip, and the potential drop is centered on the bottommost edge of the metalization. As result of the constriction, the electric field gradient is much greater in this specific region, greatly augmenting the electric field-derived component of the dielectrophoretic force equation ($\nabla|E^2|$). There is, however, a large low-field node established in between the wire tip and the end of the metal sleeve, resulting in a dead-zone in the tip. Given the intended usage, this suggests that all captured particulate will accumulate at the metalization edge rather than progress up into the tip.

Figure 4.16 shows the respective thermal and flow velocity plots. Current density is greatest in the high electric field region, and the resulting Joule heating will cause density gradients in the fluid. Due this specific geometry, the majority of the fluid inside the tip is effectively fixed, limiting heat transfer to primarily

Standard-tip left, coated-tip right.

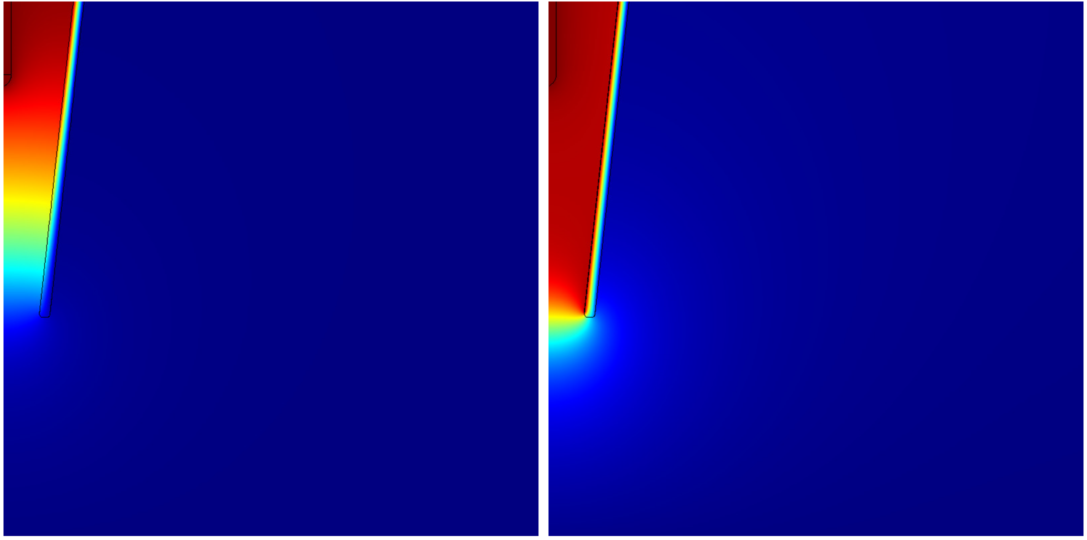

(a) (b)

Voltage simulation; range 0 to 100 V_{pp}

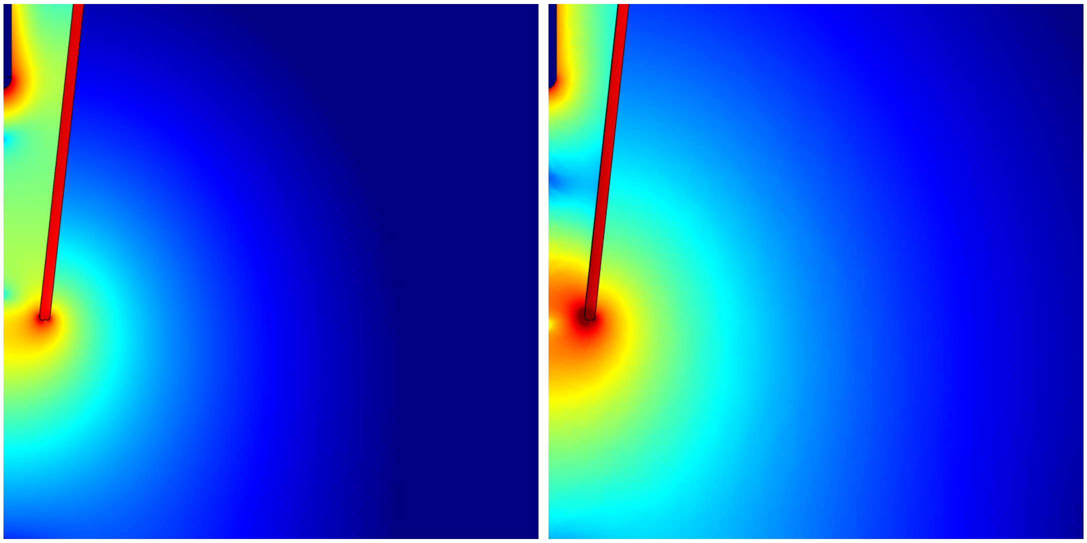

(c) (d)

$log_{10}\left(\nabla\left|E^2\right|\right)$ term, range 10^{10} to $10^{19.5}$

Figure 4.15: Simulations of the electric field of a tip-based electrokinetic system (right) and a metal coated tip (left). The electric field is constricted by the pore opening, and, thus results in large field gradients, which are needed for dielectrophoretic separations. The coated tip greatly increases the electric field gradient since it becomes the lowest impedance path.

Standard-tip left, coated-tip right.

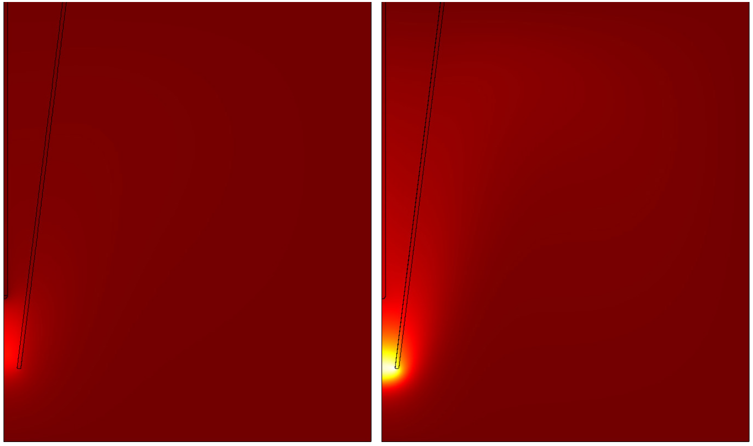

(a) (b)

Thermal simulation; range 20 °C to 72 °C

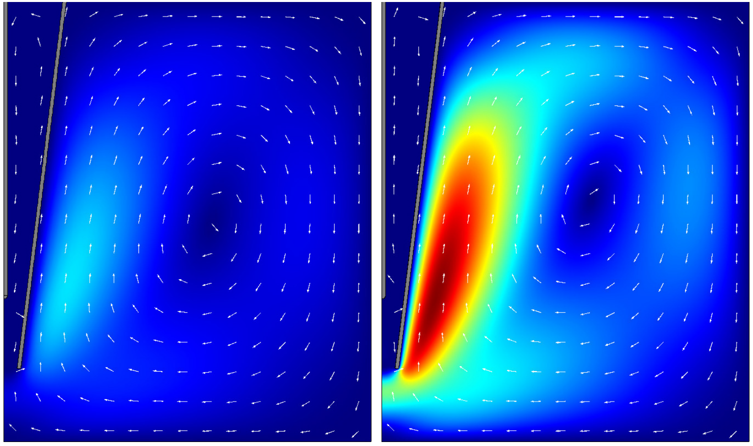

(c) (d)

Flow velocity term; range from 0 to 1,600 μm/s

Figure 4.16: Thermal and fluid velocity plots from simulations of a wire electrode in a pipette tip versus a metal-coated pipette tip. Joule heating results in localized heating of the electrolyte, affecting the density of the fluid in the heated region. The density gradient drives fluid flow, resulting in the circular path, while flow is relatively restricted inside the tip. The higher current density of the metalized tip yields greater temperature gradients, and its placement closer to the tip opening augments fluid flow.

conductive rather than convective. This also means the absence of the hydrogel is relatively small. Similarly, the tip itself acts as an insulator, further localizing the heat. Thermal gradient-driven flow occurs only outside wall of the tip; the circular flow pulls the low density fluid away from the tip opening, returning cooler fluid. A

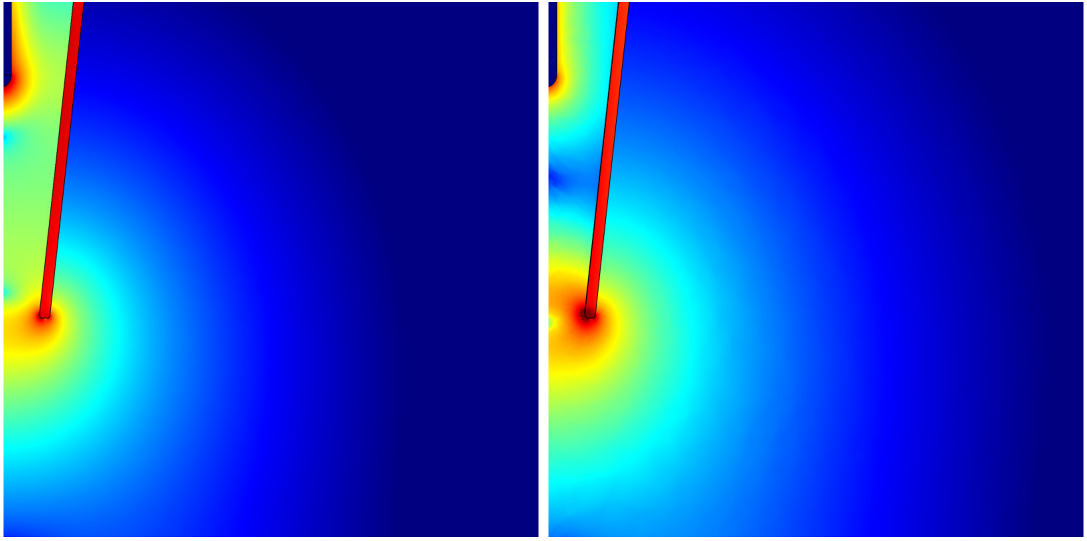

Standard-tip 100 V_{pp} left, coated-tip at 50 V_{pp} right

$log_{10}\left(\nabla\left|E^2\right|\right)$ term, range 10^{10} to $10^{19.5}$

Figure 4.17: Comparison plot of electric field gradients in for a standard-tip at 100 V_{pp} and a coated-tip at 50 V_{pp}. The electric field gradients, while obviously scaled proportionally to the magnitude of the stimulus, are governed much more directly by geometrical and design constraint. The overall electrode-to-electrode impedance in the coated-tip is roughly a quarter that of a standard-tip as the potential drop is concentrated over a much smaller region.

side benefit of the flow is that large particles, such as cells, are less likely to adhere to the outer wall of the tip. A shear force along the wall encourages particles to stay in suspension rather than diffuse throughout the fluid and interact with the pipette tip surfaces.

As result of the metalization, the current density, especially local to the edge of the coating is much greater. Joule heating in this local region drives the local temperature upward as seen in Fig. 4.16a versus 4.16b, pushing peak temperatures up to 72 °C versus 36 °C with the standard tip. As anticipated, flow velocity is also much greater, where simulated peak velocities in the metalized tip are roughly 3 times those of the standard tip. It should be stated that the simulation is some ways unrealistic: with these current densities and temperatures, the metalization layer would fail and any biological material degraded. These like-for-like parameters are

Standard-tip 100 V_{pp} left, coated-tip at 50 V_{pp} right

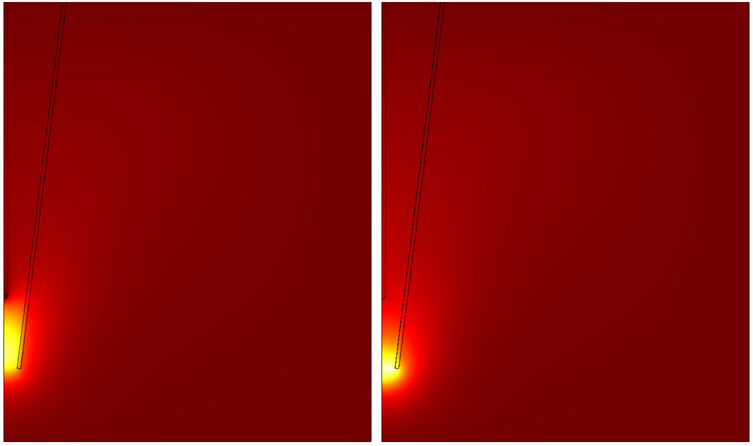

Thermal simulation, range 20 °C to 36 °C

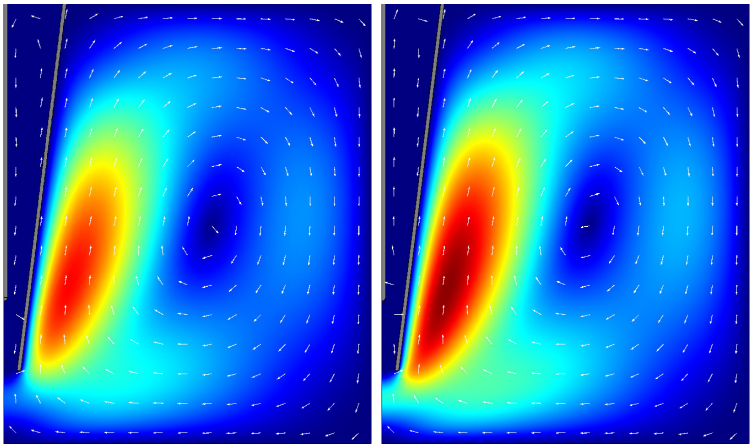

Flow velocity term, range 0 μm/s to 640 μm/s

Figure 4.18: Thermal profile and fluid velocity of a standard tip at 100 V_{pp} and a coated-tip at 50 V_{pp}. Due to the difference in electrolyte impedance, the lower voltage brings the coated-tip into near-equivalence in terms of heat output, which results in similar flow patterns and velocities.

indicative as to the dramatic effects of manipulating the electric fields incorporation of conductive elements, but reducing the voltage in half, to 50 V_{pp}, brings the temperature to a much more reasonable range.

Figure 4.18 shows the results of lowering the voltage in the modified tip to 50 V_{pp}, as compared against the standard tip geometry at 100 V_{pp}. Effectively, the coated tip system, as modeled with 0.1x PBS, exhibits $\sim \frac{1}{4}$ the impedance of the standard tip arrangement, so halving the voltage brings the temperatures into near equivalence. Consequently, fluid movement in the system becomes more closely related; the hottest, and thus lowest density fluid is centered lower in the tip, so a greater portion of it exists outside the trapped confines of the tip and resulting a slightly higher velocity fluid profile. Most importantly, scaling the voltage emphasized the importance of geometry to constrain the electric fields to favorable regions rather than by simply applying a larger voltage. Reducing voltage by a factor of two affects the $\nabla|E^2|$ by orders of magnitude less than the effect of pinching the entire electric field to a geometrically small region.

When looking at using a pipette tip-based system, several important take-away messages are manifest. There is minimal flow in the electrically-active region, reducing the possibility of drag overcoming dielectrophoretic forces, but also reducing the amount of new material delivered to the region and hampering the effective capture volume of the dielectrophoretic separation. Ideally one wishes to have slow, but continuous flow through most dielectrophoretically active region as to constantly transport new material to the collection site. The flow must be slow enough that the resulting drag force on the particulate is significantly less than electrokinetic forces. New tip geometries would need to be explored to maximize the efficacy of particulate capture. Likewise, a system designed around much smaller geometries, e.g. 384 well parts and tips with openings only tens of microns across will inherently have higher field gradients, which may be further improved by careful design of the tip. Pipette well design itself was not carefully examined, as the high field regions of interest but modification of its geometry yields small effects in comparison to tip design; efforts into optimization the well itself should focus on fluid handling, reliability, and overall system integration.

Similarly, there are a number of important implications as result of metalizing the tip that should be considered. Raising the metalization edge up the tip, closer to the wire's termination, distributes the electric field, thus adjusting this height allows one to control dielectrophoretic forces to accumulate particles most advantageously. Likewise, increasing the peak dielectrophoretic force results in a general lowering of the overall capture volume, thus the system becomes more dependent on fluid flows and diffusion than direct electrically-derived gradients. These forces must be balanced depending on the application. In engineering the electric field within the tip, one should be able to ensure the greatest electric field gradients occur within the confines of the tip, thus enabling a tip-based apparatus to capture a greater proportion of the targeted particulate. It should also be mentioned that, due to the disparity in conductance between metals and these electrolytes, the outer coating is essentially the driven electrode; one could directly connect to the shield and eliminate the wire with little change to the overall system performance.

4.2.4 Porous-PDMS Tip Simulations

To better understand the inner workings of the porous PDMS tips, a COMSOL model based on prior tips model was developed. Designing a 3-D model that incorporates a well-characterized replica of the internal pore structure of porous-PDMS is beyond the scope of this simulation and unnecessarily complex in order to elucidate underlying mechanisms. Instead, a number of polypropylene (same as the pipette wall) restrictions, arranged as a staggered array of rounded rings 50 μm tall and 20 μm thick. The rings are separated by 50 μm radially and 100 μm vertically, with a 20 μm stagger between rows. Again, the emphasis of the simulation is to model what occurs when a distributed array of sequential restrictions is placed in a critical region and its effect on the local electric field gradients.

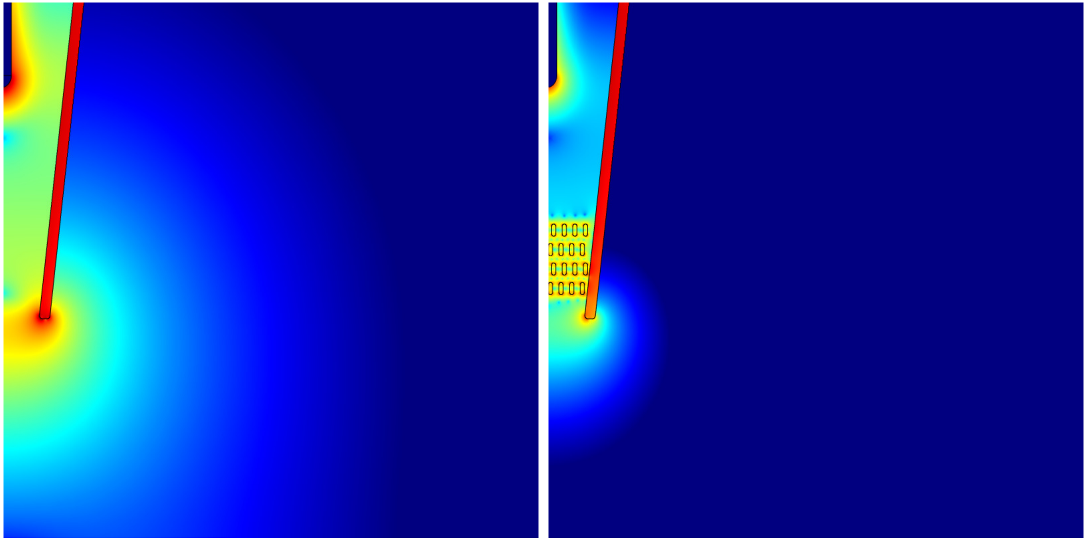

Standard-tip (left); with porous restrictions (right)

$log_{10}\left(\nabla\left|E^2\right|\right)$ term, range 10^{10} to $10^{19.5}$

Figure 4.19: Comparison plot ($log_{10}\left(\nabla\left|E^2\right|\right)$) an unrestricted tip-based system (left) and an array of rounded 50 μm by 20 μm polypropylene restrictions. These pores move and conentrate the field gradients to immediately around these restrictions; the high field gradient near the wire and the weak field gradient in the bulk are, as result, greatly reduced.

Figures 4.19 and 4.20 compare the baseline tip with a tip containing the aforementioned constrictions. Thermal profile, and, consequently, flow velocity is essentially unchanged due to the location of the potential drop and pipette tip wall. The electric field gradient, however, changes dramatically around the small pores created by the restrictions. High field gradients establish on the rounded edges of the restrictions and low field gradients at the midpoint of each pore. Concomitantly, the field gradient around the wire itself is reduced significantly, as is the breadth of weak field gradients in the bulk solution outside the wire. Again, it should be emphasized that the color scaling Empirically, moderate field gradients are unable generate sufficient DEP forces to capture nano-particles effectively, but do slowly affect particle distribution within a volume. High field gradients are necessary to hold particles in place.

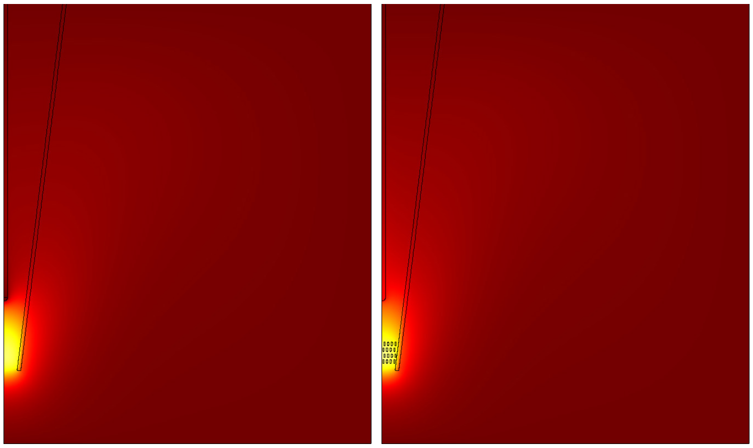

Thermal simulation, range 20 °C to 36 °C

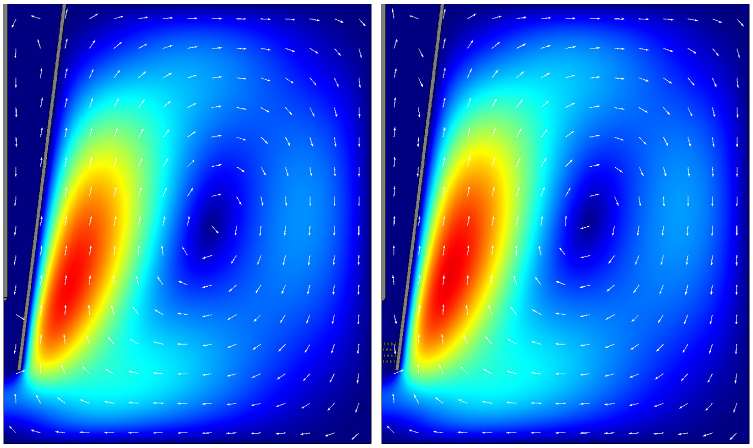

Flow velocity term, range 0 μm/s to 640 μm/s

Figure 4.20: Comparison of temperature and velocity plots between an unrestricted tip-based system (left) and an array of rounded 50 μm by 20 μm polypropylene restrictions (right). The thermal profile is pinched slightly into the porous region, but, given the pipette tip's wall the circulating flow appears essentially unaffected

Simple tip devices were likely unsuccessful due to geometry. There are essentially two high field gradients in the plain tip: one at the wire tip, which is well-recessed into the tip and reliant on diffusion to transport particles to the capture zone, and a smaller high field region at the edge of the tip. The gel encapsulated in the tip strongly impedes nanoparticle transport, e.g. 200 nm fluorescent beads. In essence, the presence of the gel all but obviates the DEP capture utility of the field gradient near the recessed wire, as particles are only weakly pulled through a restrictive medium. Likewise, even a small amount of gel remaining on the outside and bottom of a tip will effectively block particle accumulation on the high field region on the pipette tip.

These non-ideal factors are largely mitigated by moving to a solid dielectric porous structure as opposed to a hydrogel filling. With the highest DEP forces co-located with the flow-restricting pores, particles are concentrated in regions where competing forces (Brownian, thermal/density gradients) are less likely to affect particles. Second, rather than solely the inner circumference of the pipette tip opening being a relevant DEP capture zone, the entire tip opening consists of the much more dielectrophoretically active small pores, which greatly increase the effective capture area. Lastly, it provides a durable medium to store captured particles. As discussed in Sec. 4.1.2, particles are largely unable to passively diffuse through the porous PDMS matrix, with its pores ranging from 10 μm to 250 μm. The implications of using a structural polymer open cell foam (polypropylene, polyethylene, silicones, etc) as insulation-based DEP material opens up new devices structures and design workflows.

4.3 Conclusion

In this chapter, we have examined several different DEP device structures, with an overarching view at usability in high conductance solutions, such as direct interrogation of biological samples. Emphasis was placed on understanding the distributions of electric fields and their importance in effective DEP capture of particles, which requires analyzing fluid flow due to electrothermal effects and thermal management in general. The importance of achieving low overall current distributions to minimize Joule heating and concentrating electrical field gradients in low-flow regions cannot be emphasized enough. Limitations of the studies and simulations should also be noted: namely, studies here looked at primarily low-frequency behavior, where the Clausius-Mossoti factor is largely determined by the medium and particle's respective conductivities rather than their respective permittivities. The complex dielectric properties of the medium and desired particles will be very different at higher frequencies. Ultimately, for new device structures to be realized, one must keep all these factors in mind, whereas low-conductance DEP has fewer design constraints.

Chapter 4, in part, has been submitted for publication of the material as it may appear in ELECTROPHORESIS, 2017, Heineck, Daniel P.; Lewis, Jean M.; Heller, Michael J., Wiley-Blackwell. The dissertation author was the primary investigator and author of this paper.

Chapter 5

Conclusions and future work

The primary focus of this thesis is to characterize and model the use of dielectrophoretic (DEP) devices in high-conductance solutions such as those found in biological fluids. Therein, many of the design constraints and fundamental limitations of high-conductance DEP were demonstrated. Platinum electrode degradation is shown when chlorine-bearing electrolytes are used in DEP systems. Corrosion is shown to increase with current density and with lower frequency AC stimulus, both of which point to platinum-chlorine reaction kinetics as the driving culprit. As biological fluids are inherently high in chlorine concentration, minimizing heating via device structure is necessary, in addition to lowering current density and maximizing electrical drive frequency that maintains selectivity to desired particles. These issues are not necessarily restricted to dielectrophoretic devices, but any high-conductance electrokinetic device will be similarly constrained.

Several DEP device architectures are explored and, as result, several important themes appear. Joule heating is a major effect in high-conductance solutions and resulting effects on electrolyte density drives fluid flow. Unfortunately, the highest electric field gradients coincide with the greatest Joule heating, thus drag forces from electrothermal flow are often in competition with positive-DEP forces. Suspended wire devices were compared against wire arrays placed on top of a glass substrate. The former showed substantial electrothermal flow between the wires, making positive-DEP capture of fluorescent beads difficult in high-conductance solutions. The latter suffered less from electrothermal effects since fluid circulated above the wires instead. Planar electrode arrays also have minimal time-averaged electrothermal effects, as heat is effectively transfered to the silicon substrate. Devices embedded into a pipette tip also show minimal electrothermal effects in the DEP-active region since the thermal gradient is minimal and fluid movement is essentially restricted inside pipette tip. Device architecture can go a long ways towards minimizing thermal gradients. Use of structural porous materials, in the form of porous-PDMS, is demonstrated as effective in generating large field gradients for DEP.

A culminating all-important factor in high-conductance DEP devices is thermal management. With the high conductivity of biological solutions, Joule heating is of major concern that cannot be avoided and must be mitigated by device design instead. Thermal issues are two-fold: first, electrothermal flows compete with DEP for effective particle isolation and, second, electrochemical corrosion is kinetically dependent. These constraints, by and large, point to minimizing overall electric fields and focusing on maximizing local electric field gradients by geometry. Ultimately, that indicates a need for micron-sized dimensions or smaller in critical regions of devices.

For small structures where one can engineer electric field gradients greatly by lithographic patterning of device geometry, overall inter-electrode potentials need to be small in order to minimize current density, as the inter-electrode impedance will be extremely low. Large devices, where inter-electrode distances are in millimeters or more, will necessitate greater voltages to overcome potential drop across the electrolyte. Current density near electrodes can still be large due to crowding, with all the non-ideal attendant corrosion. Doubly, due to fabrication complexities, the highest electric field gradients occur in remote regions of the device, where effective capture of particles is minimized. Large devices afford opportunities to inexpensively scale effective capture area, but this is easily compromised if the device is allowed to heat significantly.

Insulation-based DEP topologies are a good match to high conductivity solutions. One can design the electrodes to be large, thus minimize local current density and its attendant corrosive effects. Electric fields may instead be constricted into large gradients in regions far away from the electrodes. Additionally, nonreactive insulating materials may be selected for the constrictive regions instead of chemically-active metals, further reducing device degradation. Lastly, constrictions in insulation-based DEP may be sufficiently distributed to ensure that any local Joule heating may be diffused over a much greater area, lowering peak temperatures and minimizing thermal gradients. Most efforts into insulator-based DEP has been focused into small devices where that require extensive lithographic patterning, which greatly limits overall active surface area and is expensive. Bulk structures, where the material itself can reliably formed into small geometries without need for patterning, allow for scaling device size over several orders of magnitudes.

5.1 Future Work

Better understanding of demands of high-conductance DEP offers insights into designing new devices. Figure 5.1 shows two examples of a large-scale, insulator-based, DEP device integrated into a blood-draw tube. The overarching design is simple: a structural porous membrane separates the tube into two parts where

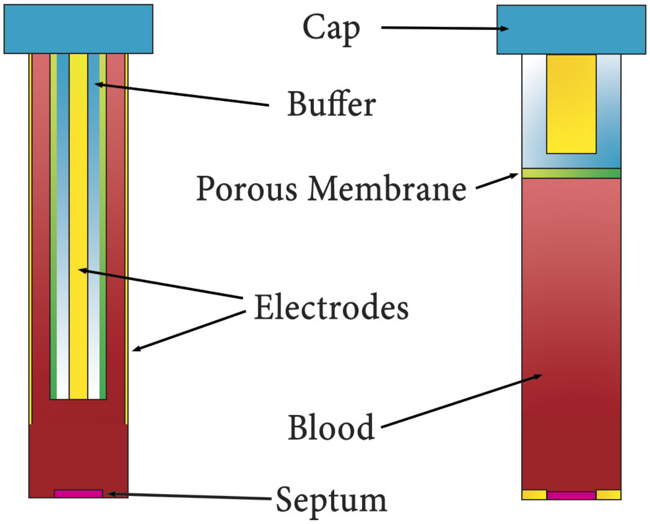

Figure 5.1: Schematic diagrams of proposed insulator-based DEP blood draw tubes. Architecturally both designs operate on the same principle. A porous, open-cell, membrane made of a dielectric medium is placed as to separate the tube into a blood side and a buffer side. Electrodes are placed in each medium, respectively, and the electric field applied between the electrodes is locally constrained through the porous medium, thus drawing positive-DEP particles to the region.

electrodes are placed, respectively. Diffusion of even small particles across the barrier is extremely slow, essentially inhibiting any non-targeted transport. By applying an electric field across the membrane, local high field gradients are realized throughout the porous structures, drawing particles, e.g. cell-free DNA, RNA or exosomes, into the membrane via positive-DEP.

Cell-free bloodborne products are known to degrade over time [75]–[77], thus incorporating the DEP isolation into the blood draw dramatically lowers the degradation time compared to common centrifuge steps and simplifies work-flow [18]. To ensure long-term stability and integrity of the now-captured particulate, stabilization products must be included into the draw tube. While the core concept of insulator-DEP through a rigid porous membrane is demonstrated herein, a number of technical challenges still remain. First, is better characterization and

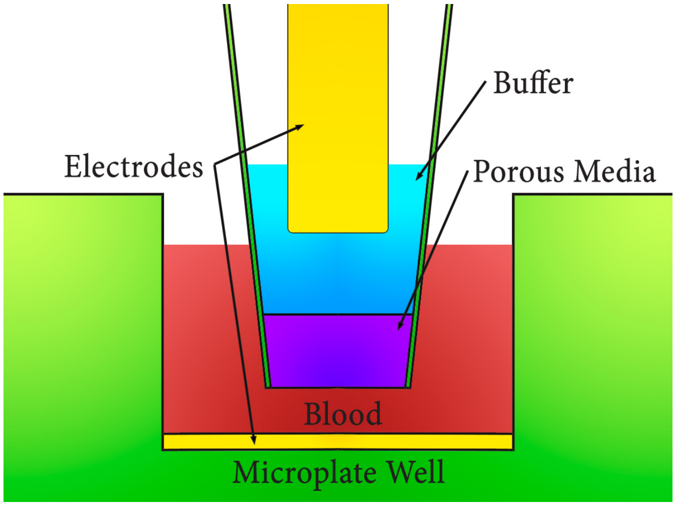

Figure 5.2: Schematic for an insulation-DEP based system designed to integrate into a microplate well. Using a robotic pipette handler for fluid handling in addition to specialized microplates and tips for DEP extraction, a system could automate particle extraction and subsequent sample preparation in a single tool.

development of porous membrane materials, especially in blood as opposed to synthetic substitutes. Bio-compatible structural polymers, such as polypropylene, silicones, or polystyrene all inherently hydrophobic, which raises concerns about cell and nonspecific protein adhesion [78]. Hydrophilic surface coatings, showing far reduced adhesion and nonspecific binding, may be necessary to mitigate contamination and cell lysis. Likewise, an effective, stable, buffer needs to be developed for a completely pre-fabricated tube. Lastly, releasing captured particles may prove problematic, depending on the particle properties. Release protocols will need developing, especially for electrically-neutral particles. Similar design constraints would be necessary for a robotic microtiter-based system, albeit with a slightly different work flow. A schematic of a microplate system is shown in Fig. 5.2.

The small pore structure dominates electric field gradients, especially with high conductance solutions. Therefore, device geometry optimization can be prioritized towards other criteria: namely packaging and ability to manufacture; fluid management, and overall integration with surrounding hardware. This flexibility afforded by allowing the electrodes to be remote to the active region enables structures than would otherwise be designed with DEP collection focused at the electrode. This subset of device designs is hitherto unexplored and shows tremendous promise.

Chapter 5, in part, is being prepared for publication submission. Heineck, Daniel P.; Heller, Michael J. The dissertation author is the primary investigator and author of the material herein.

Bibliography

[1] R. Pethig, "Dielectrophoresis: Status of the theory, technology, and applications", *Biomicrofluidics*, vol. 4, no. 2, p. 022 811, 2010. DOI: 10.1063/1.3456626.

[2] T. V. D. Simon Ramo John R. Whinnery, *Fields and waves in communication electronics*. JOHN WILEY & SONS INC, Feb. 11, 1994, 864 Seiten, ISBN: 0471585513.

[3] T. Jones, "Basic theory of dielectrophoresis and electrorotation", *IEEE Eng. Med. Biol. Mag.*, vol. 22, no. 6, pp. 33–42, Nov. 2003. DOI: 10.1109/memb.2003.1304999.

[4] A. Irimajiri, T. Hanai, and A. Inouye, "A dielectric theory of multi-stratified shell model with its application to a lymphoma cell", *Journal of Theoretical Biology*, vol. 78, no. 2, pp. 251–269, May 1979. DOI: 10.1016/0022-5193(79)90268-6.

[5] V. L. Sukhorukov, G. Meedt, M. Kürschner, and U. Zimmermann, "A single-shell model for biological cells extended to account for the dielectric anisotropy of the plasma membrane", *Journal of Electrostatics*, vol. 50, no. 3, pp. 191–204, Feb. 2001. DOI: 10.1016/s0304-3886(00)00037-1.

[6] A. Ramos, Ed., *Electrokinetics and electrohydrodynamics in microsystems*. Springer Science Business Media, 2011. DOI: 10.1007/978-3-7091-0900-7.

[7] A. V. Delgado, F. González-Caballero, R. J. Hunter, L. K. Koopal, and J. Lyklema, "Measurement and interpretation of electrokinetic phenomena (IUPAC technical report)", *Pure and Applied Chemistry*, vol. 77, no. 10, Jan. 2005. DOI: 10.1351/pac200577101753.

[8] M. A. Brown, A. Goel, and Z. Abbas, "Effect of electrolyte concentration on the stern layer thickness at a charged interface", *Angewandte Chemie*

International Edition, vol. 55, no. 11, pp. 3790–3794, Feb. 2016. DOI: 10.1002/anie.201512025.

[9] B. Hirschorn, M. E. Orazem, B. Tribollet, V. Vivier, I. Frateur, and M. Musiani, "Determination of effective capacitance and film thickness from constant-phase-element parameters", *Electrochimica Acta*, vol. 55, no. 21, pp. 6218–6227, Aug. 2010. DOI: 10.1016/j.electacta.2009.10.065.

[10] M. Scott, K. V. Kaler, and R. Paul, "Theoretical model of electrode polarization and AC electroosmotic fluid flow in planar electrode arrays", *Journal of Colloid and Interface Science*, vol. 238, no. 2, pp. 449–451, Jun. 2001. DOI: 10.1006/jcis.2001.7651.

[11] A. Ramos, H. Morgan, N. G. Green, and A. Castellanos, "AC electric-field-induced fluid flow in microelectrodes", *Journal of colloid and interface science*, vol. 217, no. 2, pp. 420–422, 1999.

[12] A. Castellanos, A. Ramos, A. Gonzalez, N. G. Green, and H. Morgan, "Electrohydrodynamics and dielectrophoresis in microsystems: Scaling laws", *Journal of Physics D: Applied Physics*, vol. 36, no. 20, p. 2584, 2003. DOI: 10.1088/0022-3727/36/20/023.

[13] D. A. Saville, "ELECTROHYDRODYNAMICS:the Taylor-melcher leaky dielectric model", *Annu. Rev. Fluid Mech.*, vol. 29, no. 1, pp. 27–64, Jan. 1997. DOI: 10.1146/annurev.fluid.29.1.27.

[14] H. A. Haus and J. R. Melcher, *Electromagnetic fields and energy.* Prentice-Hall: Englewood Cliffs, NJ, 1989.

[15] A. González, A. Ramos, H. Morgan, N. G. Green, and A. Castellanos, "Electrothermal flows generated by alternating and rotating electric fields in microsystems", *J. Fluid Mech.*, vol. 564, p. 415, Sep. 2006. DOI: 10.1017/s0022112006001595.

[16] D. F. Chen and H. Du, "Simulation studies on electrothermal fluid flow induced in a dielectrophoretic microelectrode system", *Journal of Micromechanics and Microengineering*, vol. 16, no. 11, p. 2411, 2006. DOI: 10.1088/0960-1317/16/11/023. [Online]. Available: http://stacks.iop.org/0960-1317/16/i=11/a=023.

[17] C. Oddoze, E. Lombard, and H. Portugal, "Stability study of 81 analytes in human whole blood, in serum and in plasma", *Clinical Biochemistry*, vol. 45, no. 6, pp. 464–469, Apr. 2012. DOI: 10.1016/j.clinbiochem.2012.01.012.

[18] J. M. Lewis, D. P. Heineck, and M. J. Heller, "Detecting cancer biomarkers in blood: Challenges for new molecular diagnostic and point-of-care tests using cell-free nucleic acids", *Expert review of molecular diagnostics*, vol. 15, no. 9, pp. 1187–1200, 2015.

[19] C. D. Chin, V. Linder, and S. K. Sia, "Commercialization of microfluidic point-of-care diagnostic devices", *Lab on a Chip*, vol. 12, no. 12, p. 2118, 2012. DOI: 10.1039/c2lc21204h.

[20] F.-Y. Kong, S.-X. Gu, W.-W. Li, T.-T. Chen, Q. Xu, and W. Wang, "A paper disk equipped with graphene/polyaniline/au nanoparticles/glucose oxidase biocomposite modified screen-printed electrode: Toward whole blood glucose determination", *Biosensors and Bioelectronics*, vol. 56, pp. 77–82, Jun. 2014. DOI: 10.1016/j.bios.2013.12.067.

[21] X. Yang, O. Forouzan, T. P. Brown, and S. S. Shevkoplyas, "Integrated separation of blood plasma from whole blood for microfluidic paper-based analytical devices", *Lab Chip*, vol. 12, no. 2, pp. 274–280, 2012. DOI: 10.1039/c1lc20803a.

[22] M. G. Lee, J. H. Shin, C. Y. Bae, S. Choi, and J.-K. Park, "Label-free cancer cell separation from human whole blood using inertial microfluidics at low shear stress", *Analytical Chemistry*, vol. 85, no. 13, pp. 6213–6218, Jul. 2013. DOI: 10.1021/ac4006149.

[23] F. Inci, O. Tokel, S. Wang, U. A. Gurkan, S. Tasoglu, D. R. Kuritzkes, and U. Demirci, "Nanoplasmonic quantitative detection of intact viruses from unprocessed whole blood", *ACS Nano*, vol. 7, no. 6, pp. 4733–4745, Jun. 2013. DOI: 10.1021/nn3036232.

[24] J. C. Barrese, J. Aceros, and J. P. Donoghue, "Scanning electron microscopy of chronically implanted intracortical microelectrode arrays in non-human primates", *J. Neural Eng.*, vol. 13, no. 2, p. 026 003, Jan. 2016. DOI: 10.1088/1741-2560/13/2/026003.

[25] A. Prasad, Q.-S. Xue, V. Sankar, T. Nishida, G. Shaw, W. J. Streit, and J. C. Sanchez, "Comprehensive characterization and failure modes of tungsten microwire arrays in chronic neural implants", *J. Neural Eng.*, vol. 9, no. 5, p. 056 015, Sep. 2012. DOI: 10.1088/1741-2560/9/5/056015.

[26] D. Zhou and R. Greenberg, "Electrochemistry in neural stimulation by biomedical implants", *Electrochemistry*, vol. 17, no. 3, pp. 249–262, 2011.

[27] E. Patrick, M. E. Orazem, J. C. Sanchez, and T. Nishida, "Corrosion of tungsten microelectrodes used in neural recording applications", *Journal of Neuroscience Methods*, vol. 198, no. 2, pp. 158–171, Jun. 2011. DOI: 10.1016/j.jneumeth.2011.03.012.

[28] E. M. Hudak, J. T. Mortimer, and H. B. Martin, "Platinum for neural stimulation: Voltammetry considerations", *J. Neural Eng.*, vol. 7, no. 2, p. 026 005, Mar. 2010. DOI: 10.1088/1741-2560/7/2/026005.

[29] X. Fang, H. Sakaguchi, T. Fujikado, M. Osanai, Y. Ikuno, M. Kamei, M. Ohji, T. Yagi, and Y. Tano, "Electrophysiological and histological studies of chronically implanted intrapapillary microelectrodes in rabbit eyes", *Graefe's Arch Clin Exp Ophthalmo*, vol. 244, no. 3, pp. 364–375, Aug. 2005. DOI: 10.1007/s00417-005-0073-9.

[30] B. Shepherd and G. Clark, "Scanning electron microscopy of platinum scala tympani electrodes following chronic stimulation in patients", *Biomaterials*, vol. 12, no. 4, pp. 417–423, May 1991. DOI: 10.1016/0142-9612(91)90011-x.

[31] M. D. Craggs, N. de N. Donaldson, and P. E. K. Donaldson, "Performance of platinum stimulating electrodes, mapped on the limitvoltage plane", *Medical & Biological Engineering & Computing*, vol. 24, no. 4, pp. 424–430, Jul. 1986. DOI: 10.1007/bf02442699.

[32] S. A. Brown and K. Merritt, "Electrochemical corrosion in saline and serum", *Journal of Biomedical Materials Research*, vol. 14, no. 2, pp. 173–175, Mar. 1980. DOI: 10.1002/jbm.820140208.

[33] R. C. Black and P. Hannaker, "Dissolution of smooth platinum electrodes in biological fluids.", eng, *Appl Neurophysiol*, vol. 42, no. 6, pp. 366–374, 1980. DOI: 10.1159/000102382.

[34] E. R. Castro and A. Manz, “Present state of microchip electrophoresis: State of the art and routine applications”, *Journal of Chromatography A*, vol. 1382, pp. 66–85, Feb. 2015. DOI: 10.1016/j.chroma.2014.11.034.

[35] A. Sonnenberg, J. Y. Marciniak, E. A. Skowronski, S. Manouchehri, L. Rassenti, E. M. Ghia, G. F. Widhopf, T. J. Kipps, and M. J. Heller, “Dielectrophoretic isolation and detection of cancer-related circulating cell-free DNA biomarkers from blood and plasma”, *ELECTROPHORESIS*, vol. 35, no. 12-13, pp. 1828–1836, May 2014, ISSN: 0173-0835. DOI: 10.1002/elps.201400016.

[36] M. Hayes, A. Kuhn, and W. Grant, “Aggregation effects on the electrocatalytic activity of platinum”, *Journal of Catalysis*, vol. 53, no. 1, pp. 88–95, 1978, ISSN: 0021-9517. DOI: 10.1016/0021-9517(78)90009-X. [Online]. Available: http://www.sciencedirect.com/science/article/pii/002195177890009X.

[37] J. Llopis, “Corrosion of platinum metals and chemisorption”, *Catalysis Reviews*, vol. 2, no. 1, pp. 161–220, Jan. 1969. DOI: 10.1080/01614946908066543.

[38] X. F. Wei and W. M. Grill, “Impedance characteristics of deep brain stimulation electrodes in vitro and in vivo”, *J. Neural Eng.*, vol. 6, no. 4, p. 046 008, Jul. 2009. DOI: 10.1088/1741-2560/6/4/046008.

[39] R. Juchniewicz, “The influence of alternating current on the anodic behaviour of platinum”, *Platinum Metals Review*, vol. 6, no. 3, pp. 100–105, 1962. [Online]. Available: http://www.ingentaconnect.com/content/matthey/pmr/1962/00000006/00000003/art00009.

[40] R. Bentley and T. R. Prentice, “The alternating current electrolysis of concentrated acids”, *Journal of Applied Chemistry*, vol. 7, no. 11, pp. 619–626, May 1957. DOI: 10.1002/jctb.5010071109.

[41] J. Llopis and A. Sancho, “Electrochemical corrosion of platinum in hydrochloric acid solutions”, *Journal of The Electrochemical Society*, vol. 108, no. 8, p. 720, 1961. DOI: 10.1149/1.2428205.

[42] E. Briner and A. Yalda, “Recherches sur l’électrolyse avec courant ondulé. III. observations sur l’attaque des électrodes de platine et la formation de l’ozone sous l’effet du courant alternatif et du courant ondulé, à différentes fréquences et à différentes concentrations des so”, *Helvetica Chimica Acta*, vol. 26, no. 6, pp. 1829–1835, Oct. 1943. DOI: 10.1002/hlca.19430260612.

[43] U. Pyell, “Characterization of nanoparticles by capillary electromigration separation techniques”, *ELECTROPHORESIS*, vol. 31, no. 5, pp. 814–831, Mar. 2010. DOI: 10.1002/elps.200900555.

[44] W. Franks, I. Schenker, P. Schmutz, and A. Hierlemann, “Impedance characterization and modeling of electrodes for biomedical applications”, *IEEE Transactions on Biomedical Engineering*, vol. 52, no. 7, pp. 1295–1302, Jul. 2005. DOI: 10.1109/tbme.2005.847523.

[45] M. Pourbaix, J. Van Muylder, and N. De Zoubov, “Electrochemical properties of the platinum metals”, *Platinum metals review*, vol. 3, no. 2, pp. 47–53, 1959. [Online]. Available: http://www.ingentaconnect.com/content/matthey/pmr/1959/00000003/00000002/art00004.

[46] J. Llopis and M. Vázquez, “Study of the impedance of a platinum electrode in the system cl2/cl- (HClO4aq)”, *Electrochimica Acta*, vol. 8, no. 3, pp. 163–173, Mar. 1963. DOI: 10.1016/0013-4686(63)80014-6.

[47] R. Juchniewicz, “The influence of increasing superimposed 50 c/s a.c. on the anodic dissolution of platinum in 3% sodium chloride”, *Corrosion Science*, vol. 6, no. 2, pp. 69–77, Jan. 1966. DOI: 10.1016/s0010-938x(66)80026-4.

[48] D. Rand and R. Woods, “A study of the dissolution of platinum, palladium, rhodium and gold electrodes in 1 m sulphuric acid by cyclic voltammetry”, *Journal of Electroanalytical Chemistry and Interfacial Electrochemistry*, vol. 35, no. 1, pp. 209–218, Mar. 1972. DOI: 10.1016/s0022-0728(72)80308-5.

[49] A. Kuhn and P. Wright, “The behaviour of platinum, iridium and ruthenium electrodes in strong chloride solutions”, *Journal of Electroanalytical Chemistry and Interfacial Electrochemistry*, vol. 41, no. 3, pp. 329–349, Feb. 1973. DOI: 10.1016/s0022-0728(73)80412-7.

[50] L. R. Czarnetzki and L. J. J. Janssen, “Formation of hypochlorite, chlorate and oxygen during NaCl electrolysis from alkaline solutions at an RuO2/TiO2 anode”, *J Appl Electrochem*, vol. 22, no. 4, pp. 315–324, Apr. 1992. DOI: 10.1007/bf01092683.

[51] G. Benke and W. Gnot, “The electrochemical dissolution of platinum”, *Hydrometallurgy*, vol. 64, no. 3, pp. 205–218, Jun. 2002. DOI: 10.1016/s0304-386x(02)00044-0.

[52] Y. Song, A. Sonnenberg, Y. Heaney, and M. J. Heller, "Device for dielectrophoretic separation and collection of nanoparticles and DNA under high conductance conditions", *ELECTROPHORESIS*, vol. 36, no. 9-10, pp. 1107–1114, Apr. 2015. DOI: 10.1002/elps.201400507.

[53] S. Manouchehri, S. Ibsen, J. Wright, L. Rassenti, E. M. Ghia, G. F. Widhopf, T. J. Kipps, and M. J. Heller, "Dielectrophoretic recovery of DNA from plasma for the identification of chronic lymphocytic leukemia point mutations", *Int. J. Hematol. Oncol.*, vol. 5, no. 1, pp. 27–35, May 2016. DOI: 10.2217/ijh-2015-0009.

[54] S. Ibsen, A. Sonnenberg, C. Schutt, R. Mukthavaram, Y. Yeh, I. Ortac, S. Manouchehri, S. Kesari, S. Esener, and M. J. Heller, "Recovery of drug delivery nanoparticles from human plasma using an electrokinetic platform technology", *Small*, vol. 11, no. 38, pp. 5088–5096, Aug. 2015. DOI: 10.1002/smll.201500892.

[55] A. Sharma, C.-H. Han, and J. Jang, "Rapid electrical immunoassay of the cardiac biomarker troponin i through dielectrophoretic concentration using imbedded electrodes", *Biosensors and Bioelectronics*, vol. 82, pp. 78–84, Aug. 2016. DOI: 10.1016/j.bios.2016.03.056. [Online]. Available: http://dx.doi.org/10.1016/j.bios.2016.03.056.

[56] R. E. Fernandez, B. J. Sanghavi, V. Farmehini, J. L. Chávez, J. Hagen, N. Kelley-Loughnane, C.-F. Chou, and N. S. Swami, "Aptamer-functionalized graphene-gold nanocomposites for label-free detection of dielectrophoretic-enriched neuropeptide y", *Electrochemistry Communications*, vol. 72, pp. 144–147, Nov. 2016. DOI: 10.1016/j.elecom.2016.09.017. [Online]. Available: http://dx.doi.org/10.1016/j.elecom.2016.09.017.

[57] B. J. Sanghavi, W. Varhue, A. Rohani, K.-T. Liao, L. A. L. Bazydlo, C.-F. Chou, and N. S. Swami, "Ultrafast immunoassays by coupling dielectrophoretic biomarker enrichment in nanoslit channel with electrochemical detection on graphene", *Lab Chip*, vol. 15, no. 24, pp. 4563–4570, 2015. DOI: 10.1039/c5lc00840a. [Online]. Available: http://dx.doi.org/10.1039/C5LC00840A.

[58] C.-H. Chuang, T.-F. Wu, C.-H. Chen, K.-C. Chang, J.-W. Ju, Y.-W. Huang, and V. V. Nhan, "Lab on a chip for multiplexed immunoassays to detect bladder cancer using multifunctional dielectrophoretic manipulations", *Lab*

Chip, vol. 15, no. 14, pp. 3056–3064, 2015. DOI: 10.1039/c5lc00352k. [Online]. Available: http://dx.doi.org/10.1039/C5LC00352K.

[59] H. Song, J. M. Rosano, Y. Wang, C. J. Garson, B. Prabhakarpandian, K. Pant, G. J. Klarmann, A. Perantoni, L. M. Alvarez, and E. Lai, "Continuous-flow sorting of stem cells and differentiation products based on dielectrophoresis", *Lab on a Chip*, vol. 15, no. 5, pp. 1320–1328, 2015. DOI: 10.1039/c4lc01253d.

[60] B. Mathew, A. Alazzam, G. Destgeer, and H. J. Sung, "Dielectrophoresis based cell switching in continuous flow microfluidic devices", *Journal of Electrostatics*, vol. 84, pp. 63–72, Dec. 2016. DOI: 10.1016/j.elstat.2016.09.003. [Online]. Available: http://dx.doi.org/10.1016/j.elstat.2016.09.003.

[61] D. Tsikritsis, H. Shi, Y. Wang, S. Velugotla, V. Sršeň, A. Elfick, and A. Downes, "Label-free biomarkers of human embryonic stem cell differentiation to hepatocytes", *Cytometry*, vol. 89, no. 6, pp. 575–584, May 2016. DOI: 10.1002/cyto.a.22875. [Online]. Available: http://dx.doi.org/10.1002/cyto.a.22875.

[62] E. Bisceglia, M. Cubizolles, C. I. Trainito, J. Berthier, C. Pudda, O. Français, F. Mallard, and B. L. Pioufle, "A generic and label free method based on dielectrophoresis for the continuous separation of microorganism from whole blood samples", *Sensors and Actuators B: Chemical*, vol. 212, pp. 335–343, Jun. 2015. DOI: 10.1016/j.snb.2015.02.024.

[63] M. Sun, P. Agarwal, S. Zhao, Y. Zhao, X. Lu, and X. He, "Continuous on-chip cell separation based on conductivity-induced dielectrophoresis with 3D self-assembled ionic liquid electrodes", *Analytical Chemistry*, vol. 88, no. 16, pp. 8264–8271, Aug. 2016. DOI: 10.1021/acs.analchem.6b02104.

[64] K. Park, S. Kabiri, and S. Sonkusale, "Dielectrophoretic lab-on-CMOS platform for trapping and manipulation of cells", *Biomedical Microdevices*, vol. 18, no. 1, Jan. 2016. DOI: 10.1007/s10544-016-0030-x.

[65] P.-Y. Weng, I.-A. Chen, C.-K. Yeh, P.-Y. Chen, and J.-Y. Juang, "Size-dependent dielectrophoretic crossover frequency of spherical particles", *Biomicrofluidics*, vol. 10, no. 1, p. 011 909, Jan. 2016. DOI: 10.1063/1.4941853.

[66] M. A. Saucedo-Espinosa, M. M. Rauch, A. LaLonde, and B. H. Lapizco-Encinas, "Polarization behavior of polystyrene particles under direct current

and low-frequency (1 kHz) electric fields in dielectrophoretic systems", *ELECTROPHORESIS*, vol. 37, no. 4, pp. 635–644, Dec. 2015. DOI: 10.1002/elps.201500338.

[67] A. Sonnenberg, J. Y. Marciniak, L. Rassenti, E. M. Ghia, E. A. Skowronski, S. Manouchehri, J. McCanna, G. F. Widhopf, T. J. Kipps, and M. J. Heller, "Rapid electrokinetic isolation of cancer-related circulating cell-free DNA directly from blood", *Clinical Chemistry*, vol. 60, no. 3, pp. 500–509, Nov. 2013, ISSN: 1530-8561. DOI: 10.1373/clinchem.2013.214874.

[68] V. Vitagliano and P. Lyons, "Diffusion coefficients for aqueous solutions of sodium chloride and barium chloride", *Journal of the American Chemical Society*, vol. 78, no. 8, pp. 1549–1552, 1956.

[69] C. Malmberg and A. Maryott, "Dielectric constant of water from 0° to 100° C", *J Res Nat Bureau Stand*, vol. 56, pp. 1–8, 1956.

[70] U. Kaatze, "Complex permittivity of water as a function of frequency and temperature", *Journal of Chemical & Engineering Data*, vol. 34, no. 4, pp. 371–374, Oct. 1989. DOI: 10.1021/je00058a001.

[71] W. Ellison, A. Balana, G. Delbos, K. Lamkaouchi, L. Eymard, C. Guillou, and C. Prigent, "New permittivity measurements of seawater", *Radio Science*, vol. 33, no. 3, pp. 639–648, May 1998. DOI: 10.1029/97rs02223.

[72] D. Ben-Yaakov, D. Andelman, and R. Podgornik, "Dielectric decrement as a source of ion-specific effects", *The Journal of Chemical Physics*, vol. 134, no. 7, p. 074 705, 2011. DOI: 10.1063/1.3549915.

[73] R. Krishnan, D. A. Dehlinger, G. J. Gemmen, R. L. Mifflin, S. C. Esener, and M. J. Heller, "Interaction of nanoparticles at the {dep} microelectrode interface under high conductance conditions", *Electrochemistry Communications*, vol. 11, no. 8, pp. 1661–1666, 2009, ISSN: 1388-2481. DOI: 10.1016/j.elecom.2009.06.033. [Online]. Available: http://www.sciencedirect.com/science/article/pii/S1388248109003014.

[74] W. Y. Gu, H. Yao, A. L. Vega, and D. Flagler, "Diffusivity of ions in agarose gels and intervertebral disc: Effect of porosity", *Annals of Biomedical Engineering*, vol. 32, no. 12, pp. 1710–1717, Dec. 2004. DOI: 10.1007/s10439-004-7823-4.

[75] J. A. Hoerter, V. Krishnan, T. A. Lionberger, and N. G. Walter, “Sirna-like double-stranded rnas are specifically protected against degradation in human cell extract”, *PloS one*, vol. 6, no. 5, e20359, 2011. DOI: 10.1371/journal.pone.0020359.

[76] P. B. Gahan, *Circulating nucleic acids in early diagnosis, prognosis and treatment monitoring*, O. Golubnitschaja, Ed., ser. Advances in Predictive, Preventive and Personalised Medicine. Springer, 2015, vol. 5.

[77] A. N. Barrett, B. G. Zimmermann, D. Wang, A. Holloway, and L. S. Chitty, “Implementing prenatal diagnosis based on cell-free fetal DNA: Accurate identification of factors affecting fetal DNA yield”, *PLoS One*, vol. 6, no. 10, e25202, 2011. DOI: 10.1371/journal.pone.0025202.

[78] T. A. Horbett, J. J. Waldburger, B. D. Ratner, and A. S. Hoffman, “Cell adhesion to a series of hydrophili-hydrophobic copolymers studies with a spinning disc apparatus”, *Journal of Biomedical Materials Research*, vol. 22, no. 5, pp. 383–404, May 1988. DOI: 10.1002/jbm.820220503.